Analyzing Power Measurement for p + 3He Elastic scattering at Intermediate Energies

博士論文

Analyzing Power Measurement for $p + \overrightarrow{^3\mathrm{He}}$ Elastic Scattering at Intermediate Energies

（中間エネルギーにおける陽子 $+\overrightarrow{^3\mathrm{He}}$ 弾性散乱の偏極分解能測定）

東北大学大学院　理学研究科
物理学専攻

渡邉跡武

令和元年

Abstract

With the aim of pinning down three-nucleon force (3NF) effects in comparison with to the rigorous numerical four-nucleon calculations and approaching the total isospin channel of $T = 3/2$ of 3NFs, we plan to measure the complete set of the p–^{3}He elastic scattering at intermediate energies. For the measurement of ^{3}He analyzing power and spin-correlation coefficients, we have constructed the polarized ^{3}He target system.

The polarized ^{3}He target is based on the spin-exchange optical pumping (SEOP) method. The ^{3}He target is the double-chambered cell made of boron-free aluminosilicate glass and contains ^{3}He gas together with alkali-metals as well as N_2 gas. We measured the ^{3}He polarization by the adiabatic fast passage (AFP) NMR method in combination with the alkali-metal electron paramagnetic resonance (EPR) method. However, to obtain the absolute value of ^{3}He polarization of the target chamber from the EPR method, it is necessary to know the ^{3}He number densities, namely the gas temperature inside the cell. In this work, we studied the gas temperature and the polarization gradient which is the polarization difference between each chamber based on numerical simulations. As a result, we obtained the target polarization with accuracies of 2–6 % for the ^{3}He cells.

For the direct measurement of the target polarization, we performed the neutron transmission experiment using a neutron source at RIKEN. This measurement utilizes the fact that the neutron transmission for ^{3}He depends on the ^{3}He polarization. The obtained target polarizations have good agreements with the results from the numerical simulations.

Using the polarized ^{3}He target we performed the measurement of ^{3}He analyzing powers A_{0y} for p–^{3}He scattering with incident energies of 70 MeV at CYRIC and 100 MeV at RCNP. We obtained the data in the wide angular range $\theta_{\mathrm{c.m.}} = 46°$–$141°$ and $\theta_{\mathrm{c.m.}} = 47°$–$149°$ for the experiments at CYRIC and RCNP, respectively. For the data at 70 MeV, statistical uncertainties are less than 0.02, and the systematic uncertainties are estimated to be 0.02 or less. For the data at 100 MeV, statistical uncertainties are less than 0.04 at the angles of $\theta_{\mathrm{c.m.}} \leq 116°$, and are from 0.05 to 0.08 at the angles of $\theta_{\mathrm{c.m.}} \geq 133°$. The systematic uncertainties are estimated to be 0.02 or less except for the angle of $\theta_{\mathrm{c.m.}} = 142°$.

The precise experimental data of A_{0y} were compared with the theoretical predictions based on various nuclear potentials. Clear discrepancies were found at around the angles where the A_{0y} takes minimum and maximum. Energy dependent study from 8.5 to 100 MeV for A_{0y} in comparison between the data and the theoretical predictions indicates that effects of fine components of 3NFs would be appearing with increasing an incident energy.

Contents

Chapter 1

Introduction

1.1 General Introduction

Nuclear forces are fundamental interactions acting in nuclei. One of the main interest of nuclear physics is to understand nuclear properties based on bare nuclear forces. Detailed knowledge of nuclear forces provides a solid basis for the descriptions of nuclear properties.

The theoretical description of the pair-wise nucleon-nucleon (NN) force was first given by Yukawa in 1935 in terms of a quantized field theory with a massive particle [1]. He predicted that this massive particle, called "meson" later, has a mass between that of a nucleon and an electron ($\sim$ 100 MeV) from the expected range of nuclear forces of about 2 fm. Therefore, the nuclear force was firstly described as a two-nucleon force (2NF). Meson was discovered from the cosmic radiation as π-meson later in 1937 [2]. Later, heavy mesons such as ρ and ω mesons were discovered with the development of accelerator facilities in the 1960's.

In the long-range part ($r \gtrsim 2$ fm; r denotes the distance between two nucleons) of NN forces, the one-pion exchange (OPE) is dominant and causes an attractive interaction. In the intermediate range ($1 \lesssim r \lesssim 2$ fm) with an attractive interaction, the two-pion exchange is the most important, although the contributions of heavy mesons become relevant. Many different processes play a role in the short-range region ($r \lesssim 1$ fm) such as multipion exchanges, various kinds of heavy mesons and quark-gluon exchanges. In the 1960's, the one-boson exchange (OBE) model was developed taking into account the contributions of heavy mesons. This model describes NN forces by the sum of the contributions of various one-meson exchanges based on Yukawa's theory. In parallel to the theoretical study the experiments of proton-proton and proton-neutron scattering as well as deuteron properties

were conduced at accelerator facilities all over the world. In the end of 1960's the phase shift analysis was performed by using about 2000 NN data up to 450 MeV [3]. The results of this analysis provided an important presupposition for the later theoretical work of providing a quantitative nuclear force based on meson theory.

In the 1990's, the Nijmegen group have presented a multienergy partial-wave analysis (PWA) for 4301 pp and np scattering data below 350 MeV [4]. The Nijmegen PWA has 39 parameters and has been fitted to the NN scattering data with χ^2/datum = 0.99. Further progress in experimental and theoretical study led to establishment of realistic NN potentials such as Argonne v_{18} potential (AV18 [5]), charge-dependent Bonn potential (CD-Bonn [6]) and Nijmegen potential (Nijmegen I,II [7]). These realistic NN potentials reproduce a total of 3000 to 4000 high-precision NN scattering data contained in the Nijmegen database [4] with an accuracy of χ^2/datum ~ 1. The realistic NN potentials also provide an excellent description for the properties of deuterons such as the binding energy. However, it has found that these realistic NN potentials fail to describe the binding energies of three- and four-nucleon ($4N$) systems, for which exact solutions of the Schrödinger equation are available, and lead to clear less binding. For systems of more nucleons *ab initio* microscopic calculations, such as Green's Function Monte Carlo (GFMC) [8] and no-core shell model calculations [9] show insufficient descriptions of the binding energies and low-lying levels of light mass nuclei. As for the symmetric nuclear matter, it has been reported that all NN potentials provide saturation at too high density [10]. Natural candidates to resolve these discrepancies are considered to be three-nucleon forces (3NFs) that appear when more than two nucleons interact.

The existence of 3NF was first predicted by Wigner in 1933 [11]. He did the first basic work of the calculations for few-nucleon systems. He also pointed out the significance of 3NFs in the $3N$ systems. The first theoretical insight of 3NFs was given by Fujita and Miyazawa in 1957 [12]. They provided the explicit form of 3NFs based on the two-pion exchange process among three-nucleons. Figure 1.1 shows the Feynman diagram for the Fujita-Miyazawa 3NF. One nucleon emits a pion that is absorbed by a second one and excites to a Δ-isobar in the intermediate state. This Δ-isobar turns into a nucleon emitting a second pion that is absorbed by the third nucleon. This process cannot be represented as the iteration of 2NFs. The recent 3NF models are formulated based on the Fujita-Miyazawa type 3NF because this type 3NF has been considered to be a main ingredient of 3NFs. Tucson-Melbourne (TM) [13–15] and Urbana IX (UIX) 3NF potentials [16] which are refined versions of the Fujita-Miyazawa type 3NF are often used in theoretical

calculations.

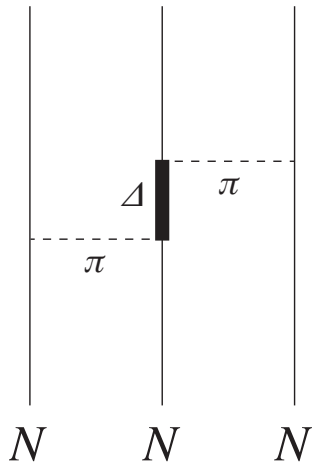

Figure 1.1: Feynman diagram for the Fujita-Miyazawa 3NF.

The first evidence for 3NFs was found in the $3N$ bound states, ^{3}H and ^{3}He [17, 18]. Again the binding energies of these nuclei are not reproduced by exact solutions of $3N$ Faddeev equations [19] employing realistic NN potentials only, that is, AV18, CD-Bonn and Nijmegen I, II [20]. In Ref. [20], the calculations in terms of Faddeev-Yakubovsky equation [21] have also been performed for ^{4}He, a $4N$ bound system. All the realistic NN potentials provide less binding, 0.5–0.8 MeV for $3N$ systems and 2–4 MeV for a $4N$ system. Including the TM or UIX 3NFs and adjusting the parameters of the 3NF models the correct binding energies are obtained. Note four-nucleon force effects have been estimated to be much smaller than those of 3NFs.

The binding energy mainly constrains only the overall strength. More detailed investigation of 3NF properties can be achieved by measuring the observables of few-nucleon scattering; differential cross sections and spin observables. The recent progress in computational capabilities made it possible to perform rigorous numerical calculations based on the Faddeev equation for the few-nucleon scattering processes. Therefore, the comparison between the predictions of rigorous numerical calculations and the high-precision data of few-nucleon scattering can provide a quantitative discussion of 3NF properties such as momentum dependence, spin and isospin dependence.

In the following sections, we first briefly describe the formalism of the realistic NN potentials, the 3NF models, and the chiral perturbation theory recently developed. Next, we describe the current status of the 3NF study in nucleon-deuteron (Nd) and proton-^{3}He

scattering systems. Finally, we present the requirements of the polarized ^{3}He target for the p–^{3}He scattering experiments and the purpose of the thesis.

1.2 Realistic Nucleon-Nucleon Potentials

We briefly describe the formalism of the most commonly used realistic NN potentials, Argonne, Bonn and Nijmegen potentials.

1.2.1 Argonne Potential

The Argonne potential is one of the conventional model of the NN interactions [5]. The AV18 potential is an updated version of AV14 potential [22] and consists of three parts: an electro-magnetic (EM) part, a OPE part and an intermediate- and short-range phenomenological part. The sum of the EM and OPE parts is the long-range part of the potential. The intermediate-range part is assumed to come from two-pion exchange processes and is expressed as the square of the tensor function. The short-range part is given as a Woods-Saxon shaped potential whose parameters are determined by fitting data. The sum of these parts of the potential is rewritten as a sum of 18 operator components, O_{ij}^p:

$$v_{ij} = \sum_{p=1}^{18} v_p(\boldsymbol{r}_{ij}) O_{ij}^p. \tag{1.1}$$

The first 14 operators are charge-independent ones:

$$O_{ij}^{p=1,14} = [1, (\boldsymbol{\sigma}_i \cdot \boldsymbol{\sigma}_j), S_{ij}, (\boldsymbol{L} \cdot \boldsymbol{S}), \boldsymbol{L}^2, \boldsymbol{L}^2(\boldsymbol{\sigma}_i \cdot \boldsymbol{\sigma}_j), (\boldsymbol{L} \cdot \boldsymbol{S})^2] \otimes [1, (\boldsymbol{\tau}_i \cdot \boldsymbol{\tau}_j)], \tag{1.2}$$

where $\boldsymbol{\sigma}$ and $\boldsymbol{\tau}$ are the spin and isospin operator, respectively. $\boldsymbol{L}$ is the relative orbital angular momentum and $\boldsymbol{S}$ is the total spin of the nucleon pair. S_{ij} is the usual tensor operator written as,

$$S_{ij} = 3(\boldsymbol{\sigma}_i \cdot \hat{\boldsymbol{r}}_{ij})(\boldsymbol{\sigma}_j \cdot \hat{\boldsymbol{r}}_{ij}) - (\boldsymbol{\sigma}_i \cdot \boldsymbol{\sigma}_j). \tag{1.3}$$

The remaining operators are charge-dependent, which are given by,

$$O_{ij}^{p=15,18} = T_{ij},\ (\boldsymbol{\sigma}_i \cdot \boldsymbol{\sigma}_j) T_{ij},\ S_{ij} T_{ij},\ \tau_{z_i} + \tau_{z_j}, \tag{1.4}$$

where T_{ij} is the isotensor operator written as,

$$T_{ij} = 3\tau_{z_i}\tau_{z_j} - (\boldsymbol{\tau}_i \cdot \boldsymbol{\tau}_j). \tag{1.5}$$

The parameters of the AV18 potential fit the Nijmegen database [4] with χ^2/datum = 1.09.

1.2.2 Bonn Potential

The Bonn potential is based on various boson exchanges for the NN interaction below pion production threshold [23]. This potential contains an explicit 2π-exchange contribution which is taken into account virtual isobar excitation and direct $\pi\pi$-interactions. Higher-order diagrams involving heavy-meson exchanges are also taken into account. In particular, the combination of π- and ρ-mesons is crucial for a quantitative description of the phase shifts at low angular momentum of NN scattering.

The couplings for the various mesons in meson-nucleon-nucleon vertices are given in terms of their interaction Lagrangian densities for pseudoscalar (π, η), scalar (σ, δ) and vector mesons (ρ, ω):

$$\mathscr{L}_{NNps} = -g_{ps}\bar{\psi}i\gamma^5\psi\phi^{(ps)}, \tag{1.6}$$

$$\mathscr{L}_{NNs} = g_s\bar{\psi}\psi\phi^{(s)}, \tag{1.7}$$

$$\mathscr{L}_{NNv} = -g_v\bar{\psi}\gamma^\mu\psi\phi^{(v)}_\mu - \frac{f_v}{4M}\bar{\psi}\sigma^{\mu\nu}\psi(\partial_\mu\phi^{(v)}_\nu - \partial_\nu\phi^{(v)}_\mu), \tag{1.8}$$

where ψ denotes the nucleon Dirac spinor field. $\phi^{(ps)}$, $\phi^{(s)}$ and $\phi^{(v)}$ are the pseudoscalar, scalar and vector boson field, respectively. M is the nucleon mass. g_α and f_α are coupling constants. Correspondingly, the vertices in meson-nucleon-isobar are given by

$$\mathscr{L}_{N\Delta\pi} = \frac{f_{N\Delta\pi}}{m_\pi}\bar{\psi}T\psi_\mu\partial^\mu\phi_\pi + \text{h.c.}, \tag{1.9}$$

$$\mathscr{L}_{N\Delta\rho} = i\frac{f_{N\Delta\rho}}{m_\rho}\bar{\psi}\gamma^5\gamma_\mu T\psi_\nu(\partial^\mu\phi^\nu_\rho - \partial^\nu\phi^\mu_\rho) + \text{h.c.}, \tag{1.10}$$

where ψ_μ is the field operator describing the Δ-isobar. T is the isospin operator and h.c. denotes hermitian conjugate.

The first-order contributions come from the one-pion and one-omega exchanges (see Fig. 1.2). The pion provides the long-ranged tensor force and the ω-meson provides the short-ranged repulsive central force as well as the spin-orbit force. The scalar isovector δ-meson (4π-resonance, $M_\delta = 983$ MeV) provides the isospin-dependent central force which has a very small contribution used for a consistent description of both S-wave ($^1S_0$ and $^3S_1$) phase shifts. The η- and η'-meson exchanges are left out in this potential because the contributions of these particles are small.

The Bonn potential contains the 2π-contributions coming from nucleon resonances (Δ-isobar) as well as a direct $\pi\pi$ interaction as shown in Fig. 1.3. The two-pion exchange contributions play a important role for the long- and intermediate-range parts of the NN

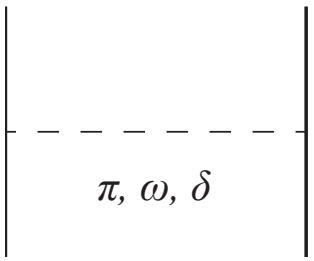

Figure 1.2: Diagram of single-meson exchange included in the Bonn potential.

interaction as described in phase shifts at higher angular momenta. In Fig. 1.3, the six upper diagrams represent uncorrelated 2π-exchange and those at the second line from the bottom represent the correlated S-wave contribution. The correlated $\pi\pi$ S-wave contribution can be approximated by the exchange of a scalar isoscalar boson (σ') with a broad mass distribution. The $\pi\pi$ S-wave interaction contained this contribution is determined from the empirical $\pi\pi$ S-wave phase shifts. The correlated 2π P-wave contribution is described by the ρ-meson exchange shown in the bottom of Fig. 1.3.

From the OBE model it is known that there is a strong cancellation between the contributions of the single π- and ρ-meson exchanges. Therefore, the Bonn potential includes the ρ and π two-boson-exchange diagrams, expecting them to counterbalance corresponding 2π contributions, as shown in Fig. 1.4.

Due to the fact that the $\pi\rho$ diagrams essentially contribute the NN interaction, the Bonn potential includes additional classes of the 3π- and 4π-exchanges. Figure 1.5 shows all diagrams included in the Bonn full model.

The latest version of the potential is charge-dependent Bonn (CD-Bonn) potential based upon the philosophy of the Bonn potential for charge symmetry and charge independence breaking [6]. The parameters of this potential fit 5990 NN scattering data which are the sum of the Nijmegen database [4] and the data published before 2000 with χ^2/datum = 1.02. The charge symmetry breaking (CSB) in the NN force is caused by the difference between the masses of protons and neutrons. The Bonn group supposed that irreducible diagrams of π and γ exchanges between two nucleons provide a charge-dependent nuclear force because the empirically known CSB can be explained from nucleon mass splitting. The major source of charge independence breaking (CIB) in the nuclear force is pion mass splitting. The CIB effect mainly comes from the OPE diagram which accounts for about 50 % of the difference between the empirical scattering lengths of pp and np scatterings. In addition, the potential includes two other sources for the CIB: the diagrams of two-

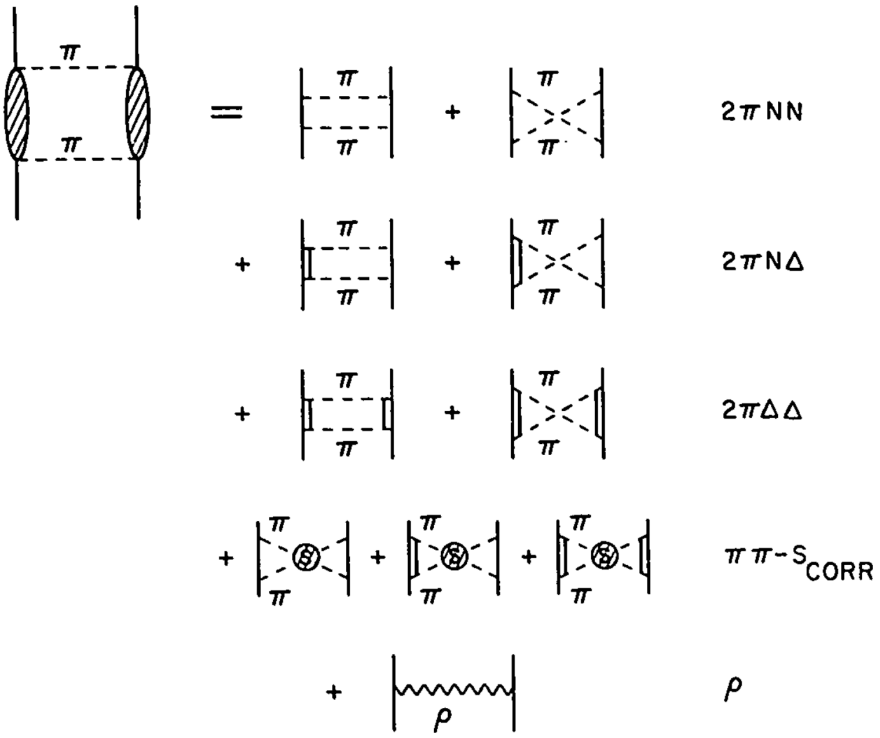

Figure 1.3: 2π-exchange contribution in the Bonn potential. Figure taken from Ref. [23].

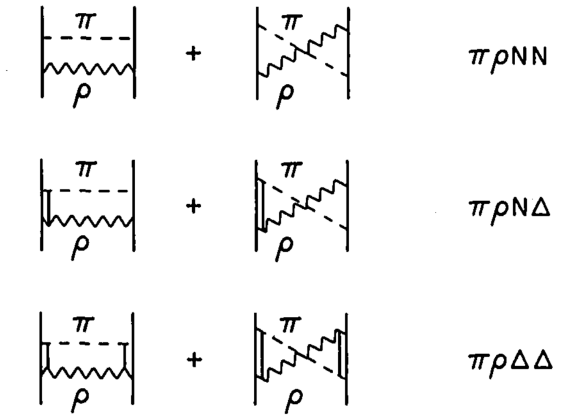

Figure 1.4: $\pi\rho$ contributions to the NN interactions in the Bonn potential. Figure taken from Ref. [23].

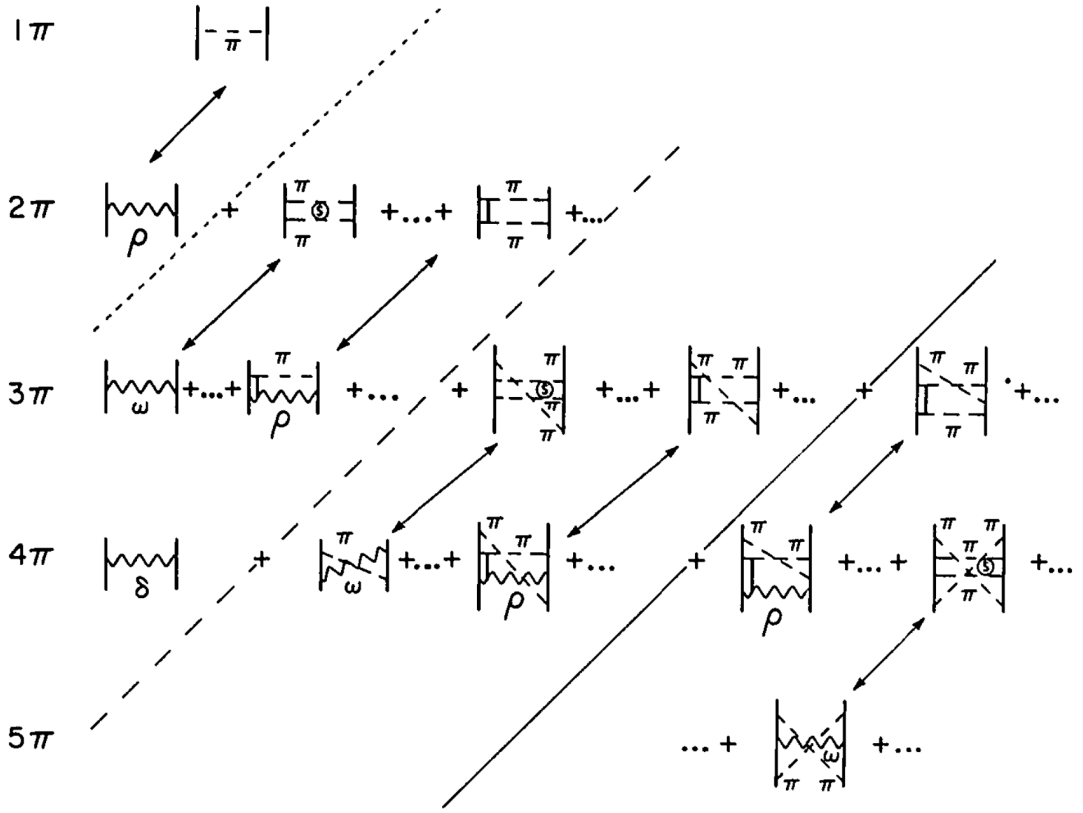

Figure 1.5: Diagrammatic expansion of the meson-exchange NN interaction. All diagrams above and left of the solid line are included in the Bonn full model. The arrows denote terms should be grouped together. Figure taken from Ref. [23].

boson exchange and irreducible $\pi\gamma$ exchange. Therefore, the CD-Bonn potential includes considerably more charge dependence than other realistic potentials such as AV18 and Nijmegen potentials.

1.2.3 Nijmegen Potential

The Nijmegen group has presented three high-quality NN potentials [7]: a nonlocal Reid-like Nijmegen potential (Nijm I), a local version (Nijm II) and an updated regularized version (Reid93) of the Reid soft-core potential. All these three potentials fit the Nijmegen database [4] with the same accuracy of χ^2/datum = 1.03. The potentials are based upon the OBE potentials with momentum-dependent central terms and exponential form factors. These potentials have rotational, reflectional and time reversal invariance, and are written as the sum of six independent terms,

$$V = \sum_{i=1}^{6} V_i P_i. \tag{1.11}$$

A common choice for the six operators in momentum space is given by,

$$\begin{aligned} P_1 &= 1, \\ P_2 &= \boldsymbol{\sigma}_1 \cdot \boldsymbol{\sigma}_2, \\ P_3 &= (\boldsymbol{\sigma}_1 \cdot \boldsymbol{k})(\boldsymbol{\sigma}_2 \cdot \boldsymbol{k}) - \frac{1}{3}\boldsymbol{k}^2(\boldsymbol{\sigma}_1 \cdot \boldsymbol{\sigma}_2), \\ P_4 &= \frac{i}{2}(\boldsymbol{\sigma}_1 + \boldsymbol{\sigma}_2) \cdot \boldsymbol{n}, \\ P_5 &= (\boldsymbol{\sigma}_1 \cdot \boldsymbol{n})(\boldsymbol{\sigma}_2 \cdot \boldsymbol{n}), \\ P_6 &= \frac{i}{2}(\boldsymbol{\sigma}_1 - \boldsymbol{\sigma}_2) \cdot \boldsymbol{n}, \end{aligned} \tag{1.12}$$

where $\boldsymbol{k} = \boldsymbol{p}_f - \boldsymbol{p}_i$, $\boldsymbol{q} = (\boldsymbol{p}_f + \boldsymbol{p}_i)/2$, and $\boldsymbol{n} = \boldsymbol{q} \times \boldsymbol{k}$ are the momentum vectors in terms of initial and final momenta, $\boldsymbol{p}_i$ and $\boldsymbol{p}_f$. The six potential forms V_i are parameterized for each partial wave separately. The free parameters are optimized by the fitting to the NN data and comparing the predicted phase shifts of the Nijmegen NN multienergy PWA below 350 MeV [4].

1.3 Three-Nucleon Force

As described above, most of the present-day 3NF models are based on a refined version of the Fujita-Miyazawa type 3NF incorporating a two-pion exchange process with the

Δ-isobar excitation in the intermediate state. In the following sections, we describe the 3NF models often used in the theoretical calculations as well as an alternative theoretical description which gives an effective 3NF.

1.3.1 Tucson-Melbourne 3NF

The general from of the two-pion exchange 3NF is derived from the low-momentum expansion of the off-mass-shell πN scattering amplitude. The Tucson-Melbourne (TM) 3NF model [13–15] is based on current-algebra and partially conserved axial-vector current (PCAC) constraints. The full potential is given by [24, 25],

$$
\begin{aligned}
V_{\rm 3NF} &= \sum_{i=1}^{3} V_{\rm 3NF}^{(i)}, \\
V_{\rm 3NF}^{(3)} &= \frac{g^2}{4m_N^2} \frac{\boldsymbol{\sigma}_1 \cdot \boldsymbol{q}}{\boldsymbol{q}^2 + m_\pi^2} \frac{\boldsymbol{\sigma}_2 \cdot \boldsymbol{q'}}{\boldsymbol{q'}^2 + m_\pi^2} F_{\pi NN}^2(\boldsymbol{q}^2) F_{\pi NN}^2(\boldsymbol{q'}^2) \left[O^{\alpha\beta} \tau_1^\alpha \tau_2^\beta \right], \qquad (1.13) \\
O^{\alpha\beta} &= \delta^{\alpha\beta} \left[a + b \boldsymbol{q} \cdot \boldsymbol{q'} + c(\boldsymbol{q}^2 + \boldsymbol{q'}^2) \right] - d(\tau_3^\gamma \epsilon^{\alpha\beta\gamma} \boldsymbol{\sigma}_3 \cdot \boldsymbol{q} \times \boldsymbol{q'}), \qquad (1.14)
\end{aligned}
$$

where δ functions, phase-space factors, etc., have been ignored. $V_{\rm 3NF}^{(i)}$ denotes a 3NF potential where the nucleon i is in the middle. g is the πN coupling constant. m_N and m_π are the mass for a nucleon and a pion, respectively. $\boldsymbol{\sigma}_i$ and $\boldsymbol{\tau}_i$ are the spin and isospin operator for the nucleon i. The initial and final pion momenta are expressed as $\boldsymbol{q}$ and $\boldsymbol{q'}$. α and β are the isospin labels of the initial and final pions. The coefficients a, b, c and d are determined from the πN scattering data. The a-term describes the πN S-wave scattering because this term is independent of the pion momenta. The b- and d-terms describe the πN P-wave scattering whose the main ingredient is the process $\pi N \to \Delta \to \pi N$ corresponding to the Fujita-Miyazawa type 3NF. It has been pointed out that the short-range c-term is unnatural under a chiral perturbation theory (ChPT) and should not be kept in Ref. [24]. For a more consistent form of the TM 3NF with chiral symmetry, the c-term is decomposed into a two-pion exchange term with the same structure as the a-term and a short-range/π-range term:

$$
\begin{aligned}
V_{\rm 3NF}|_{c-\rm term} &\propto \frac{\boldsymbol{q}^2}{\boldsymbol{q}^2 + m_\pi^2} \frac{1}{\boldsymbol{q'}^2 + m_\pi^2} + (q \leftrightarrow q') \\
&= \frac{\boldsymbol{q}^2 + m_\pi^2 - m_\pi^2}{\boldsymbol{q}^2 + m_\pi^2} \frac{1}{\boldsymbol{q'}^2 + m_\pi^2} + (q \leftrightarrow q') \\
&= \left(1 - \frac{m_\pi^2}{\boldsymbol{q}^2 + m_\pi^2} \right) \frac{1}{\boldsymbol{q'}^2 + m_\pi^2} + (q \leftrightarrow q'). \qquad (1.15)
\end{aligned}
$$

Table 1.1: Triton binding energies E_t predicted by various realistic NN potentials with and without the TM 3NF. The last column shows the adjusted cut-off parameters Λ in the 3NF model [27].

Potential	E_t [MeV] (w/o 3NF)	E_t [MeV] (with 3NF)	Λ/m_π
CD-Bonn	7.953	8.483	4.856
AV18	7.576	8.479	5.215
Nijm I	7.731	8.480	5.147
Nijm II	7.709	8.477	4.990
Exp.	8.4817986(24) [MeV]		

Including the two-pion exchange part of the c-term, one can leads to a redefinition of a as $a' \equiv a - 2m_\pi^2 c$. It is required that the short-range/π-range term is rejected and the value of a is replaced as a' from the ChPT. This new form of TM 3NF is called TM' 3NF [24–26].

The TM 3NF also has a strong form factor:

$$F_{\pi NN}(\boldsymbol{q}^2) = \frac{\Lambda^2 - m_\pi^2}{\Lambda^2 + \boldsymbol{q}^2}. \tag{1.16}$$

The cut-off parameter Λ is chosen to the appropriate value so that the ^{3}H binding energy is reproduced for each NN potentials (see Table 1.1) [27].

1.3.2 Urbana/Illinois 3NF

Urbana IX model:

The Urbana IX (UIX) model is based on the two-pion exchange 3NF and the short-range phenomenological term [16]. The original form of this potential is written as a sum of two-pion exchange and short-range phenomenological terms,

$$V_{ijk} = V_{ijk}^{2\pi} + V_{ijk}^{R}. \tag{1.17}$$

The two-pion exchange term is expressed as,

$$V_{ijk}^{2\pi} = \sum_{\text{cyclic}} A_{2\pi} \left(\{X_{ij}^\pi, X_{jk}^\pi\}\{\boldsymbol{\tau}_i \cdot \boldsymbol{\tau}_j, \boldsymbol{\tau}_j \cdot \boldsymbol{\tau}_k\} + \frac{1}{4}[X_{ij}^\pi, X_{jk}^\pi][\boldsymbol{\tau}_i \cdot \boldsymbol{\tau}_j, \boldsymbol{\tau}_j \cdot \boldsymbol{\tau}_k] \right), \tag{1.18}$$

where $A_{2\pi}$ is the interaction strength. X_{ij} is constructed with an average pion mass,

$$m_\pi = \frac{1}{3} m_{\pi^0} + \frac{2}{3} m_{\pi^\pm}, \tag{1.19}$$

and given by,

$$X_{ij}^{\pi} = Y(m_\pi r_{ij})(\boldsymbol{\sigma}_i \cdot \boldsymbol{\sigma}_j) + T(m_\pi r_{ij}) S_{ij}, \tag{1.20}$$

$$Y(m_\pi r) = \frac{e^{-m_\pi r}}{m_\pi r}\left(1 - e^{-cr^2}\right), \tag{1.21}$$

$$T(m_\pi r) = \left[1 + \frac{3}{m_\pi r} + \frac{3}{(m_\pi r)^2}\right] \frac{e^{-m_\pi r}}{m_\pi r}\left(1 - e^{-cr^2}\right)^2, \tag{1.22}$$

where S_{ij} is the tensor operator shown in Eq. (1.3). A cut-off parameter c in $Y(m_\pi r)$ and $T(m_\pi r)$ is specified in Ref. [5]. The shorter-range phenomenological term is expressed as,

$$V_{ijk}^{R} = \sum_{\text{cyclic}} U_0 T_\pi^2(m_\pi r_{ij}) T_\pi^2(m_\pi r_{jk}). \tag{1.23}$$

The parameters for UIX model are $A_{2\pi} = -0.0293$ MeV and $U_0 = 0.0048$ MeV. These parameters have been determined by fitting the density of nuclear matter and the ^{3}H binding energy in combination with the AV18 interaction.

Illinois model:

The Illinois 3NF model is the updated version of the UIX model [16] and is obtained by fitting the energies of all the 17 bound or narrow states of $3 \leq A \leq 8$ nuclei [8]. The calculation was performed in combination with the AV18 NN potential using the GFMC method with an error of less than 2 %. The results significantly improve the binding energies of the p-shell nuclei.

The Illinois model includes the two-pion exchange term due to the πN scattering in S-wave and the 3π exchange term due to ring diagrams with a Δ intermediate state in addition to the UIX model terms. The potential is expressed as,

$$\begin{aligned} V_{ijk} &= V_{2\pi}^{PW} + V_{2\pi}^{SW} + V_{3\pi}^{\Delta R} + V_R \\ &= A_{2\pi}^{PW} O_{ijk}^{2\pi,PW} + A_{2\pi}^{SW} O_{ijk}^{2\pi,SW} + A_{3\pi}^{\Delta R} O_{ijk}^{3\pi,\Delta R} + A_R O_{ijk}^{R}, \end{aligned} \tag{1.24}$$

where $A_{2\pi}^{PW}$, $A_{2\pi}^{SW}$, $A_{3\pi}^{\Delta R}$ and A_R are strengths for the four interaction terms, $V_{2\pi}^{PW}$, $V_{2\pi}^{SW}$, $V_{3\pi}^{\Delta R}$ and V_R, respectively. In the UIX model, $A_{2\pi}^{PW}$ is denoted by $A_{2\pi}$ and A_R by U_0.

The two-pion exchange term of the πN P-wave scattering $V_{2\pi}^{PW}$ is due to the Fujita-Miyazawa type 3NF shown in Fig. 1.6 (a). The form of $V_{2\pi}^{SW}$ caused by the πN S-wave scattering illustrated in Fig. 1.6 (b) is given by,

$$O_{ijk}^{2\pi,SW} = \sum_{\text{cyclic}} Z(m_\pi r_{ij}) Z(m_\pi r_{jk}) \boldsymbol{\sigma}_i \cdot \hat{\boldsymbol{r}}_{ij} \boldsymbol{\sigma}_k \cdot \hat{\boldsymbol{r}}_{kj} \boldsymbol{\tau}_i \cdot \boldsymbol{\tau}_k, \tag{1.25}$$

$$Z(m_\pi r) = \frac{m_\pi r}{3}[Y(m_\pi r) - T(m_\pi r)]. \tag{1.26}$$

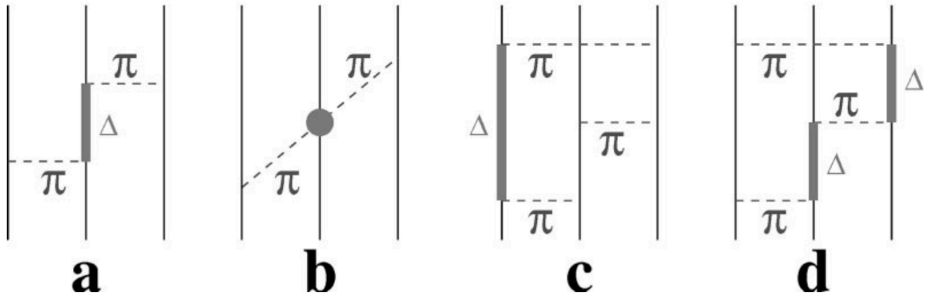

Figure 1.6: 3NF Feynman diagrams in the Illinois 3NF model. The first (a) is the Fujita-Miyazawa type 3NF, (b) is the two-pion exchange in S-wave, (c) and (d) are 3π ring diagrams with one Δ in intermediate states. Figure taken from Ref. [8].

It is difficult to determine its strength $A_{2\pi}^{SW}$ from the data because the contribution of $V_{2\pi}^{SW}$ to nuclear energies is rather small. Therefore, $A_{2\pi}^{SW}$ is assumed to be 0 or -1.0 MeV as in modern ChPT potentials [24]. The 3π exchange term $V_{3\pi}^{\Delta R}$ is based on the 3π exchange ring diagrams shown in Fig. 1.6 (c) and (d). These diagrams have only one Δ at a time in the intermediate states. The $V_{3\pi}^{\Delta R}$ is approximately given as the sum of terms derived from these diagrams. Finally, the form of $V_{3\pi}^{\Delta R}$ is expressed as,

$$O_{ijk}^{3\pi,\Delta R} = \frac{50}{3} S_\tau^I S_\sigma^I + \frac{26}{3} A_\tau^I A_\sigma^I + \frac{2}{9} \sum_{\text{cyclic}} (S_\sigma^I S_{\tau,ijk}^D + S_\tau^I S_{\sigma,ijk}^D + A_\tau^I A_{\sigma,ijk}^D + 13 S_{\tau,ijk}^D S_{\sigma,ijk}^D), \quad (1.27)$$

where S and A are operators that are symmetric and antisymmetric under the exchange of j with k. Subscripts τ and σ denote that the operators contain isospin and spin-space parts. Superscripts I and D indicate that the operators are independent or dependent on the cyclic permutation of ijk. Interesting dependence on the total isospin T_{tot} is found in the $V_{3\pi}^{\Delta R}$. The isospin operator S_τ^I is given as,

$$\begin{aligned} S_\tau^I &= 2 + \frac{2}{3}(\boldsymbol{\tau}_i \cdot \boldsymbol{\tau}_j + \boldsymbol{\tau}_j \cdot \boldsymbol{\tau}_k + \boldsymbol{\tau}_k \cdot \boldsymbol{\tau}_i) \\ &= \frac{4}{3} T_{tot}^2 - 1. \end{aligned} \quad (1.28)$$

Accordingly, the first term of $V_{3\pi}^{\Delta R}$ is zero in the isospin channels of $T_{tot} = 1/2$, i.e. in Nd elastic scattering as well as $A = 3, 4$ bound states. In contrast, A_τ^I is zero in $T_{tot} = 3/2$ states. The strengths $A_{2\pi}^{PW}$, $A_{3\pi}^{\Delta R}$ and A_R are determined by fitting the nuclear energies.

1.3.3 Formalism with Explicit Δ-Isobar Excitation

An alternative theoretical description that provides an effective 3NF is formulated by the Hannover-Lisbon group [28]. They take an extended Hilbert space to allow the explicit excitation of a nucleon to a Δ-isobar, which is considered as a stable particle rather than a dynamic πN system. A two-baryon coupled channel potential in NN and $N\Delta$ space was constructed referring to the CD-Bonn potential as a NN part, and using a transition potential from NN state to $N\Delta$ state derived from π- and ρ-meson exchange. Parameters of the coupled channel potential are tuned to the NN phase shifts of the CD-Bonn model [28].

The resulting coupled-channel potential, CD-Bonn+Δ, is applied to $3N$ systems [28] and later to $4N$ systems [29]. Although the CD-Bonn+Δ potential fails to give the correct binding energy of ^{3}H, it provides similar results for $3N$ scattering observables to those based on the NN potentials combined with the TM and UIX 3NFs (see Sec. 1.5).

1.4 Chiral Perturbation Theory

The chiral perturbation theory is an effective field theory (EFT) based on the chiral symmetry of quantum chromodynamics (QCD) for implementing strong-interaction physics in low-momentum regime [30]. The theory provides the most general effective Lagrangian involving all possible terms such as low-energy nucleons as well as pions consistent with the spontaneously broken chiral symmetry. The Lagrangian has an infinite number of the unknown low-energy constants (LECs). Thus, the effective Lagrangian is used to compute low-energy observables via an expansion in powers of Q/Λ_χ. Q is the soft scale associated with external momenta or the mass of pions. Λ_χ denotes the hard scale which is set to hadronic scale ~ 1 GeV and is so-called the chiral symmetry breaking scale. The interaction in the Lagrangian is organized by the power ν of the expansion parameter Q/Λ_χ, and is expressed as the sum of each order [24]:

$$\mathcal{L}_{\text{eff}} = \mathcal{L}^{(\nu=0)} + \mathcal{L}^{(\nu=1)} + \mathcal{L}^{(\nu=2)} + \cdots . \tag{1.29}$$

Epelbaum *et al.* constructed the nuclear potential based on the ChEFT using the unitary transformation method [31]. In this theory, the two- or many-nucleon potentials

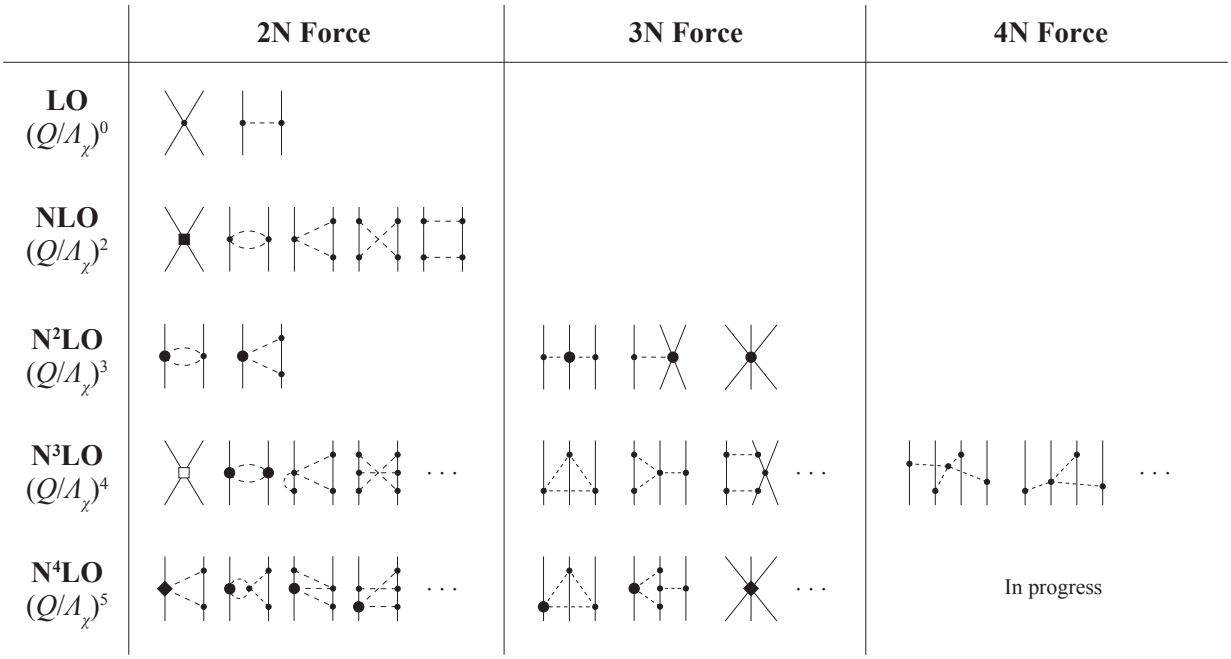

Figure 1.7: Hierarchy of the nuclear force diagrams in the ChEFT [40]. Solid and dashed lines represent nucleons and pions, respectively. Solid dots, filled circles, filled and open squares and filled diamonds refer to vertices of the Lagrangian.

are naturally derived on an equal footing in the hierarchy as [32, 33],

$$V_{\rm 2N} = V_{\rm 2N}^{(0)} + V_{\rm 2N}^{(2)} + V_{\rm 2N}^{(3)} + V_{\rm 2N}^{(4)} + \cdots , \tag{1.30}$$

$$V_{\rm 3N} = V_{\rm 3N}^{(3)} + V_{\rm 3N}^{(4)} + \cdots , \tag{1.31}$$

$$V_{\rm 4N} = V_{\rm 4N}^{(4)} + \cdots , \tag{1.32}$$

as shown in Fig. 1.7. The first non-vanishing 3NF diagram appears at next-to-next-to-leading order ($\rm N^2LO$). The 3π ring diagrams contribute from $\rm N^3LO$. Recently two-nucleon sector of the ChPT has achieved to the level of high-precision. Semilocal momentum-space regularized chiral two-nucleon potentials up to fifth order [34], called $\rm N^4LO^+$, reproduce the *pp* (*np*) data from the 2013 Granada database [35] up to 300 MeV with an accuracy of $\chi^2/\text{datum} = 1.00$ (1.06). In parallel with the development on NN potential theoretical treatment of 3NFs based on the ChPT is being pushed to the fifth order [36–39].

1.5 Study of Three-Nucleon Force in Few-Nucleon Scattering

Nuclear forces have dynamical properties such as momentum dependence, spin and isospin dependence. Few-nucleon scattering is one of a good probe to investigate in detail the properties of nuclear forces including 3NFs. Precise measurements of differential cross sections and various spin observables can extract the detailed information of nuclear forces.

Due to the development of the realistic NN potentials described above and the improvement of the computational technology, it has become possible to perform the model-independent rigorous numerical calculations for the scattering observables of few-nucleon systems. Comparing the experimental data and the theoretical predictions, one can quantitatively discuss the 3NF effects. For the Nd scattering, the simplest $3N$ scattering system, the comparison between the high-precision data and the rigorous numerical calculations based on the Faddeev equation was performed up to 200 MeV [41]. The calculation reproduces the scattering observables except for the deuteron vector and tensor analyzing power using only the NN potentials at low energies of less than 20 MeV/nucleon. Therefore, it was found that the 3NF effects are relatively small compared to those of the 2NF at low-energy regions.

The first signature of 3NF effect in $3N$ scattering was indicated for Nd elastic scattering at above 60 MeV/nucleon by Witała *et al.* in 1998 [42]. They performed the Faddeev calculation using the modern NN interactions combined with the TM 3NF for the differential Nd cross section at 12, 65, 140 and 200 MeV/nucleon. Although the 3NF contribution is negligible at 12 MeV, the theoretical predictions of the NN potential underestimate the experimental data in the angular range of the minima at higher energies. The discrepancy between the data and the theoretical calculation increases with an incident energy. This discrepancy is removed by incorporating the TM 3NF with a cut-off Λ of which was adjusted to reproduce the ^{3}H binding energy. Thus, the result have shown that *the minima of the elastic Nd scattering cross sections are probably a smoking gun for 3NF effects* [42].

RIKEN group carried out the high-precise measurement of the elastic Nd scattering at intermediate energies with the aim of studying the 3NF effects [43–47]. Figure 1.8 shows the measured angular distribution of the differential cross section for dp elastic scattering at 70 and 135 MeV/nucleon. The rigorous numerical Faddeev calculations based on the modern NN potentials with or without the 3NF are also shown. It is clearly seen the large discrepancies between the experimental data and the rigorous Faddeev calculations

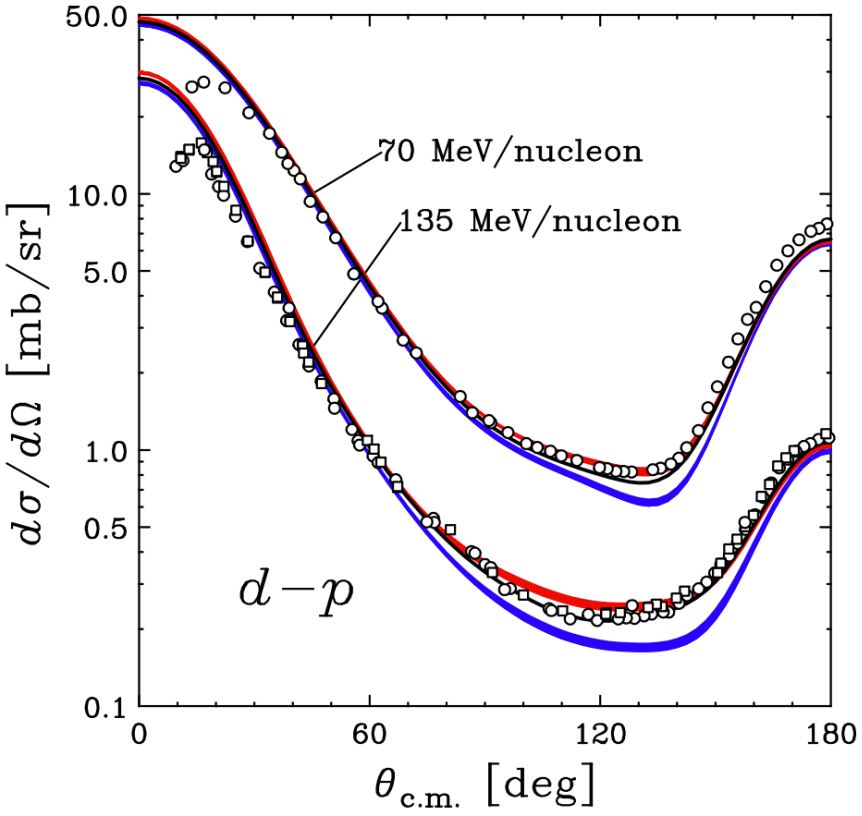

Figure 1.8: Differential cross section for dp elastic scattering with incident energies of 70 and 135 MeV/nucleon [45]. The data are shown by open circles. The blue bands are the theoretical predictions based on the modern NN potentials; CD-Bonn, AV18 and Nijmegen I, II. The red bands and the solid lines show the predictions based on the modern NN potential with TM'99 3NF and AV18 2NF with UIX 3NF, respectively.

with only the modern NN potentials at the minima of the differential cross section. The discrepancies at the forward angles are due to Coulomb interactions. Including the 3NF model, the theoretical predictions remove these discrepancies and reproduce the experimental data very well. This result is taken as the clearest signature of the 3NF effects in $3N$ scattering system. Meanwhile the measured spin observables are not always explained even by incorporating the 3NFs, which shows deficiencies in the spin dependencies of the 3NF models applied in the theoretical calculations [45, 47]. In view of understanding spin dependent parts of 3NFs theoretical treatments based on the chiral effective field theory are currently in progress [39].

The study of 3NFs via the Nd scattering at intermediate energies has provided a solid

basis to explore the properties of 3NFs. Importance of the 3NF effects was suggested in four or more nucleon system as well as the equation of state of nuclear matter. The GFMC calculations including the Illinois 3NF provide the significant improvements for the binding energies of the p-shell nuclei including neutron-rich nuclei [8, 48]. As described in Sec. 1.3.2, in the Illinois 3NF, the 3π-exchange ring diagram with a Δ intermediate state which is sensitive to the total isospin $T = 3/2$ is considered. This $T = 3/2$ component plays an important role in describing the binding energies, especially in neutron-rich nuclei. Importance of the $T = 3/2$ component is also indicated in the pure neutron matter and the properties of neutron stars [10, 49].

1.6 Study of Three-Nucleon Force in p–^{3}He Elastic Scattering

The p–^{3}He scattering is one of the simplest scattering system in which the total isospin $T = 3/2$ channel of 3NFs can be investigated. For the Nd scattering system, the total isospin channel is limited to $T = 1/2$. Two-nucleon pairs with the isospin of $I = 1$ in ^{3}He nucleus [50] coupled with another proton can provide the system with the total isospin of $T = 3/2$ in the p–^{3}He system. In order to explore the properties of 3NFs in $4N$ system, it is indispensable to obtain differential cross sections as well as various spin observables; analyzing powers and spin-correlation coefficients.

In recent years rigorous numerical calculations for $4N$ scattering are becoming available, and remarkable theoretical investigations of 3NF effects in p–^{3}He elastic scattering have been reported. Viviani *et al.* presented theoretical analysis for p–^{3}He elastic scattering including 3NFs at low energies ($\leq$ 5.54 MeV) for the first time [51]. They calculated the observables by using the Kohn variational principle and the hyper-spherical harmonics technique to solve the $4N$ scattering problem. The nuclear potentials used are i) the ChEFT N^{3}LO 2NF combined with the N^{2}LO 3NF and ii) the AV18 2NF with the Illinois 3NF. Generally predicted 3NF effects at 5.54 MeV are small for all the measured observables as shown in Fig. 1.9. However, as an enlargement view around the peak region of ^{3}He analyzing power (see Fig. 1.10) shows, the difference is found between the 3NF models used in the calculations. Although the predicted 3NF effects are small at low energies the results indicate that ^{3}He analyzing power is quite sensitive to the particular component of 3NFs.

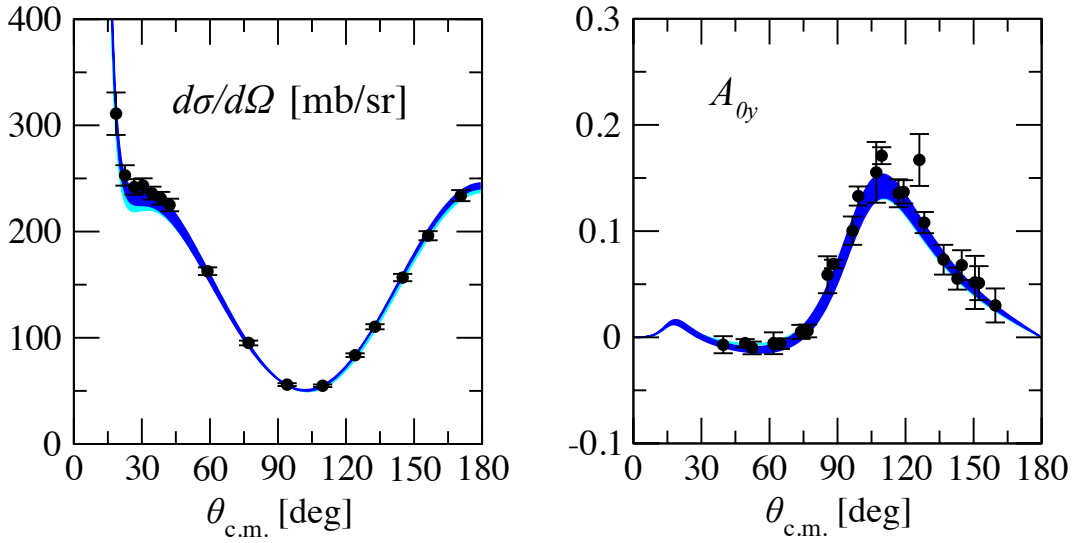

Figure 1.9: Differential cross section and ^{3}He analyzing power A_{0y} of p–^{3}He elastic scattering at $E_p = 5.54$ MeV [51]. The calculations with only the NN potential (light cyan band) or also including the 3NF (darker blue band) are shown.

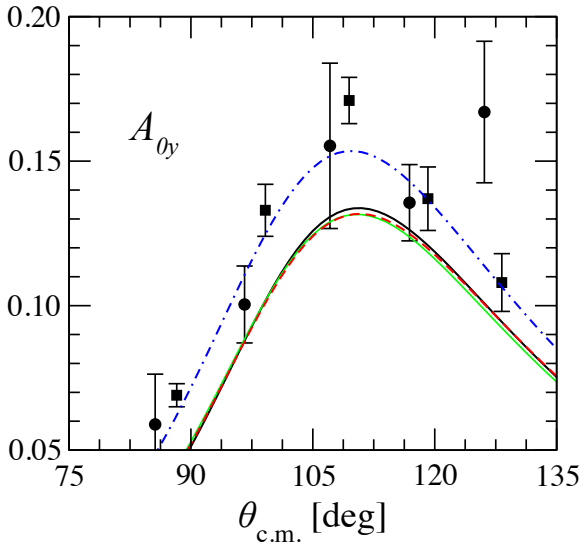

Figure 1.10: Enlargement view of ^{3}He analyzing power A_{0y} of p–^{3}He elastic scattering at $E_p = 5.54$ MeV [51]. The black solid, green solid, and dashed red lines denote the calculations based on the N^{3}LO 2NF and N^{2}LO 3NF derived from the ChEFT. The dot-dashed blue line is based on AV18 2NF with Illinois 3NF.

Deltuva and Fonseca have succeeded in performing the Alt, Grassberger, and Sandhas (AGS) calculation for p–^{3}He elastic scattering even above the $4N$ breakup threshold energy up to 35 MeV [52]. They used the realistic NN potentials for the calculations; the AV18, the inside-nonlocal outside-Yukawa (INOY04) [53, 54] and the CD-Bonn potentials. The INOY04 potential reproduces the experimental values of the ^{3}H and ^{3}He binding energies without an additional 3NF. Figure 1.11 shows the calculated ^{3}He analyzing power compared with the available data at proton energies from 7 to 35 MeV. The ^{3}He analyzing power varies slowly with increasing an incident energy and has a good agreement with the data over the whole energy range. They also studied the effect of 3NFs by using the CD-Bonn+Δ potential [28] for the differential cross section at 30.0 MeV (see Fig. 1.12). Discrepancy found in the cross section minimum between the data and the calculations based on the CD-Bonn potential is partially removed by the Δ-isobar effects. The feature obtained here is similar to what is observed in the cross section for Nd elastic scattering. Then it is expected that cross section minimum region for p–^{3}He elastic scattering could provide rich sources to explore 3NFs as going to an incident energy.

At energies below 35 MeV rich data sets for p–^{3}He elastic scattering are available, covering the cross section [55–58], proton analyzing power [59–62], ^{3}He analyzing power [59,62–64], and spin-correlation coefficients [59,62,65]. However at higher energies existing data bases are rather scare. The cross section data are obtained at 85 MeV [66], 100 MeV [67,68] and 150 MeV [68]. The proton analyzing powers are measured at 100 and 150 MeV [68]. The spin-correlation coefficient $C_{y,y}$ data are reported at 200, 300 and 400 MeV [69] but at the limited angle of $\theta_{\rm c.m.} = 180^\circ$. There exist few data for the ^{3}He analyzing power.

With the aim of pinning down 3NF effects in comparison with to the rigorous numerical $4N$ calculations recently developed and then approaching the total isospin channel of $T = 3/2$ of 3NFs, it is essential to obtain high precision data sets for p–^{3}He elastic scattering at intermediate energies ($E \gtrsim 60$ MeV). We plan to measure the complete set of the p–^{3}He elastic scattering at intermediate energies, that allows us to extract the scattering amplitudes. For the measurement of spin observables such as ^{3}He analyzing power as well as spin-correlation coefficients, we have constructed the polarized ^{3}He target.

1.7 Required Conditions for the Polarized ^{3}He Target

We describe the requirements of the polarized ^{3}He target for the measurement of ^{3}He analyzing power with sufficient accuracy. Assuming that the effect of 3NFs in p–^{3}He

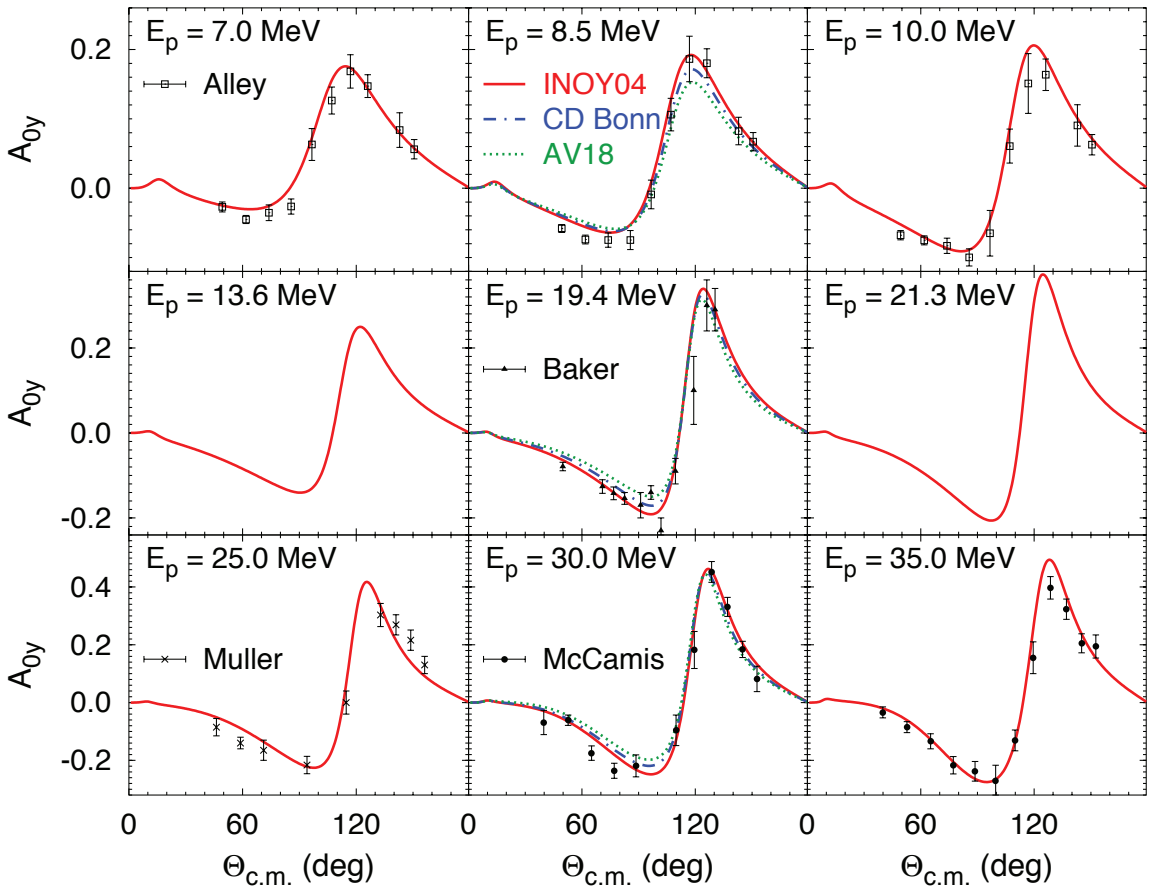

Figure 1.11: ^{3}He analyzing power for elastic p–^{3}He scattering at 7.0, 8.5, 10.0, 13.6, 19.4, 21.3, 25.0, 30.0, and 35.0 MeV. The solid, dashed-dotted and dotted curves are the calculations based on the INOY04, CD-Bonn and AV18 potentials, respectively. Figure taken from Ref. [52].

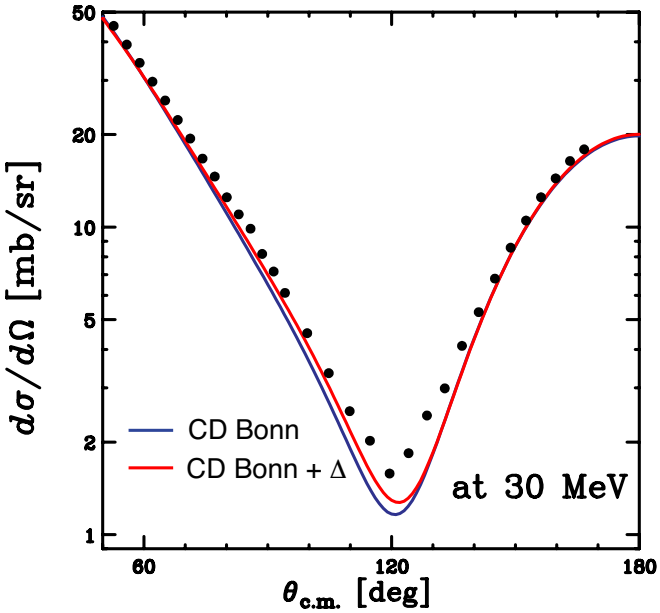

Figure 1.12: Differential cross section for elastic p–^{3}He scattering at 30.0 MeV [52]. The calculations obtained with the CD-Bonn (black solid line) and the CD-Bonn+Δ (red solid line) potentials are compared with the data.

scattering system is the same order of that in dp scattering, we require that the statistical error of ^{3}He analyzing power is about less than 0.02 for a detailed quantitative discussion of 3NFs.

The differential cross section for p–^{3}He elastic scattering is formulated as,

$$\frac{d\sigma}{d\Omega} = \left(\frac{d\sigma}{d\Omega}\right)_0 (1 + \boldsymbol{p} \cdot \boldsymbol{A}), \tag{1.33}$$

where $d\sigma/d\Omega$ ($(d\sigma/d\Omega)_0$) is the polarized (unpolarized) differential cross section. $\boldsymbol{p}$ denotes the polarization of the ^{3}He target, and $\boldsymbol{A}$ is the ^{3}He analyzing power. The coordinate system of the spin axis of the polarized target is defined by following the Madison convention [70]. A schematic view of the coordinate system for the p–^{3}He scattering experiment is shown in Fig. 1.13. According to the Madison convention, the z-axis is taken along to the direction of the projectile momentum $\boldsymbol{k}_{\rm in}$. The y-axis is taken along $\boldsymbol{k}_{\rm in} \times \boldsymbol{k}_{\rm out}$, where $\boldsymbol{k}_{\rm out}$ denotes the direction of the scattered particle. The x-axis is defined as $\hat{\boldsymbol{y}} \times \hat{\boldsymbol{z}}$. From Eq. (1.33) and the Madison convention, the yields of scattered protons at the angle θ are

expressed by,

$$
\begin{aligned}
L_\uparrow &= L_0[1 + p_y A_{0y}(\theta)], && (1.34)\\
L_\downarrow &= L_0[1 - p_y A_{0y}(\theta)], && (1.35)\\
R_\uparrow &= R_0[1 - p_y A_{0y}(\theta)], && (1.36)\\
R_\downarrow &= R_0[1 + p_y A_{0y}(\theta)], && (1.37)
\end{aligned}
$$

where L and R denote the yields of p–^{3}He elastic events in the left- and the right-side of the target. The spin axis of the polarized target is aligned to the y-axis. The subscripts $\uparrow$ and $\downarrow$ refer to spin directions of the target. The subscript 0 denotes the yields with the unpolarized target. Thus, the ^{3}He analyzing power A_{0y} is given by,

$$
A_{0y} = \frac{1}{p_y}\frac{L_\uparrow - L_\downarrow}{L_\uparrow + L_\downarrow} = \frac{1}{p_y}\frac{R_\downarrow - R_\uparrow}{R_\uparrow + R_\downarrow}. \tag{1.38}
$$

The statistical error is obtained by,

$$
\begin{aligned}
dA_{0y} &= \sqrt{\left(\frac{\partial A_{0y}}{\partial Y_\uparrow}\right)^2 (dY_\uparrow)^2 + \left(\frac{\partial A_{0y}}{\partial Y_\downarrow}\right)^2 (dY_\downarrow)^2},\\
(dA_{0y})^2 &= \frac{1}{p_y^2}\frac{4}{(Y_\uparrow + Y_\downarrow)^4}[Y_\downarrow^2 (dY_\uparrow)^2 + Y_\uparrow^2 (dY_\downarrow)^2], && (1.39)
\end{aligned}
$$

where $Y \equiv L,\ R$. Assuming that $p_y A_{0y} \ll 1$ and $Y \equiv Y_\uparrow \sim Y_\downarrow$, Eq. (1.39) is rewritten as,

$$
(dA_{0y})^2 \sim \frac{1}{p_y^2}\frac{(dY)^2}{2Y^2}. \tag{1.40}
$$

The statistical error of yields is expressed as $dY = \sqrt{Y}$ since the elastic scattering events follow the Poisson distribution. Therefore, the statistical error of ^{3}He analyzing power is simplified as,

$$
(dA_{0y})^2 \sim \frac{1}{p_y^2}\frac{1}{2Y}. \tag{1.41}
$$

The yield of detected protons is given by,

$$
\begin{aligned}
Y &= N \cdot t,\\
&= I \cdot \rho_{\mathrm{T}} \cdot \Delta\Omega \cdot \epsilon \cdot \frac{d\sigma}{d\Omega} \cdot t, && (1.42)
\end{aligned}
$$

where N is the event rate and t is the measurement period. I is the flux of incident particles, ρ_{T} is the number of target particles per unit area, $\Delta\Omega$ is the solid angle of the

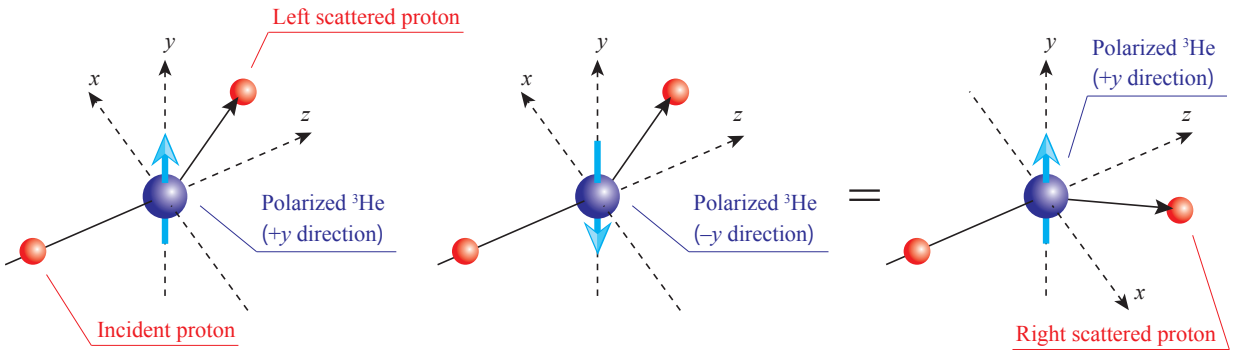

Figure 1.13: Schematic view of the coordinate system in the p–^{3}He scattering experiment with the polarized ^{3}He target defined by the Madison convention.

detector and ϵ is the detection efficiency, respectively. Using Eqs. (1.41) and (1.42), the statistical error of A_{0y} is expressed as,

$$(dA_{0y})^2 \sim \frac{1}{2p_y^2 \cdot \rho_{\rm T}} \frac{1}{I \cdot \Delta\Omega \cdot \epsilon \cdot \dfrac{d\sigma}{d\Omega} \cdot t}. \tag{1.43}$$

The statistical error is inversely proportional to the product of the target polarization p_y and the square root of $\rho_{\rm T}$. Therefore, it is necessary to the high-density and high-polarization target to reduce the statistical error.

We estimate the required conditions for the target using Eq. (1.43). The assumed experimental conditions are listed in Table 1.2. Using Eq. (1.43), the statistical error is calculated as,

$$\begin{aligned}(dA_{0y})^2 &\sim \frac{1}{2p_y^2 \cdot \rho_{\rm T}} \frac{1}{\dfrac{5\times10^{-9}}{1.6\times10^{-19}} \cdot 0.5\times10^{-3} \cdot 1 \cdot 0.5\times10^{-27} \cdot 5 \times 60^2}, \\ &\simeq \frac{3.56\times10^{15}}{p_y^2 \cdot \rho_{\rm T}\ [{\rm cm}^{-2}]}.\end{aligned} \tag{1.44}$$

Using the ^{3}He molar mass of 3.015 g/mol, Eq. (1.44) is rewritten as,

$$\begin{aligned}(dA_{0y})^2 &\sim \frac{3.56\times10^{15}}{p_y^2 \cdot \rho_{\rm T}}, \\ &= \frac{3.56\times10^{15}}{p_y^2 \cdot \rho \cdot l \cdot \dfrac{6.022\times10^{23}}{3.015}}, \\ &\simeq \frac{1.78\times10^{-8}}{p_y^2 \cdot \rho \cdot l},\end{aligned} \tag{1.45}$$

Table 1.2: Assumed conditions for the p–^{3}He scattering experiment.

Measurement period	t	5 [hours]
Beam intensity	$I \cdot e$	5 [nA]
Solid angle of the detector	$\Delta\Omega$	0.5 [msr]
Detection efficiency	ε	100%
Differential cross section at lab. system	$\frac{d\sigma}{d\Omega}$	0.5 [mb/sr]

where ρ is the density of the target in g/cm^3 and l is the target length in cm. Therefore, the required target condition is given by,

$$p_y^2 \cdot \rho \cdot l > \frac{1.78 \times 10^{-8}}{(0.02)^2} = 4.45 \times 10^{-5}. \tag{1.46}$$

The ^{3}He density at 0 C$^\circ$ and at 1 atm is 0.135 mg/cm^3. Assuming that the target density is 3 atm and the target length is 2 cm, the ^{3}He polarization of more than 25 % is needed to satisfy the required statistical error of the ^{3}He analyzing power.

In the previous work, the polarized ^{3}He target system was developed and the first measurement of ^{3}He analyzing power was performed at 70 MeV [71]. The ^{3}He analyzing power was obtained at the laboratory angles of 50°, 70°, 90° and 110°. However, the obtained ^{3}He analyzing power at the backward angle of 110° had poor statistical and systematic uncertainties mainly due to the low ^{3}He polarization of $\sim$ 7 %. Moreover the polarization gradient occurred in the double-chambered target cell, the importance for which we have found later in order to evaluate the absolute values of the polarizations of the ^{3}He target, was not taken into account.

In this work, we improved the ^{3}He polarization by introducing the alkali-hybrid spin exchange optical pumping (AH-SEOP) method and evaluated the absolute value of the ^{3}He polarization by studying the polarization gradient. Furthermore, the target polarization was also evaluated by the neutron transmission measurement. In addition a target cell with thinner surface was produced in order to obtain better energy resolution for p–^{3}He elastic scattering events. We performed the measurement of ^{3}He analyzing powers using the improved polarized ^{3}He target at intermediate energies; 70 and 100 MeV. The experiments were performed at Cyclotron and Radioisotope Center (CYRIC) in Tohoku University and Research Center for Nuclear Physics (RCNP) in Osaka University. In Chapter 2, we describe the principle of ^{3}He polarization production and our devices. The polarimetry of the ^{3}He target and the study of the target polarization are presented in Chapter 3.

The direct measurement of the target polarization using a neutron source at RIKEN is described in Chapter 4. Chapter 5 deals with the measurement of ^{3}He analyzing power at CYRIC and RCNP. The experimental results are compared with the theoretical predictions in Chapter 6. Summary and conclusion follow in Chapter 7.

Chapter 2

Polarized ^{3}He Target

We developed the polarized ^{3}He target for the measurement of ^{3}He analyzing powers. In this chapter, we describe the principles of a polarization method of ^{3}He nuclei, a construction of a target glass cell which contains ^{3}He gas, and the devices of our polarization system.

2.1 Principle of ^{3}He Polarization

A polarized ^{3}He target is used in a wide variety of scientific researches. The net magnetic moment of a ^{3}He nucleus approximately equals to the magnetic moment of the neutron in it since the two protons in a ^{3}He nucleus are in a spin singlet state by the Pauli exclusion principle. As a matter of fact it has been indicated that about 90 % of the nuclear spin of ^{3}He is dominated by the neutron spin [72], and hence a polarized ^{3}He target is a reasonable approximation to a polarized neutron target. Furthermore, ^{3}He nuclei have a large absorption cross section depending on the spin direction to a low energy neutron [73]. Therefore polarized ^{3}He nuclei are also utilized as a neutron spin filter [74] and polarimetry [75]. In this section, we describe the principles of ^{3}He polarization.

2.1.1 Polarization Methods of ^{3}He Nuclei

There are two major techniques for a production of polarized ^{3}He nuclei; metastability-exchange optical pumping (MEOP) [76] and spin-exchange optical pumping (SEOP) [77]. In the MEOP method, ^{3}He nuclear polarizations are produced by metastability exchange with optically pumped metastable ^{3}He atoms. Figure 2.1 shows the energy levels of ^{3}He atoms and the scheme of MEOP. An radio-frequency (RF) discharge is used to produce

the 2^3S_1 metastable state of ^{3}He atoms. The metastable ^{3}He atoms are optically pumped by circularly polarized light tuned at 1083 nm corresponding to the transition between the 2^3S_1 and 2^3P states. Then the metastability exchange collision occurs between ground state ^{3}He atoms and polarized metastable ^{3}He atoms. As a result, the ^{3}He nuclei in the ground state are polarized by this process. The MEOP method typically achieves a high ^{3}He polarization about 80% since the cross section for metastability exchange is quite large ($\sigma \sim 10^{-16}$ cm^2). However, to maintain the RF discharge, ^{3}He gas pressure is limited to the order of 1 mbar. Therefore this method is not appropriate for the target of the scattering experiment which requires high ^{3}He number density.

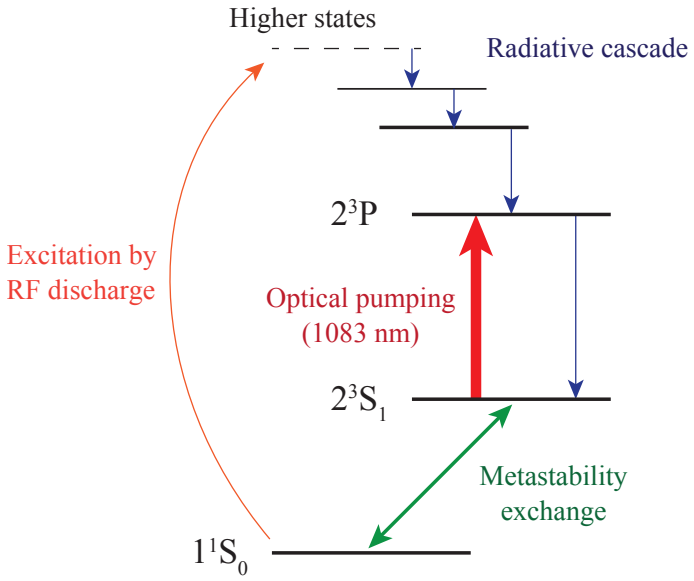

Figure 2.1: Schematic view of MEOP.

In order to obtain high density polarized ^{3}He gas, the SEOP method is appropriate. This method has two steps. First, alkali metal atoms are polarized by optical pumping with circularly polarized light in the presence of a static magnetic field. Then, the alkali metal polarization is transferred to ^{3}He nuclei by hyper-fine interactions. A high power laser with an output power on the order of 10 W is generally used for optical pumping of alkali metal atoms. Recently, the SEOP method achieves a high ^{3}He polarization of more than 70 % with ^{3}He gas pressure of $\sim$ 3 atm [78]. For the above reasons, we have adopted the SEOP method to produce polarized ^{3}He nuclei. We describe the details of SEOP in the following sub-sections 2.1.2–2.1.4.

2.1.2 Optical Pumping of Rubidium Atoms

In order to produce high density polarized ^{3}He gas, it is necessary to polarize large volumes of alkali metal vapor by a high power laser. Rb atoms are typically employed for optical pumping because of the availability of high power lasers at the Rb D_1 line ($\lambda = 795$ nm). Optical pumping of alkali metal atoms relies on the angular momentum selection rule in the optical excitation. Figure 2.2 shows simplified energy levels of Rb atoms without the effect of nuclear spin. In the presence of a static magnetic field, the $5^2S_{1/2}$ ground state and the $5^2P_{1/2}$ excited state of Rb split into the Zeeman sub-levels of $m_J = \pm 1/2$. Rb atoms are excited from the $5^2S_{1/2}$ state to the $5^2P_{1/2}$ state by a laser tuned to 795 nm corresponding to the D_1 transition. When right circularly polarized light (σ_+) is used, the Rb atoms can only be excited from the $m_J = -1/2$ state. Then the excited Rb atoms decay to the both levels of the $5^2S_{1/2}$ ground state. Note that the direction of the light propagation is parallel to the direction of the static magnetic field which fixes the quantization axis. The probabilities of this de-excitation are 2/3 for $5^2P_{1/2}$ ($m_J = +1/2$) to $5^2S_{1/2}$ ($m_J = -1/2$) and 1/3 for $5^2P_{1/2}$ ($m_J = +1/2$) to $5^2S_{1/2}$ ($m_J = +1/2$), respectively. Generally in SEOP, ^{3}He gas at a pressure of a few atm is filled in a cell with alkali metals. The excited Rb atoms decay to the both levels of the $5^2S_{1/2}$ state with equal probabilities since the populations of the sub-levels of the $5^2P_{1/2}$ state equalize by collisions with ^{3}He atoms (*collisional mixing*). Therefore, the Rb atoms will be accumulated in the $5^2S_{1/2}$ ($m_J = +1/2$) state. The photons emitted from the de-excitation of Rb atoms cause a saturation of optical pumping processes. The transition from $5^2P_{1/2}$ ($m_J = +1/2$) to $5^2S_{1/2}$ ($m_J = -1/2$) emits right circularly polarized light (σ_+), the transition from $5^2P_{1/2}$ ($m_J = -1/2$) to $5^2S_{1/2}$ ($m_J = +1/2$) emits left circularly polarized light (σ_-) and the transition between the same sub-levels emits linearly polarized light (π), respectively. However, the efficiency of optical pumping processes is limited since the Rb atoms accumulated in the $5^2S_{1/2}$ ($m_J = +1/2$) state can be excited by absorptions of the σ_- or π photons (*radiation trapping*). In order to suppress this effect, N_2 gas is added to the cell as a buffer gas. Figure 2.3 shows the optical pumping processes in the presence of ^{3}He gas with and without a buffer gas. The excited Rb atoms can radiationlessly decay to the ground state since the energy of them can be transferred to the vibrational and rotational motion of the N_2 molecule. The probability of a radiative decay of the excited Rb atoms is given by [79],

$$B_\gamma = \frac{3}{3 + P_{N_2}}, \tag{2.1}$$

where P_{N_2} is the partial pressure of N_2 gas in torr. We typically use about 100 Torr of N_2 gas, then B_γ is suppressed to $\sim 3\%$.

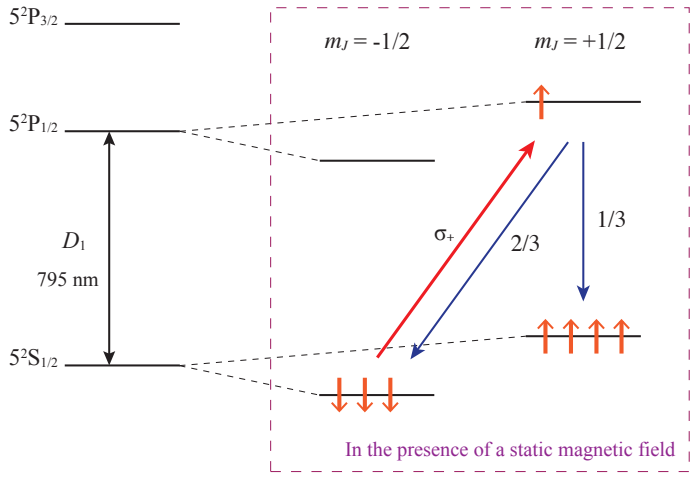

Figure 2.2: Optical pumping of Rb atoms by circularly polarized light. The perturbation due to nuclear spins is ignored.

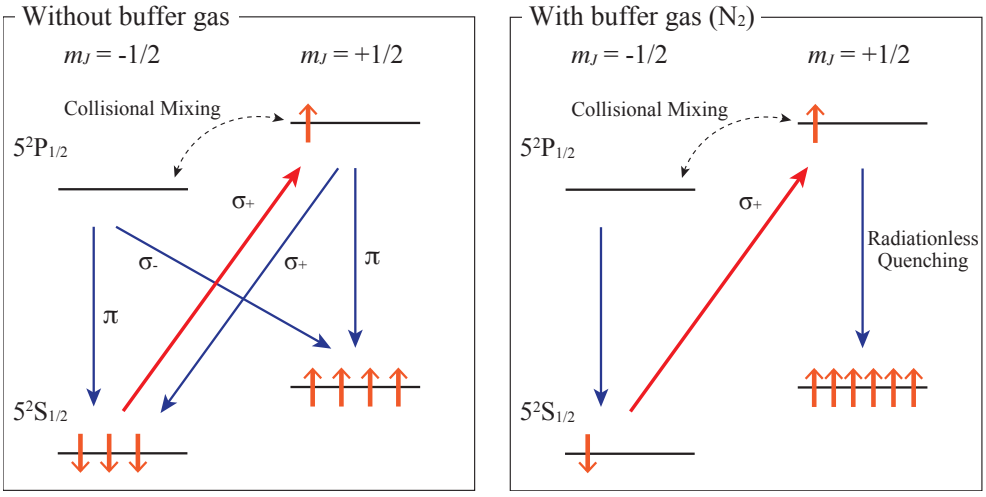

Figure 2.3: Optical pumping of Rb atoms by circularly polarized light with (right panel) and without (left panel) a N_2 buffer gas. The perturbation due to nuclear spins is ignored.

Next, we derive the expression of the atomic polarization of Rb. The Rb polarization P_{Rb} is

$$P_{\mathrm{Rb}} = \frac{\rho_+ - \rho_-}{\rho_+ + \rho_-} = \rho_+ - \rho_-, \tag{2.2}$$

where $\rho_\pm$ is the probability that a Rb atom is in the $m_J = \pm 1/2$ state ($\rho_+ + \rho_- = 1$). The

rate equation of $\rho_\pm$ is given by [80],

$$\frac{d\rho_\pm(x)}{dt} = \pm\left(\gamma_\nu^+(x) + \gamma_\nu^0(x) + \Gamma_{\rm Rb} - D\frac{d^2}{dx^2}\right)\rho_-(x) \mp \left(\frac{\Gamma_{\rm Rb}}{2} + \frac{\gamma_\nu^0(x)}{2}\right), \tag{2.3}$$

where $\gamma_\nu^+(x)$ ($\gamma_\nu^0(x)$) denotes the absorption rate of circularly (linearly) polarized photons per Rb atom at the position x along the propagation direction, and $\Gamma_{\rm Rb}$ is the spin destruction rate of Rb atoms. D is the effective diffusion constant for Rb atoms in the presence of ^{3}He gas and reflects the boundary conditions of the Rb polarization near the cell wall and the nonuniformity of Rb densities. We assume that the polarization of the laser light used for optical pumping is nearly perfect circular; hence $\gamma_\nu^0(x) = 0$. Furthermore, we also assume that $\rho_\pm(x)$ is uniform in the cell because of the high gas pressure and density. Thus the diffusion term of Eq. (2.3) is negligible, Eq. (2.3) is simplified to

$$\begin{aligned}\frac{d\rho_\pm(x)}{dt} &= \pm\left(\gamma_\nu^+(x) + \Gamma_{\rm Rb}\right)\rho_-(x) \mp \frac{\Gamma_{\rm Rb}}{2} \\ &= \pm\left(\gamma_\nu^+(x) + \frac{\Gamma_{\rm Rb}}{2}\right)\rho_-(x) \mp \frac{\Gamma_{\rm Rb}}{2}\rho_+(x).\end{aligned} \tag{2.4}$$

From Eq. (2.2) and (2.4), the rate equation of the Rb polarization is given by,

$$\begin{aligned}\frac{dP_{\rm Rb}(x)}{dt} &= \frac{d}{dt}(\rho_+(x) - \rho_-(x)) \\ &= -\left(\gamma_\nu^+(x) + \Gamma_{\rm Rb}\right)P_{\rm Rb}(x) + \gamma_\nu^+(x).\end{aligned} \tag{2.5}$$

Therefore, the solution to Eq. (2.5) is

$$P_{\rm Rb}(x,t) = \left(\frac{\gamma_\nu^+(x)}{\gamma_\nu^+(x) + \Gamma_{\rm Rb}}\right)\left[1 - e^{-(\gamma_\nu^+(x) + \Gamma_{\rm Rb})t}\right]. \tag{2.6}$$

The equilibrium Rb polarization ($t \to \infty$) can be expressed as,

$$\overline{P}_{\rm Rb}(x) = \frac{\gamma_\nu^+(x)}{\gamma_\nu^+(x) + \Gamma_{\rm Rb}}. \tag{2.7}$$

Thus, the Rb polarization is determined by the ratio of $\gamma_\nu^+(x)$ and $\Gamma_{\rm Rb}$.

The optical pumping rate $\gamma_\nu^+(x)$ is given by,

$$\gamma_\nu^+(x) = \int \Phi(x,\nu)\sigma_{\rm abs}(\nu)d\nu, \tag{2.8}$$

where $\Phi(x,\nu)$ is the flux of circularly polarized photons per unit area and frequency at the position x and $\sigma_{\rm abs}(\nu)$ is the light absorption cross section. The propagation of the laser

light through the cell is defined as follows:

$$\Phi(0,\nu) = \frac{I_{\rm laser}(\nu)}{h\nu}, \tag{2.9}$$

$$\frac{d\Phi(x,\nu)}{dx} = -[\mathrm{Rb}]\sigma_{\rm abs}(\nu)(1-P_{\rm Rb}(x))\Phi(x,\nu), \tag{2.10}$$

where $I_{\rm laser}(\nu)$ is the intensity of circularly polarized light per unit area and frequency, h is the Planck constant, and [Rb] denotes the Rb number density. The light absorption cross section $\sigma_{\rm abs}(\nu)$ is given by [80],

$$\sigma_{\rm abs}(\nu) = \frac{\lambda_0^2}{8\pi}\Gamma_{\rm nat}\left[\frac{\Gamma}{(\nu-\nu_0)^2+(\Gamma/2)^2} + \frac{b(\nu-\nu_0)}{\Gamma}e^{-\frac{|\nu-\nu_0|}{\Gamma_a}}\right], \tag{2.11}$$

where λ_0 (794.979 nm) and ν_0 (377.107 THz) are the wavelength and frequency of the Rb D_1 transition in vacuum, respectively. $\Gamma_{\rm nat}$ (5.75 MHz) is the natural line width, Γ is the total pressure broadened width, and b and Γ_a are the convenient parameters to describe the observed line shape asymmetry. These parameters have been obtained by Larson *et al.* [80] and are summarized in Table 2.1.

Table 2.1: The parameters of the light absorption cross section for the Rb D_1 line [80].

^{3}He pressure [atm]	Γ [GHz]	Γ_a [GHz]	b [10^{-12} s]
2.94	54 ± 3	154 ± 11	0.20 ± 0.04
6.44	126 ± 5	146 ± 11	1.0 ± 0.2
8.97	184 ± 6	184 ± 11	1.5 ± 0.2
12.1	244 ± 7	225 ± 12	1.5 ± 0.2

The electron spin destruction of Rb atoms is mostly due to the spin rotation interaction during collisions between the Rb and other atoms. The spin rotation interaction is described by [81],

$$\mathcal{H}_{\rm SR} = \gamma \boldsymbol{N}\cdot\boldsymbol{S}, \tag{2.12}$$

where γ is the coupling coefficient, $\boldsymbol{N}$ is the rotational angular momentum of the coupling pair, and $\boldsymbol{S}$ is the electron spin of the Rb atom. The spin destruction rate due to the collisions with atoms is proportional to the density of those atoms, hence $\Gamma_{\rm Rb}$ is given by,

$$\Gamma_{\rm Rb} = \langle\sigma_{\rm SD}v\rangle[\mathrm{Rb}] + \langle\sigma_{\rm N_2}v\rangle[\mathrm{N_2}] + \langle\sigma_{\rm SE}v\rangle[^3\mathrm{He}] + k_3[^3\mathrm{He}]^2, \tag{2.13}$$

where the box bracket denotes the number density of atoms or molecules. $\langle\sigma_{\rm SD}v\rangle$, $\langle\sigma_{\rm N_2}v\rangle$, and $\langle\sigma_{\rm SE}v\rangle$ are the velocity averaged cross sections of the Rb–Rb, Rb–N_2, and Rb–^{3}He

collisions, respectively. The last term of Eq. (2.13) expresses the effect of three-body collisions between a Rb atom and two ^{3}He atoms. These constants have been measured by Wagshul and Chupp [82] and Larson *et al.* [80]:

$$\langle \sigma_{\mathrm{SD}} v \rangle = (8.3 \pm 0.6) \times 10^{-13} \ [\mathrm{cm}^3/\mathrm{s}], \tag{2.14}$$

$$\langle \sigma_{\mathrm{N_2}} v \rangle = (9.38 \pm 0.22) \times 10^{-18} \ [\mathrm{cm}^3/\mathrm{s}], \tag{2.15}$$

$$\langle \sigma_{\mathrm{SE}} v \rangle = (6.1 \pm 0.2) \times 10^{-20} \ [\mathrm{cm}^3/\mathrm{s}], \tag{2.16}$$

$$k_3 \sim 7.5 \times 10^{-39} \ [\mathrm{cm}^6/\mathrm{s}]. \tag{2.17}$$

Here, we estimate Γ_{Rb} in our operating conditions (the pressure of ^{3}He gas is $\sim$ 3 atm, the pressure of N_2 gas is $\sim$ 100 Torr, and the cell temperature is 200 °C). The density of ^{3}He at 273 K and 1 atm is 1.35×10^{-4} g/cm^3 and that of N_2 is 1.25×10^{-3} g/cm^3. The molar mass of ^{3}He atoms is 3.016 g/mol and that of N_2 molecules is 28.01 g/mol. Thus, the number density at 300 K is 7.4×10^{19} cm^{-3} for ^{3}He atoms and 3.2×10^{18} cm^{-3} for N_2 molecules. The number density of Rb can be written as a function of temperature [83]:

$$[\mathrm{Rb}] = \frac{7.243}{T} 10^{25.318 - \frac{4040}{T}} \ [\mathrm{cm}^{-3}], \tag{2.18}$$

where T is the temperature in Kelvin. Using Eq. (2.18), the number density of Rb is 9.2×10^{14} cm^{-3} at 200 °C. Therefore, the spin destruction rate Γ_{Rb} is calculated by,

$$\Gamma_{\mathrm{Rb}} = \langle \sigma_{\mathrm{SD}} v \rangle [\mathrm{Rb}] + \langle \sigma_{\mathrm{N_2}} v \rangle [\mathrm{N_2}] + \langle \sigma_{\mathrm{SE}} v \rangle [^3\mathrm{He}] + k_3 [^3\mathrm{He}]^2 \tag{2.19}$$

$$= 765 + 30 + 4.5 + 41 \ [\mathrm{s}^{-1}] \tag{2.20}$$

$$= 840 \ [\mathrm{s}^{-1}]. \tag{2.21}$$

Therefore, the Rb–Rb collisions dominate the relaxation process of the Rb electron spin in this condition.

2.1.3 Spin Exchange between Alkali Metal and ^{3}He

In the mixture of Rb vapor and ^{3}He gas, the polarization of Rb atoms is transferred to ^{3}He nuclei through the spin exchange process. The spin exchange occurs by hyperfine interactions between the valence electron of Rb atoms and the ^{3}He nucleus. This interaction is given by [84],

$$\mathcal{H}_{\mathrm{HFI}} = -2\gamma_{^3\mathrm{He}} \mu_{\mathrm{N}} \mu_{\mathrm{B}} \sum_{i=1}^{3} \left[\frac{\boldsymbol{I} \cdot \boldsymbol{J}_i}{r_i^3} - 3 \frac{(\boldsymbol{I} \cdot \boldsymbol{r}_i)(\boldsymbol{J}_i \cdot \boldsymbol{r}_i)}{r_i^5} - \frac{8\pi}{3} \delta(\boldsymbol{r}_i) \boldsymbol{I} \cdot \boldsymbol{J}_i \right], \tag{2.22}$$

where $\gamma_{^3\mathrm{He}}$ is the gyro magnetic ratio of ^{3}He, μ_N is the nuclear magneton, and μ_B is the Bohr magneton. The Rb valence electron corresponds to $i = 1$ and the ^{3}He electrons correspond to $i = 2, 3$. $\boldsymbol{I}$ is the ^{3}He nuclear spin, $\boldsymbol{J}_i$ is the i-th electron spin, and $\boldsymbol{r}_i$ is the position vector from the ^{3}He nucleus to the i-th electron. The first two terms in Eq. (2.22) represent the polar interaction between two magnetic dipoles. The third term is the Fermi contact potential which gives rise to a polarization transfer from Rb atoms to ^{3}He nuclei. This interaction also causes a shift of the Rb Zeeman frequency due to the ^{3}He polarization. We used the Zeeman frequency shift for ^{3}He polarimetry, as described in Chapter 3.

We describe the equation of the nuclear polarization of ^{3}He below. The ground state of ^{3}He nuclei splits into the Zeeman sub-levels of $m_I = \pm 1/2$ in the presence of a static magnetic field. The ^{3}He polarization is defined by,

$$P_{^3\mathrm{He}} = \frac{\tilde{\rho}_+ - \tilde{\rho}_-}{\tilde{\rho}_+ + \tilde{\rho}_-} = \tilde{\rho}_+ - \tilde{\rho}_-, \tag{2.23}$$

where $\tilde{\rho}_\pm$ is the populations of the $m_I = \pm 1/2$ sub-levels and we have used the relation $\tilde{\rho}_+ + \tilde{\rho}_- = 1$. The rate equation of $\tilde{\rho}_\pm$ is given by [80],

$$\frac{d\tilde{\rho}_\pm}{dt} = \pm \left(\frac{\Gamma_{^3\mathrm{He}}}{2} + \gamma_\mathrm{SE}\rho_+ \right) \tilde{\rho}_- \mp \left(\frac{\Gamma_{^3\mathrm{He}}}{2} + \gamma_\mathrm{SE}\rho_- \right) \tilde{\rho}_+, \tag{2.24}$$

where $\gamma_\mathrm{SE} = k_\mathrm{SE}[\mathrm{Rb}]$ is the spin exchange rate between a Rb atom and a ^{3}He nucleus and $\Gamma_{^3\mathrm{He}}$ is the spin relaxation rate of ^{3}He nuclei. $k_\mathrm{SE} = \langle \sigma_\mathrm{SE} v \rangle$ is the spin exchange rate constant and have been measured to be $(6.1 \pm 0.2) \times 10^{-20}$ cm^3/s by Larson *et al.* [80] and $(6.8 \pm 0.2) \times 10^{-20}$ cm^3/s by Chann *et al.* [85]. Based on Eqs. (2.23) and (2.24), the rate equation of the ^{3}He polarization is given by,

$$\frac{dP_{^3\mathrm{He}}}{dt} = -(\gamma_\mathrm{SE} + \Gamma_{^3\mathrm{He}})P_{^3\mathrm{He}} + \gamma_\mathrm{SE}\overline{P}_\mathrm{Rb}, \tag{2.25}$$

where we ignore the time dependence of $\overline{P}_\mathrm{Rb}$ because the polarizing rate of Rb atoms is much faster than that of ^{3}He nuclei ($\gamma_\nu^+ + \Gamma_\mathrm{Rb} \gg \gamma_\mathrm{SE} + \Gamma_{^3\mathrm{He}}$). Therefore, the solution to Eq. (2.25) is

$$P_{^3\mathrm{He}} = \overline{P}_\mathrm{Rb} \frac{\gamma_\mathrm{SE}}{\gamma_\mathrm{SE} + \Gamma_{^3\mathrm{He}}} \left[1 - e^{-(\gamma_\mathrm{SE} + \Gamma_{^3\mathrm{He}})t} \right]. \tag{2.26}$$

The equilibrium ^{3}He polarization ($t \to \infty$) is expressed as,

$$\overline{P}_{^3\mathrm{He}} = \overline{P}_\mathrm{Rb} \frac{\gamma_\mathrm{SE}}{\gamma_\mathrm{SE} + \Gamma_{^3\mathrm{He}}} \tag{2.27}$$

$$= \frac{\gamma_\nu^+(x)}{\gamma_\nu^+(x) + \Gamma_\mathrm{Rb}} \frac{\gamma_\mathrm{SE}}{\gamma_\mathrm{SE} + \Gamma_{^3\mathrm{He}}}, \tag{2.28}$$

where we use Eq. (2.7). In order to achieve a high ^{3}He polarization, one needs $\gamma_{\rm SE} \gg \Gamma_{^3{\rm He}}$ and $\gamma_\nu^+ \gg \Gamma_{\rm Rb}$. It is important to optimize the operating temperature since $\gamma_{\rm SE}$ and $\Gamma_{\rm Rb}$ are proportional to the Rb number density that depends strongly on the temperature. We also need to construct cells with few impurities so that $\Gamma_{^3{\rm He}}$ is minimized. Furthermore, we need to use a high power laser to obtain a high Rb polarization at high temperatures.

The spin relaxation rate of ^{3}He nuclei is mainly due to the three relaxation processes:

1. ^{3}He–^{3}He dipole interactions ($\Gamma_{\rm D}$),
2. inhomogeneity of the static magnetic field ($\Gamma_{\rm B}$), and
3. interactions with impurities in the cell wall or in gas ($\Gamma_{\rm W}$).

Thus, the spin relaxation rate of ^{3}He nuclei is the sum of these relaxation rates:

$$\Gamma_{^3{\rm He}} = \Gamma_{\rm D} + \Gamma_{\rm B} + \Gamma_{\rm W}. \tag{2.29}$$

The ^{3}He spin relaxation rate due to ^{3}He–^{3}He dipole interactions is calculated by Newbury *et al.* [86]:

$$\Gamma_{\rm D} = \frac{[^3{\rm He}]}{744}\ [{\rm h}^{-1}], \tag{2.30}$$

where $[^3{\rm He}]$ is in amagat defined as the number of ideal gas molecules per unit volume at 1 atm and 273.15 K. In typical conditions, $[^3{\rm He}] \sim 3$ amg, the ^{3}He spin relaxation rate due to ^{3}He–^{3}He dipole interactions is $\Gamma_{\rm D} = 4 \times 10^{-3}$ h^{-1}.

Inhomogeneities of a static magnetic field also cause spin relaxation of ^{3}He nuclei and its relaxation rate is given by [87],

$$\Gamma_{\rm B} = D_{^3{\rm He}} \frac{|\nabla B_x|^2 + |\nabla B_y|^2}{B_z^2}, \tag{2.31}$$

where $D_{^3{\rm He}}$ is the diffusion constant for the polarized spin. $D_{^3{\rm He}}$ is written as follows [88]:

$$D_{^3{\rm He}} = \frac{1}{2.13} \frac{\lambda v}{(1+\omega^2\tau^2)}, \tag{2.32}$$

where λ and v are the mean free path and the root mean square velocity of ^{3}He atoms, respectively. ω is the Larmor frequency of the ^{3}He nuclear spin and $\tau = \lambda/v$ is the collision time of ^{3}He gas. In our typical conditions ($[^3{\rm He}] \sim 3$ amg), the diffusion constant is small $D_{^3{\rm He}} \sim 0.3$ cm^2/s. Typical magnetic gradients ∇B_x and ∇B_y are 3 μT/cm in our

condition. Thus, the ^{3}He spin relaxation due to magnetic field gradients is negligible small $\sim 10^{-2}$ h^{-1}.

The main sources of the ^{3}He spin relaxation due to impurities are ferromagnetic elements in the composition of the glass cell or contaminants on the cell wall. To reduce the relaxation due to the former source, we have adopted glass which contains low ferromagnetic elements. In order to remove contaminants from the glass cell, we perform the cleaning and bake out procedures of the glass cell, as discussed later. In addition, we use gas purifiers to clean gases filled into the cell. The typical ^{3}He spin relaxation rate of our cells is $\Gamma_{^3\mathrm{He}} \sim 5 \times 10^{-2}$ h^{-1}, thus this implies that the ^{3}He spin relaxation due to impurities is dominant.

2.1.4 Alkali-Hybrid SEOP

In the SEOP method, Rb atoms are typically used for optical pumping because of the availability of high power lasers. The alkali-hybrid spin exchange optical pumping (AH-SEOP) method [89] takes advantage of higher spin-transfer efficiency and remains the availability of optical pumping for Rb atoms. A mixture of Rb and K is typically employed in this method. The Rb polarization optically pumped by circularly polarized light can be transferred to the K atoms with little loss. The K–Rb spin exchange rate ($\sim 10^5$–10^6 s^{-1}) is much larger than the spin relaxation rate of alkali metal atoms at typical number densities of 10^{14} cm^{-3} or more since the K–Rb spin exchange cross section is on the order of 10^{-14} cm^2 [90]. Therefore, the K and Rb atoms attain equal equilibrium polarizations immediately.

In the AH-SEOP method, the ^{3}He polarization is produced by collisions with both of K and Rb atoms. Thus, the rate equation of the ^{3}He polarization is analogy to Eq. (2.25) and given by,

$$\frac{dP_{^3\mathrm{He}}}{dt} = -(\gamma_{\mathrm{SE}}^{\mathrm{A}} + \Gamma_{^3\mathrm{He}})P_{^3\mathrm{He}} + \gamma_{\mathrm{SE}}^{\mathrm{A}}\overline{P}_{\mathrm{A}}, \tag{2.33}$$

where $\gamma_{\mathrm{SE}}^{\mathrm{A}} = k_{\mathrm{SE}}^{\mathrm{K}}[\mathrm{K}] + k_{\mathrm{SE}}^{\mathrm{Rb}}[\mathrm{Rb}]$ is the total hybrid spin exchange rate and $\overline{P}_{\mathrm{A}}$ is the equilibrium polarization of alkali metal atoms. $k_{\mathrm{SE}}^{\mathrm{K}}$ and $k_{\mathrm{SE}}^{\mathrm{Rb}}$ are the spin exchange rate constant for K–^{3}He and Rb–^{3}He collisions, respectively. $k_{\mathrm{SE}}^{\mathrm{K}}$ have been measured to be $(6.1 \pm 0.4) \times 10^{-20}$ cm^3/s by Babcock *et al.* [89] and $(7.5 \pm 0.6) \times 10^{-20}$ cm^3/s by Singh *et al.* [91]. From Eq. (2.33), the solution to this equation is written by,

$$P_{^3\mathrm{He}} = \overline{P}_{\mathrm{A}} \frac{\gamma_{\mathrm{SE}}^{\mathrm{A}}}{\gamma_{\mathrm{SE}}^{\mathrm{A}} + \Gamma_{^3\mathrm{He}}} \left[1 - e^{-(\gamma_{\mathrm{SE}}^{\mathrm{A}} + \Gamma_{^3\mathrm{He}})t}\right]. \tag{2.34}$$

Therefore, the equilibrium ^{3}He polarization ($t \to \infty$) is expressed as,

$$\overline{P}_{^3\mathrm{He}} = \overline{P}_{\mathrm{A}} \frac{\gamma_{\mathrm{SE}}^{\mathrm{A}}}{\gamma_{\mathrm{SE}}^{\mathrm{A}} + \Gamma_{^3\mathrm{He}}}. \tag{2.35}$$

For optical pumping of Rb atoms, the spin relaxation rate increases due to additional collisions with K atoms. Thereby, the effective spin relaxation rate of Rb atoms is given by [89],

$$\Gamma'_{\mathrm{Rb}} = \Gamma_{\mathrm{Rb}} + D\Gamma_{\mathrm{K}} + q_{\mathrm{KR}}[\mathrm{K}], \tag{2.36}$$

where $D = [\mathrm{K}]/[\mathrm{Rb}]$ is the ratio of the alkali metal number densities and Γ_{K} is the spin destruction rate of pure K atoms. q_{KR} is the spin destruction rate constant for Rb–K collisions, and is described as the geometric mean between Rb–Rb and K–K spin destruction rate constants [92]. The number density of K can be written as a function of temperature similarly to that of Rb [83]:

$$[\mathrm{K}] = \frac{7.243}{T} 10^{25.408 - \frac{4453}{T}} \ [\mathrm{cm}^{-3}]. \tag{2.37}$$

We assume that the alkali metal densities approximately obey Raoult's law [93]:

$$[\mathrm{Rb}] = m_{\mathrm{Rb}}[\mathrm{Rb}]_0, \tag{2.38}$$

$$[\mathrm{K}] = m_{\mathrm{K}}[\mathrm{K}]_0, \tag{2.39}$$

because a mixture of Rb and K is used for the AH-SEOP method. Here the subscript 0 denotes the saturated vapor density of pure alkali metal atoms. m_{Rb} and m_{K} are the mole fraction of Rb and K, respectively. Thus, the ratio of the alkali metal number densities is written as,

$$D = \frac{m_{\mathrm{K}}[\mathrm{K}]_0}{m_{\mathrm{Rb}}[\mathrm{Rb}]_0} = \frac{1 - m_{\mathrm{Rb}}}{m_{\mathrm{Rb}}} \frac{[\mathrm{K}]_0}{[\mathrm{Rb}]_0}, \tag{2.40}$$

where we have used the relation $m_{\mathrm{Rb}} + m_{\mathrm{K}} = 1$.

Γ_{K} arises from K–K, K–^{3}He, and K–N_2 collisions. Thus, the expression of Γ_{K} is given by,

$$\Gamma_{\mathrm{K}} = \Gamma_{\mathrm{K-K}} + \Gamma_{\mathrm{K-}^3\mathrm{He}} + \Gamma_{\mathrm{K-N_2}}. \tag{2.41}$$

These contributions to the spin destruction rate of K atoms can be written as follows [92]:

$$\Gamma_{\mathrm{K-K}} = 9.6 \times 10^{-14}[\mathrm{K}] \ [\mathrm{s}^{-1}], \tag{2.42}$$

$$\Gamma_{\mathrm{K-}^3\mathrm{He}} = (k_{\mathrm{SE}}^{\mathrm{K}} + 5.8 \times 10^{-31} T^{4.259})[^3\mathrm{He}] \ [\mathrm{s}^{-1}], \tag{2.43}$$

$$\Gamma_{\mathrm{K-N_2}} = 7.0 \times 10^{-26} T^3 [\mathrm{N_2}] \ [\mathrm{s}^{-1}]. \tag{2.44}$$

The spin exchange efficiency in AH-SEOP is defined as follows [89]:

$$\eta_{\rm SE} = \frac{\gamma_{\rm SE}^{\rm A}[^3{\rm He}]}{[{\rm Rb}]\Gamma'_{\rm Rb}} = \frac{(k_{\rm SE}^{\rm Rb} + Dk_{\rm SE}^{\rm K})[^3{\rm He}]}{\Gamma_{\rm Rb} + D\Gamma_{\rm K} + q_{\rm KR}[{\rm K}]}. \tag{2.45}$$

$\eta_{\rm SE}$ means the ratio of the rate at which spin polarization is transferred to ^{3}He nuclei to the rate at which it is lost by spin relaxation of alkali metal atoms. Figure 2.4 shows the spin exchange efficiency as a function of D in our typical conditions. The spin exchange efficiency increases with D as shown in Fig. 2.4. However, the several experiments have reported that the maximum polarization of alkali metal atoms decreases in high D [89,94]. It has been indicated that this effect arises from off resonant pumping of K atoms by 795 nm light that is used for optical pumping of Rb atoms. Therefore, it is important to optimize the vapor ratio D at operating temperatures. Chen *et al.* [92] have found that D between 2 and 6 yields the best results such as the maximum ^{3}He polarization and pumping rate.

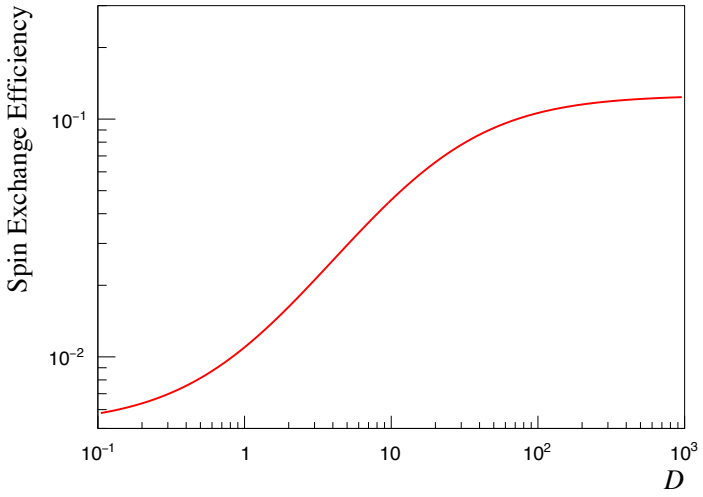

Figure 2.4: The spin exchange efficiency as a function of the ratio of the alkali metal number densities at a temperature of 200 C°.

Here, we estimate the volume ratio of solid Rb and K to satisfy the desired vapor ratio at operating temperatures. This volume ratio is the criteria of the volume of alkali metals introduced into the glass cell. Note that we assume the best vapor ratio is $D = 4$ which is a middle value of the desired range. The molar mass of Rb is 85.47 g/mol and that of K is 39.10 g/mol. The density of Rb is 1.53 g/cm^3 and that of K is 0.862 g/cm^3. Thus, the

volume ratio of alkali metals is calculated by,

$$\frac{V_{\mathrm{K}}}{V_{\mathrm{Rb}}} = D\frac{[\mathrm{Rb}]_0}{[\mathrm{K}]_0} \cdot \frac{39.10 \cdot 1.53}{85.47 \cdot 0.862} \simeq 17.5, \tag{2.46}$$

where V_{K} and V_{Rb} are the volume of solid K and Rb, respectively. We have used a operating temperature of 230 C° in the AH-SEOP method.

2.2 Cell Construction

We have developed glass cells filled with ^{3}He gas as the targets of the scattering experiments. In this section, we discuss the dimensions and structures of our target glass cells, and the procedure for gas filling in detail. The measurement of the vapor density ratios for alkali hybrid cells is also discussed.

2.2.1 Cell Dimensions

We used GE180 glass which is boron-free aluminosilicate glass produced by General Electric Co. for the target cells. GE180 is a type of glass which has few paramagnetic impurities and is less permeable to ^{3}He atoms than other glass (*e.g.*, Pyrex glass and quartz glass) [95,96]. Therefore, the glass containers made of GE180 have low spin relaxation rates of ^{3}He nuclei and can retain high pressure ^{3}He gas for a long time.

The dimensions of our target cells are shown in Fig. 2.5. The cell named Koganei was used in December, 2016 and June, 2017 for the experiments at CYRIC, Tohoku University. The cell named Ishibashi was used in June, 2018 for the experiment at CYRIC and in November, 2018 for the experiment at RCNP, Osaka University. Koganei cell is a conventional SEOP cell, which contains Rb. Ishibashi cell is a AH-SEOP cell (contains a mixture of K and Rb). These cells consist of two chambers, the target chamber and the pumping chamber, which connected by a transfer tube. In order to get a sufficient amount of the Rb vapor for SEOP, the pumping chamber is heated to nearly 200 °C. ^{3}He nuclei are polarized in the pumping chamber through spin exchange interactions and diffuse into the target chamber.

The glass thickness of the target chamber should be thin so that the energy loss of both incoming and scattered charged particles in the glass is minimized. However, the glass cell is also needed to withstand high gas pressure. Accordingly, we designed concave windows for the target chamber of the Koganei cell and convex windows for that of the

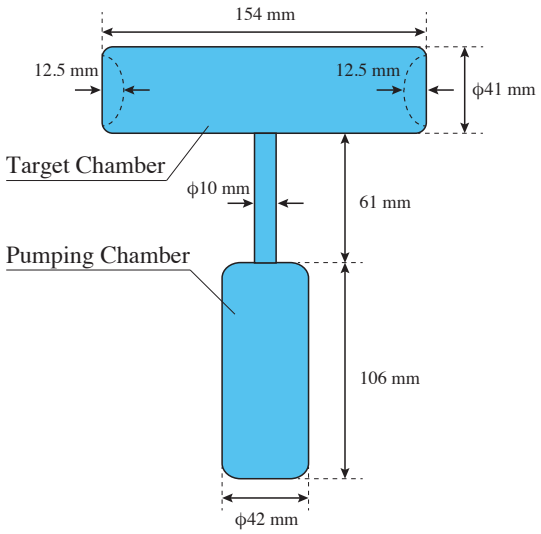

(a) Koganei cell

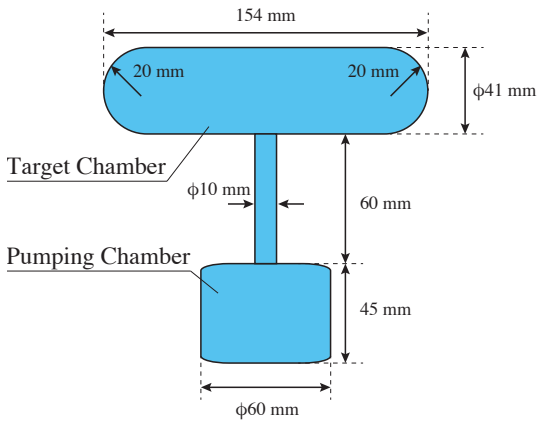

(b) Ishibashi cell

Figure 2.5: Dimensions of the target glass cell Koganei (a) and Ishibashi (b).

Ishibashi cell. The thicknesses of the cell windows were typically 0.4 mm and that of the side surfaces of the target chamber and the pumping chamber were 1.0–2.0 mm. The glass thicknesses were measured with a ultrasonic thickness gauge (PVX, Dakota Japan Inc.) which has a resolution of 0.001 mm.

2.2.2 Gas Filling System

We have constructed a vacuum system that is capable of handling clean gases to minimize the ^{3}He spin relaxation. In this section, we describe our gas filling system.

Figure 2.6 shows a schematic view of our gas filling system. This system consists of a vacuum system, pressure gauges, ^{3}He and N_2 gas cylinders and getter gas purifiers.

For filling ^{3}He gas as well as N_2 gas and alkali metals, a target cell was initially connected to a glass tube (cell branch). A schematic views of cell branches are shown in Fig. 2.7 (for a SEOP cell) and Fig. 2.8 (for a AH-SEOP cell). Cell branches were fabricated in a glass shop of School of Science, Tohoku University. This branch was connected to the gas filling system via a Kovar to Pyrex seal. The cell branches were made of Pyrex glass which is widely used for laboratory glassware and can be manufacture with comparative ease. The target cell and the branch part were connected with a tube with a diameter of 8 mm. The "T-tube" of the cell branch had a opening for insertion of a alkali metal ampule. Note that the opening was initially closed to perform a pressure test and baking the whole cell

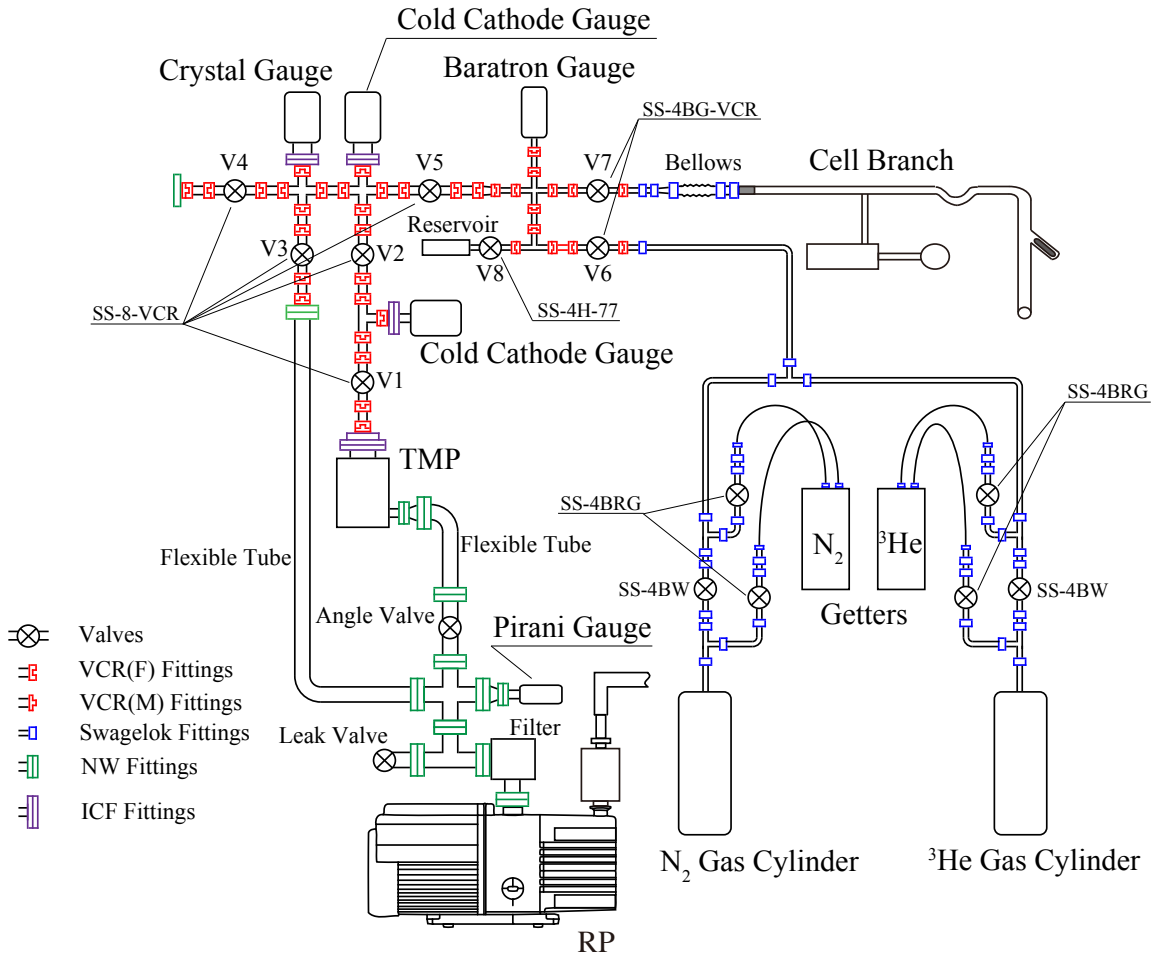

Figure 2.6: A schematic view of the gas filling system.

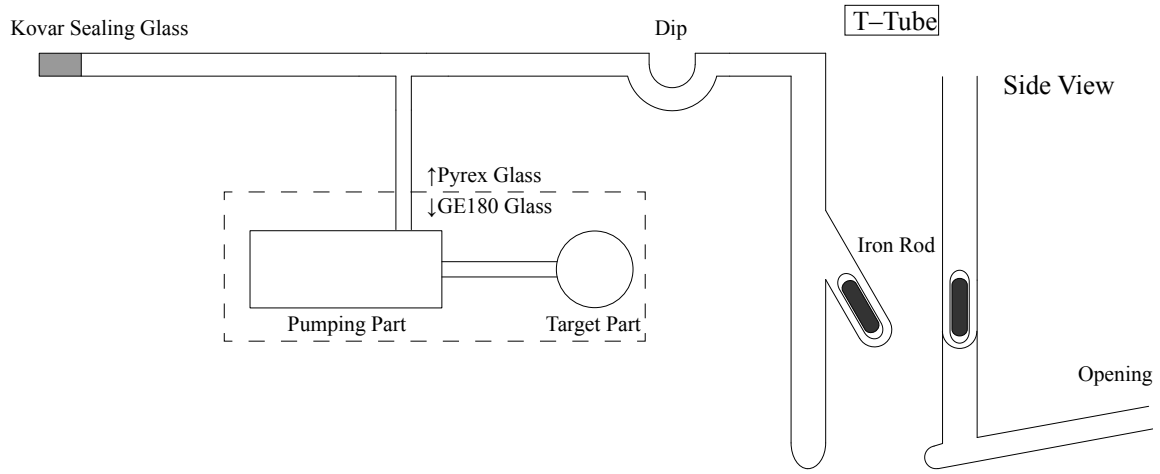

Figure 2.7: A schematic view of the cell branch of SEOP cell.

branch. An iron rod enclosed in Pyrex glass was used to break the alkali metal ampule in a sealed space. The cell branch also had a small bump which was so-called "dip" to collect the alkali metal temporarily. The cell branch of AH-SEOP cell had a another dip at the joint between the branch part and the connection tube (see Fig. 2.8). This dip is to prevent alkali metals from flowing into the gas filling system and help to flow into the target cell.

The vacuum system used a turbo molecular pump (TMP) and a rotary pump (RP). Reachable pressure was typically 8×10^{-7} Pa. We used the four pressure gauges, a Pirani gauge, a crystal gauge, a cold cathode gauge and a capacitance manometer. The Pirani gauge was installed at the RP and was used for pressure measurements during rough evacuations. Crystal gauges utilize the change of the resonance impedance of the crystal oscillator depending on the pressure. The measurable range of crystal gauges is typically from 10^{-2} Pa to atmospheric pressure. Cold cathode gauges convert electrical currents from the ionization of the residual gas to the pressure. The combined measurable range of the cold cathode and crystal gauges is from 5×10^{-1} Pa to 10^{-8} Pa.

We used a Baratron capacitance manometer for the pressure measurement during gas filling to the target cell. This gauge determines a pressure by measuring the change in capacitance between a thin metal diaphragm and an electrode due to the pressure difference. The Baratron gauge can measure pressure which is independent of the composition of the gas being measured. The measurable range is typically from 0.1 Torr to 1000 Torr. The manometer has a voltage output that is proportional to the pressure and vary from 0 to

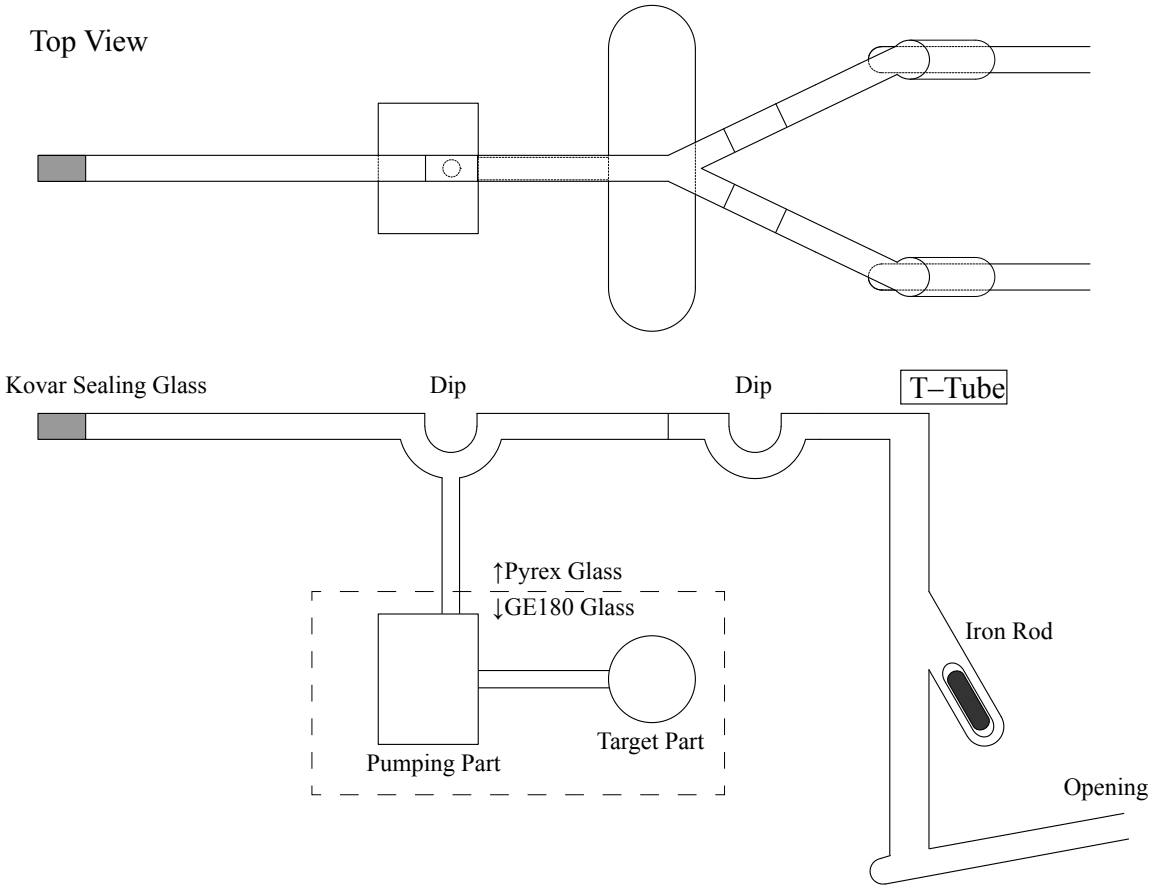

Figure 2.8: A schematic view of the cell branch of AH-SEOP cell.

10 volts. We have made a relative calibration between the Baratron manometer and an aneroid barometer for the gas filling of target cells. Figure 2.9 shows the calibration result of the Baratron gauge. From a linear fit, the relation between the voltage output of the Baratron gauge $V_{\rm bara}$ and the pressure Prs is obtained to be

$$V_{\rm bara}\ [\rm V] = (1.513 \pm 0.003) \times 10^{-3} Prs\ [\rm hPa] - (0.5 \pm 1.0) \times 10^{-3}. \qquad (2.47)$$

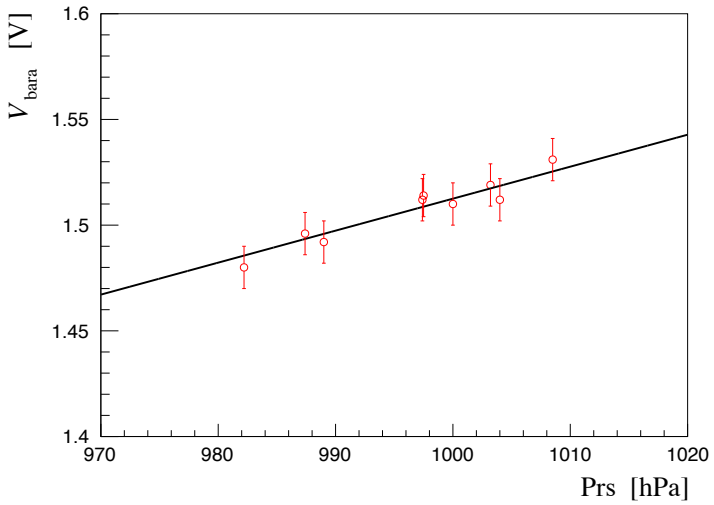

Figure 2.9: The relatiive calibration result of the Baratron capacitance manometer. The solid line shows a linear fitting function.

We used pure gases (the purity of ^{3}He gas was 99.9 % and that of N_2 gas was 99.999 %) for the gas filling of target cells. The gases were further cleaned by using getter gas purifiers. These getter gas purifiers can reduced the impurity levels of the gases to less than 10 ppb.

Manufacturer names and model numbers of the components used in the gas filling system are summarized in Table 2.2.

2.2.3 Gas Filling of Target Cells

We make target cells in the following procedure:

1. Cleaning of cell branch
2. Pressure test and pre-bale-out
3. Insertion of alkali metal ampules

Table 2.2: Manufacturer names and model numbers of the equipment used in the gas filling system.

Equipment	Manufacturer	Model number
TMP	Pfeiffer Vacuum GmbH	HiPace 80
RP	Edwards Ltd.	RV12
Pirani gauge	Pfeiffer Vacuum GmbH	TPR010
Crystal gauge	Canon Anelva Co.	M-320XG
Cold cathode gauge	Pfeiffer Vacuum GmbH	IKR060
Baratron gauge	MKS Instr.	750B
Aneroid barometer	Sato Keiryoki Mfg. Co., Ltd.	7610-20
Getter gas purifier	Saes Getters S.p.A.	GC50

4. Chasing of alkali metals

5. Gas filling

We describe each of these items in the following.

1. Cleaning of cell branch

First, we rinsed the inside of the cell branch with deionized pure water several times. The cell branch was soaked in a 10 % dilute solution of a acid cleaner (OR-IV, Branson Ultrasonics, Emerson Japan Ltd.) at 60 °C for 8 hours. After the several rinses with deionized pure water, the cell branch was soaked in a 10 % dilute solution of a phosphorus-free and pH neutral cleaner (Scat 20X-N, DKS Co., Ltd.) at 50 °C for 6 hours. In order to remove cleaners and impurities inside the cell branch, we further soaked this in deionized pure water at 50 °C for 5 hours. Next, we soaked the cell branch in acetone and performed ultrasonic cleaning for 1 hour. Finally, we rinsed the inside of the cell branch several times with deionized pure water, acetone and ethanol.

2. Pressure test and pre-bale-out

After the cleaning, we attached the cell branch to the vacuum system immediately. Then we flushed the inside the cell branch by flowing N_2 gas several times. For pressure test we filled the cell branch with 3 atm of N_2 gas and heated it to 200 °C using ribbon heaters. Thereafter, we evacuated for two days at ambient temperature to check for vacuum leaks. The cell branch was then baked out under vacuum at 300 °C using ribbon heaters for five days.

3. Insertion of alkali metal ampules

After the bake-out, we filled the cell branch with about 1 atm of N_2 gas and opened the end of the T-tube. Then we put alkali metal ampules (only Rb ampules for a Rb-SEOP cell, Rb and K ampules for an AH-SEOP cell) in the T-tube. After sealing it using a hand torch, we flushed the inside the cell branch with N_2 gas several times. The cell branch was baked out except for around the alkali metal ampules under vacuum for 2 weeks at 300 °C.

4. Chasing of alkali metals

The cell branch is filled with nitrogen gas through the getter gas purifier at a pressure of slightly higher than 1 atm. Then we broke the alkali metal ampules by using the glass-covered iron rod. After evacuation for several hours, we chased the alkali metals into the dip by using ribbon heaters. In the case of an AH-SEOP cell, we first chased K into the dip, and then chased Rb so that the volume ratio of solid K and Rb was approximately the value obtained by Eq. (2.46). After that, we pulled off the T-tubes using a hand torch. The cell branch was further baked out except for the dips under vacuum for 2 days at 300 °C. After the bake-out, we chased the alkali metals into the target cell using ribbon heaters and a heat gun. Finally, we evacuated for 3 days. The pressure usually reaches about 8×10^{-7} Pa.

5. Gas filling

First, we filled the cell branch with about 100 Torr of N_2 gas through the getter gas purifier. After that, the target cell was soaked in liquid N_2, and we filled slightly lower than 1 atm of ^{3}He gas at liquid nitrogen temperature through the getter gas purifier into the cell branch. Finally, we pulled off the target cell from the cell branch using a hand torch.

2.2.4 Measurement of Alkali Metal Number Density Ratios

As described in Section 2.1.4, it is important to optimize the ratio of the alkali metal number densities D to achieve high spin exchange efficiency. However, we don't precisely know D of the AH-SEOP cell made by the above procedure. Therefore, we measured D of the AH-SEOP cell (Ishibashi) using a absorption spectrum of white light.

The intensity of the light transmitted through the cell is expressed as,

$$I(\lambda) = I_0(\lambda) \exp(-\sigma(\lambda)\rho d), \tag{2.48}$$

where $I_0(\lambda)$ is the intensity of incident light per unit wavelength λ. $\sigma(\lambda)$ is the light absorption cross section of atoms, ρ is the number density of atoms and d is the transmission length. Eq. (2.48) is led to

$$\log \frac{I(\lambda)}{I_0(\lambda)} = -\sigma(\lambda)\rho d. \tag{2.49}$$

An integration of the absorption cross section over wavelengths is proportional to a oscillator strength f;

$$\int_{-\infty}^{\infty} \sigma(\lambda) d\lambda \propto f. \tag{2.50}$$

Therefore, D is expressed as,

$$D = \frac{\rho_{\mathrm{K}}}{\rho_{\mathrm{Rb}}} \tag{2.51}$$

$$= \frac{\int \log \frac{I_{\mathrm{K}}(\lambda)}{I_0(\lambda)} d\lambda}{\int \log \frac{I_{\mathrm{Rb}}(\lambda)}{I_0(\lambda)} d\lambda} \frac{f_{\mathrm{Rb}}}{f_{\mathrm{K}}}, \tag{2.52}$$

for the D_1 or D_2 line of Rb and K. D can be obtained from measuring the light absorption spectrum of Rb and K because the oscillator strength of the D_1 (D_2) transition of Rb and K is known. The oscillator strength is shown in Table 2.3.

Table 2.3: The oscillator strengths of the D_1 and D_2 transitions of alkali metals [97, 98].

	f_{Rb}	f_{K}
D_1	0.3424	0.3393
D_2	0.6958	0.6616

Figure 2.10 shows the setup of the absorption spectrum measurement. A halogen lamp was used as a light source. The pumping part of the target cell was inserted into an oven and heated to 120 °C. The operating temperature was monitored by a platinum resistance temperature detector (Pt100) placed inside the oven. The transmission spectrum was measured by a high resolution spectrometer (HR4000, Ocean Optics Inc.). The spectrometer has a wavelength range of $200 - 1100$ nm and resolution of < 0.5 nm. Using an aperture, the light that passes through the pumping part of the target cell is measured.

The results of the absorption spectrum measurement are shown in Fig. 2.11. Although absorption of the transmitted light was not observed at a room temperature, we clearly found the D_1 and D_2 lines of K and Rb at a oven temperature of 120 °C. As a result of this measurement, we obtained the ratio of the alkali metal number densities at a temperature

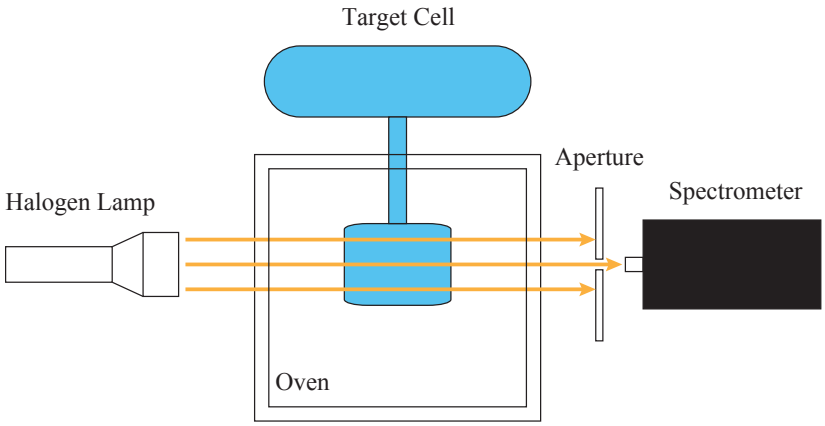

Figure 2.10: Setup of the absorption spectrum measurement.

of 120 °C as,

$$D = 2.0 \pm 0.2. \tag{2.53}$$

Thus, the ratio of the mole fraction of Rb and K is

$$\frac{m_{\mathrm{K}}}{m_{\mathrm{Rb}}} = D\frac{[\mathrm{Rb}]}{[\mathrm{K}]} \simeq 18.4 \pm 1.7. \tag{2.54}$$

Therefore, D at a operating temperature ($T = 230$ °C) is obtained by,

$$D \simeq 3.4 \pm 0.3. \tag{2.55}$$

The ratio was found to be within the appropriate range as suggested in Ref. [92].

2.3 Target Devices

The polarized ^{3}He target system consists of a Helmholtz coil for creating a static magnetic field, gradient field coils, several other coils used for polarimetry, an oven and a laser system used for optical pumping. Figure 2.12 shows the overall setup of the polarized ^{3}He target. In this section, we detail these target devices.

2.3.1 Coils

A static magnetic field is provided by main coils and gradient field coils to define the quantization axis of ^{3}He nuclear spins. The main coils compose a Helmholtz coil to produce a homogeneous magnetic field around the target cell. The gradient field coils are a pair of

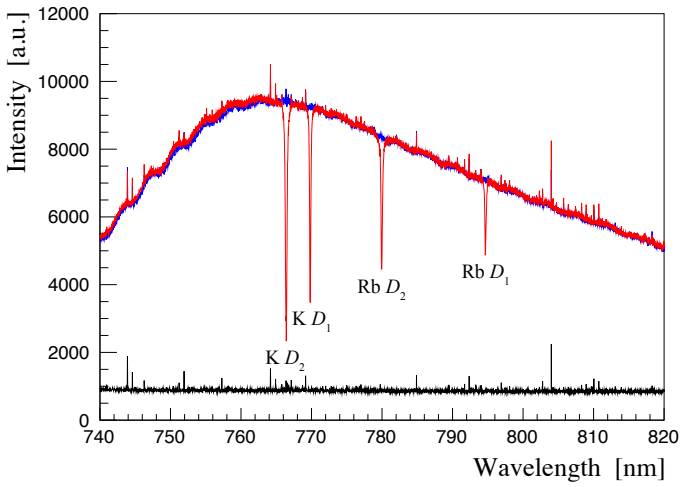

Figure 2.11: Typical measured absorption spectrum. The red (blue) solid line is the transmission spectrum with a oven temperature of 120 °C (a room temperature). The black solid line is a background spectrum.

Table 2.4: Specifications of the main coil and the gradient field coil.

	Main coils	Gradient field coils
Diameter	1000 mmϕ	750 mmϕ
Diameter of a wire	1.7 mmϕ	1.7 mmϕ
Number of turns of each coil	300	100
DC resistance (both in series)	15 Ω	4.4 Ω

circular coils just like a Helmholtz coil, but each coil is slightly tilted as shown in Fig. 2.12. The gradient field coils were used to add inhomogeneities to the static magnetic field to suppress a masing effect. The masing effect is caused by a non-linear coupling between the precession of the magnetization of polarized ^{3}He nuclei and a coil for detecting NMR signals (a pick-up coil). The alternating current induced in the pick-up coil causes an RF magnetic field. This RF magnetic field causes the ^{3}He spin relaxation, resulting in saturation of ^{3}He polarization. It is indicated that the masing effect is suppressed by adding a field gradient [99]. The specifications of the main and gradient field coils are shown in Table 2.4.

Figure 2.13 shows the relation between the exciting current I and the z-component of the magnetic flux density B_z at the center of the coils. As a result of a linear fitting, the

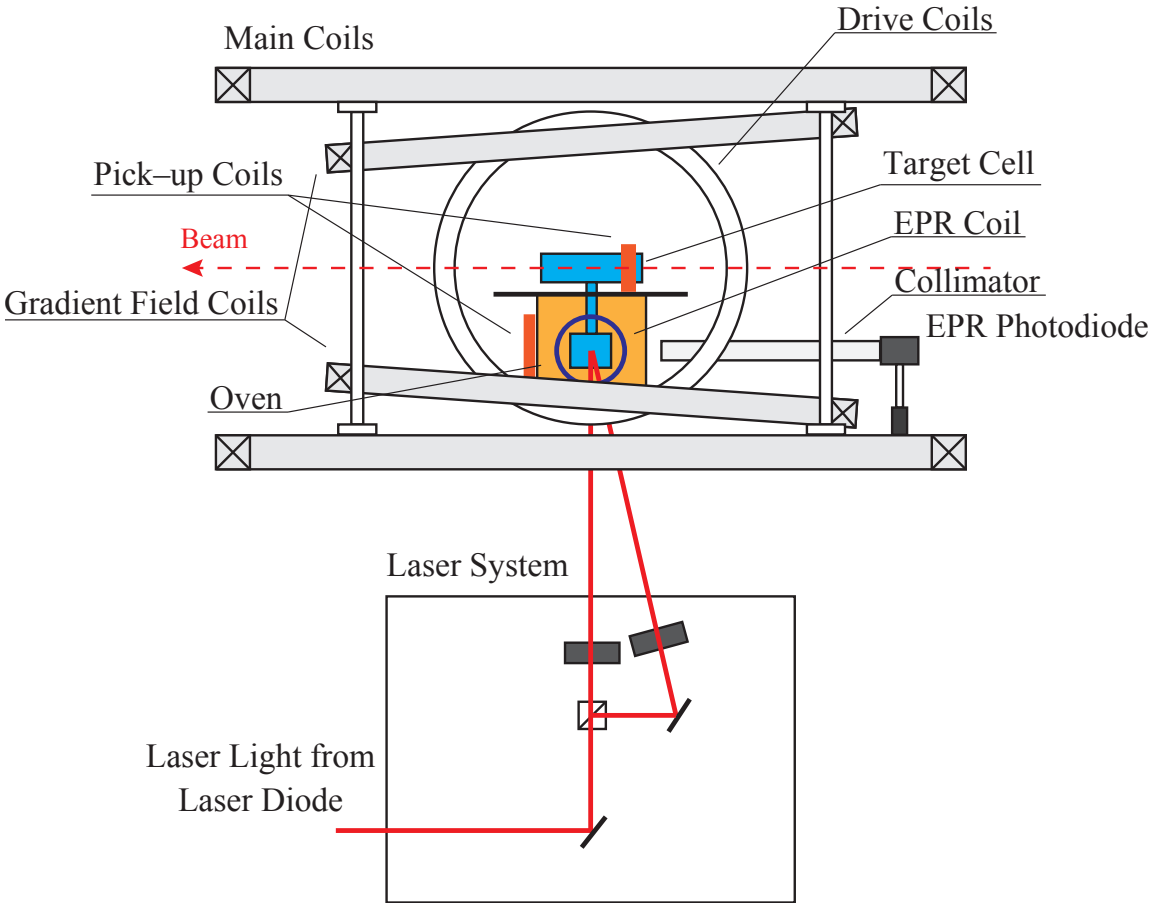

Figure 2.12: The overall setup of the polarized ^{3}He target.

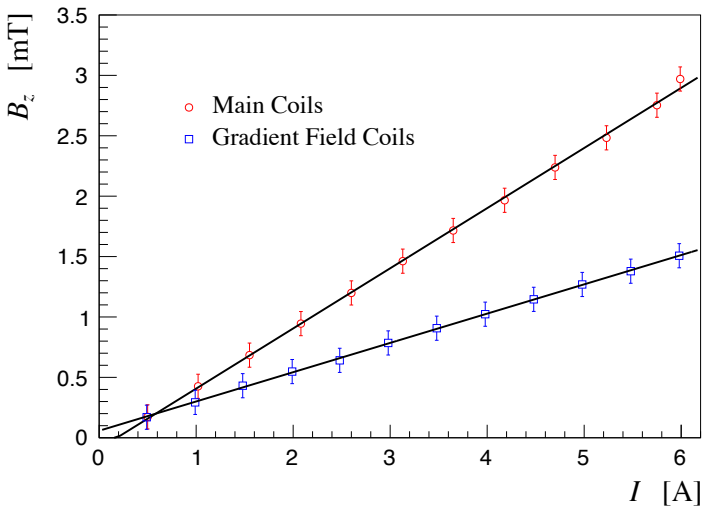

Figure 2.13: Excitation curves of the main coil and the gradient field coil. The solid lines show liner fitting functions.

relation between B_z and I for the main coils is obtained by,

$$B_z \text{ [mT]} = (0.498 \pm 0.016) I \text{ [A]} - (0.091 \pm 0.062). \tag{2.56}$$

Similarly, the relation between B_z and I for the gradient field coils is obtained by,

$$B_z \text{ [mT]} = (0.242 \pm 0.017) I \text{ [A]} + (0.058 \pm 0.061). \tag{2.57}$$

A static magnetic field of about 3 mT can be generated by applying a current of about 6 A to the main coils. The main coils and the gradient field coils were driven with a DC power supply (P/N 030058, Kudo Electric Co., Ltd.) which allowed sweeping the magnetic field for NMR polarimetry.

Drive coils and a EPR coil were used to generate an RF magnetic field for polarimetry as described in Chapter 3. The drive coils which compose a Helmholtz coil generated the RF field which is normal to the direction of a static magnetic field and was used for NMR polarimetry. On the other hand, the RF field generated by the EPR coil was used for EPR polarimetry.

Two pick-up coils were used to detect NMR signals induced by the precession of the magnetization of polarized ^{3}He nuclei. One (Pick-up coil #1) was located so as to cover the target chamber, and the other (Pick-up coil #2) was located outside the oven (see Section 2.3.2) to measure the NMR signal of the pumping chamber. These pick-up coils

Table 2.5: Specifications of the coils used for polarimetry. Pick-up coil #1 (#2) is what was located near the target (pumping) chamber.

	Drive coils	EPR coil	Pick-up coil #1	Pick-up coil #2
Coil diameter	450 mmϕ	100 mmϕ	46 mmϕ	92 mmϕ
Wire diameter	1 mmϕ	1 mmϕ	0.2 mmϕ	0.25 mmϕ
Number of turns	50 (each coil)	3	220	100
DC resistance	3.4 Ω (both in series)	0.4 Ω	18 Ω	272 Ω
Inductance	6.1 mH (both in series)	3.2 μH	3.6 mH	2.3 mH

are placed orthogonal to both drive coils and main coils. A enameled wire with a diameter of 0.2 mm was used as the wire of the pick-up coil #1. We adopt a Manganin insulated wire which has a very small temperature coefficient of resistance with a diameter of 0.25 mm because the pick-up coil #2 was located near the oven. We used non-magnetic coaxial cables as readout and input cables of each coils except for the main coils and the gradient field coils. The specifications of these coils used for polarimetry are shown in Table 2.5.

2.3.2 Target Oven

In order to maintain appropriate alkali metal number densities in the pumping chamber, it is necessary to heat this chamber to $\sim$ 200 °C. Therefore, the pumping chamber of the target cell is placed inside an oven. The pumping chamber was heated by a hot air blower (HOTWIND SYSTEM, Leister Technologies AG) whose temperature and air flow rate can be controlled via inputs. The oven is made of polyetheretherketone (PEEK) which is non-magnetic material and has an operating temperature of up to 250 °C. The oven has three glass windows; one is for the laser entering the oven and the other two, perpendicular to the laser window, for detecting the fluorescent light from the pumping chamber for the EPR measurement (see Section 3.2.2). The temperature inside the oven was monitored by a Pt100. The oven temperature can be automatically set by a Linux computer with a function generator (FG120, Yokogawa Test & Measurement Co.) through GPIB, where the function generator regulates the heater temperature of the hot air blower.

2.3.3 Laser

We used a high power diode laser (LS-795-65W, OptiGrate Co.) for optical pumping. This diode laser contains two fiber-coupled laser head mounted on water-cooling heatsinks and volume Bragg gratings which enable very narrow laser linewidth. Each laser diode can be

Table 2.6: Specifications of the diode laser.

Center wavelength	794.7 nm
Linewidth (FWHM)	< 20 GHz
Maximum output power	65 W
Output fiber core diameter	600 μm
Numerical aperture	0.22

Table 2.7: Specifications of the fiber combiner.

Length	3 m
Input core diameter	600 μm
Output core diameter	1500 μm
Numerical aperture	0.22

individually coupled to an optical fiber. To produce a single output of the laser diodes, we developed a fiber combiner (S/N OPC2-170908-2, Photonic Science Technology Inc.) which combined two fibers into one. The specifications of the diode laser and the fiber combiner are shown in Tables 2.6 and 2.7, respectively.

A schematic view of the laser system is shown in Fig. 2.14. This system consists of a laser module and a laser driver unit that also contains a DC power supply and a temperature controller as well as a software interface. A chiller (HRS012-A-10, SMC Co.) was used for cooling the laser diodes, and a flow of cooling water was monitored by a flowmeter. The laser diode was driven with the DC stabilized power supply (GEN100-7.5, TDK-Lambda Co.). The wavelength of the laser diode was adjusted by controlling the temperature with a thermo-electric cooler and the temperature controller. The thermo-electric cooler was driven with the temperature controller which can be addressed via the software interface.

A excitation curve of the diode laser is shown in Fig. 2.15. The laser power was measured with a power meter (PM150-50, Molectron Detector Inc.). The relation between the output power and the input current was 1.54 W/A from a liner fitting.

2.3.4 Optical System

Circularly polarized light is necessary for optical pumping of Rb atoms. An optical system that provides high power circularly polarized light has been developed. The optical system consists of a polarizing beam splitter (PBS), quarter-wave plates ($\lambda/4$ plate, QWP) and other optical elements. A PBS is an optical element formed with two right angle prisms. The hypotenuse surface of one prism is coated with a dielectric multilayers which reflect S-polarization light and transmits P-polarization light. Note that S (P)-polarization means a electric field of light is normal (parallel) to the plane of incidence. Thus, the incident light is separated into two linearly polarized components (the longitudinal and transverse direction) by passing through a PBS. A QWP is constructed out of a optically anisotropic

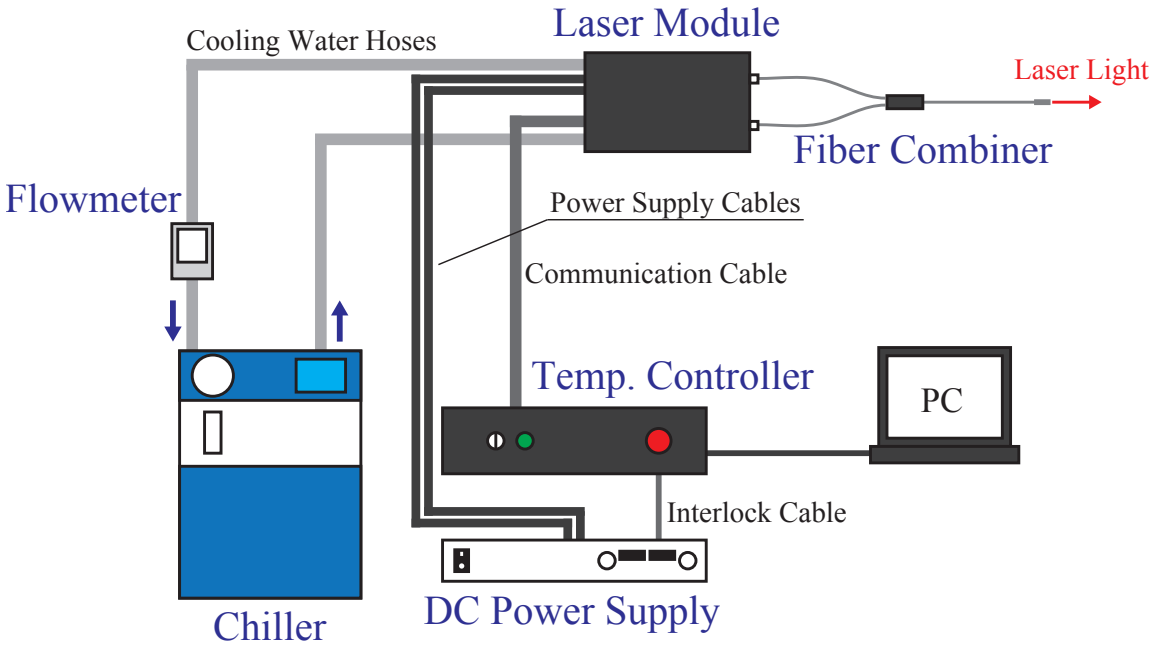

Figure 2.14: A schematic view of the laser system for optical pumping.

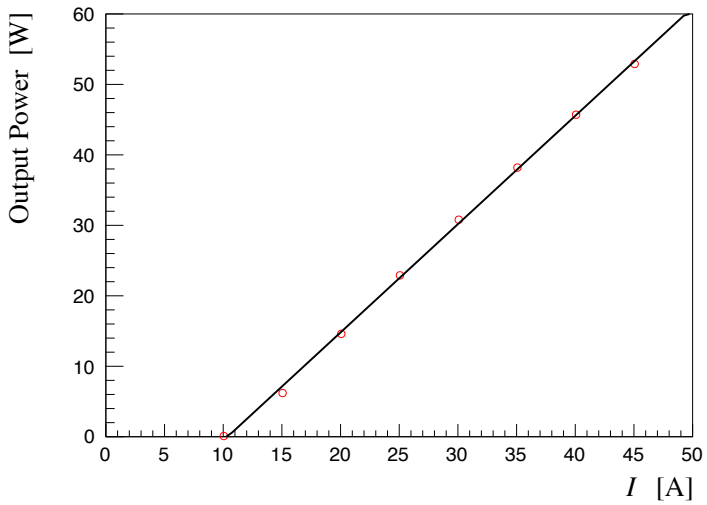

Figure 2.15: A excitation curve of the diode laser. The solid line shows a liner fitting function.

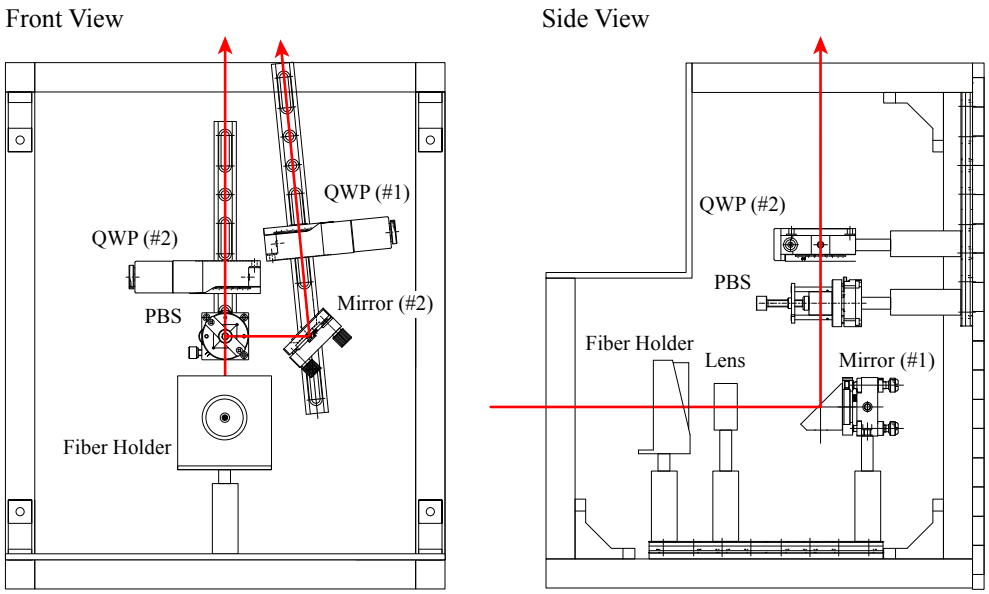

Figure 2.16: The optics system to produce circularly polarized light. This optical system was covered with aluminum plates as a dust cover. We used optical elements and holders produced by SIGMAKOKI Co., Ltd. for this system.

material, and it has two orthogonal axes (a slow axis and a fast axis). This element generates a phase difference of $\pi/2$ between the phases of linear polarized light transmitted along the slow and fast axis. Therefore, when the direction of polarization of the incident light is at an angle of 45° to the axis of a QWP, the exiting light is circularly polarized.

Figure 2.16 shows the optics system used in this work. Output laser light from the fiber combiner is collimated by a plano-convex lens with a focal length of $f = 40$ mm. We adjust the distance between the beam exit of the fiber holder and the lens so that a diameter of the laser light matches to that of the pumping chamber about 1 m away. In fact, the laser light is spread out slightly. After the collimation lens, the laser light is reflected by a mirror (#1) and goes up to the PBS. The light passed through the PBS is converted into circularly polarized light by the QWP (#2). The light reflected by the PBS is again reflected by a mirror (#2) toward the target cell and is converted into circularly polarized light by the QWP (#1).

We measured the circularity of the light after each QWP. We placed another PBS after each QWP and measured the output power of the laser passed through the PBS with a power meter, where the only P-polarized component was measured. The result of this measurement is shown in Fig. 2.17. In the case the laser light is P-polarized before passing

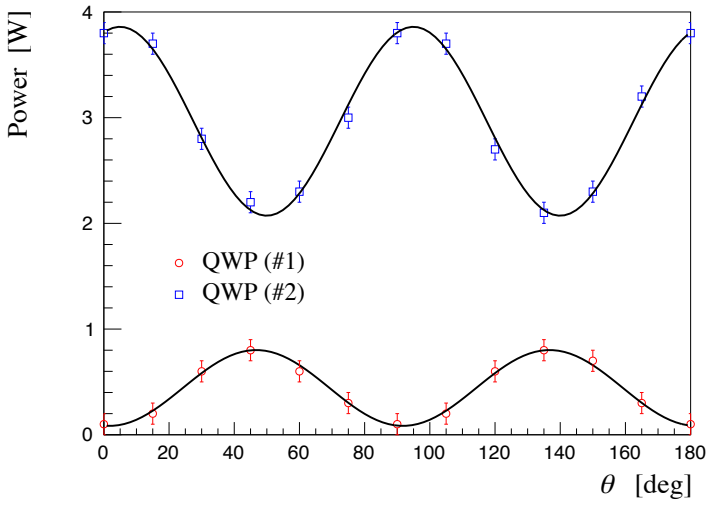

Figure 2.17: Transmitted power as a function of the azimuthal angle θ of the QWPs. The solid curves are fitting functions using Eq. (2.58).

through the QWP, the measured power is the maximum (minimum) when the light after the QWP is linearly (circularly) polarized. On the other hand, in the case the laser light is S-polarized before the QWP, this relation is reversed. The transmitted power W is described as,

$$W \propto \frac{1 \pm \cos^2(2\theta)}{2}, \tag{2.58}$$

where θ is the azimuthal angle of the QWP relative to the plane of linear polarization. The $+$ $(-)$ sign corresponds to P (S)-polarization. Thus, we determined the azimuthal angle of the QWPs to be 45° (135°) for the QWP (#1) and 135° (45°) for the QWP (#2) to produce σ_+ (σ_-) polarized light.

Chapter 3

^{3}He Polarimetry

The absolute value of the ^{3}He polarization is necessary to extract ^{3}He analyzing powers for p–^{3}He elastic scattering. In this work, we used three totally independent methods to evaluate the ^{3}He polarization. The first method is an adiabatic fast passage (AFP) NMR. The second uses an electron paramagnetic resonance (EPR) of alkali metals. The last one is a breakthrough technique based on neutron transmission to directly measure the ^{3}He polarization. We describe the two methods (the AFP-NMR and the EPR measurement) in this chapter, and then discuss a polarization gradient between the target chamber and the pumping chamber. The details of the neutron transmission method are described in Chapter 4.

3.1 Adiabatic Fast Passage NMR

AFP-NMR is a traditional method of flipping the direction of the ^{3}He polarization with a quite small polarization loss. We used the AFP-NMR method to measure the ^{3}He polarization regularly during the scattering experiment. In this section, we describe principles of the AFP-NMR and our devices.

3.1.1 Principle of the AFP-NMR Method

In the presence of a static magnetic field $\boldsymbol{B}$, the magnetization of ^{3}He nuclei $\boldsymbol{M}$ precesses around the direction of the field (z axis). Thus, the motion equation of $\boldsymbol{M}$ is expressed as,

$$\frac{d\boldsymbol{M}}{dt} = \gamma_{^3\mathrm{He}} \boldsymbol{M} \times \boldsymbol{B}, \tag{3.1}$$

where $\gamma_{^3\mathrm{He}}$ is the gyro magnetic ratio of ^{3}He. Here, we consider a reference frame rotating around the z axis at an angular frequency ω. In this frame, the motion equation of $\boldsymbol{M}$ is expressed as,

$$\left(\frac{d\boldsymbol{M}}{dt}\right)_{\mathrm{rot}} = \gamma_{^3\mathrm{He}}\boldsymbol{M} \times \left(\boldsymbol{B} + \frac{\boldsymbol{\omega}}{\gamma_{^3\mathrm{He}}}\right). \tag{3.2}$$

Therefore, the magnetization $\boldsymbol{M}$ senses the effective magnetic field B_{eff} in this frame written as follows,

$$\boldsymbol{B}_{\mathrm{eff}} = \boldsymbol{B} + \frac{\boldsymbol{\omega}}{\gamma_{^3\mathrm{He}}}. \tag{3.3}$$

We consider the case that a radio frequency (RF) field of a magnitude $2B_1$ and a frequency ω is applied in a direction perpendicular to the z axis. The RF field can be decomposed into two counter-rotating components expressed as,

$$\boldsymbol{B}_1 = \begin{pmatrix} 2B_1\cos(\omega t) \\ 0 \\ 0 \end{pmatrix} = \begin{pmatrix} B_1\cos(\omega t) \\ B_1\sin(\omega t) \\ 0 \end{pmatrix} + \begin{pmatrix} B_1\cos(-\omega t) \\ B_1\sin(-\omega t) \\ 0 \end{pmatrix}. \tag{3.4}$$

Considering only the component of the RF filed that rotates in the same direction as the rotating frame, the effective magnetic field is transformed as,

$$\boldsymbol{B}_{\mathrm{eff}} = \left(B + \frac{\omega}{\gamma_{^3\mathrm{He}}}\right)\boldsymbol{e}_z + B_1\boldsymbol{e}'_x, \tag{3.5}$$

where $\boldsymbol{e}'_x = \boldsymbol{e}_x\cos(\omega t) + \boldsymbol{e}_y\sin(\omega t)$ is a unit vector in the reference rotating frame. Note that the other component of the RF field with an angular frequency 2ω doesn't affect the ^{3}He spin because the Bloch-Siegert shift [100] of the resonance frequency due to the counter-rotating field only amounts to $B_1^2/(2B)^2 \sim 10^{-6}$ in general conditions. Consequently, sweeping the static magnetic field across the resonance, $B_0 \equiv -\omega/\gamma_{^3\mathrm{He}}$, the effective magnetic field in the rotating frame is reversed. The AFP-NMR is conceptually illustrated in Fig. 3.1.

Depolarization in the ^{3}He spin flip by the AFP-NMR can be minimized if the following three conditions are met. In order to adiabatically flip the ^{3}He polarization, it is needed to satisfy the three conditions. First, the initial and final RF fields are kept sufficiently smaller than the static magnetic field so that the direction of the effective magnetic field can be almost parallel to that of the static magnetic field (Reversing condition). Therefore, it should be satisfied the following relation:

$$|B - B_0| \gg B_1. \tag{3.6}$$

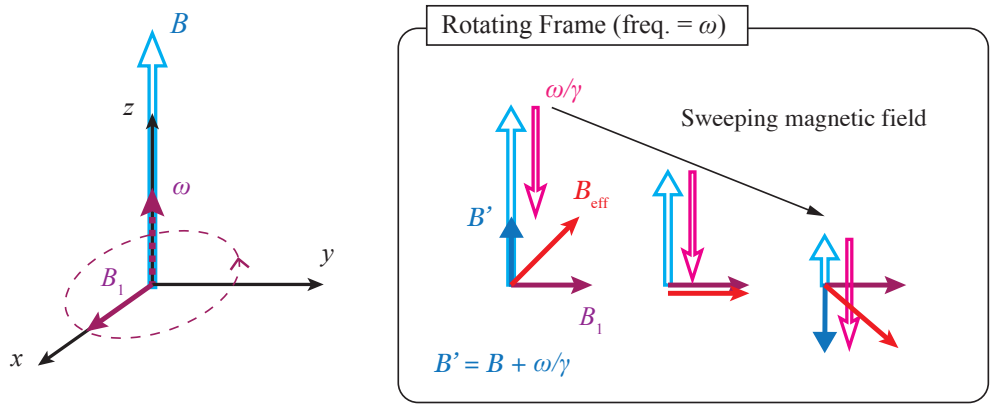

Figure 3.1: Conceptual diagram of the AFP-NMR.

Second, the effective magnetic field $B_{\rm eff}$ must change slowly enough to allow the ^{3}He spins to follow $B_{\rm eff}$ (Adiabatic condition). Thus, the adiabatic condition can be written as,

$$\frac{1}{B_{\rm eff}}\frac{dB_{\rm eff}}{dt} \ll |\gamma_{^3{\rm He}}| B_{\rm eff}. \tag{3.7}$$

Eq. (3.7) is critical when $B_{\rm eff}$ becomes the minimum at the Larmor resonance, and thus the adiabatic condition can be rewritten as,

$$\frac{1}{B_1}\frac{dB}{dt} \ll |\gamma_{^3{\rm He}}| B_1. \tag{3.8}$$

Furthermore, the rate-of-change of $B_{\rm eff}$ must be much faster than the longitudinal spin relaxation time (T_1) as well as the transverse relaxation time (T_2) (Fast passage condition). We assume that T_1 is dominant for the spin relaxation mechanism because T_1 become shorter than T_2 at the resonance [101]. The spin relaxation rate in the rotating frame $1/T_{1\rm r}$ is expressed as [87, 101],

$$\frac{1}{T_{1\rm r}} = D_{^3{\rm He}}\frac{|\nabla B_z|^2}{B_1^2}, \tag{3.9}$$

where $D_{^3{\rm He}}$ is the diffusion constant for the ^{3}He spin. Therefore, the fast passage condition is written by,

$$\frac{1}{B_1}\frac{dB}{dt} \gg D_{^3{\rm He}}\frac{|\nabla B_z|^2}{B_1^2}. \tag{3.10}$$

NMR signals were detected by two pick-up coils located at the target chamber and the pumping chamber. The voltage induced in the pick-up coil at the target chamber by the

precession of the magnetized ^{3}He nuclei is expressed as,

$$V(t) = V_{\rm NMR} \cdot \frac{B_1}{\sqrt{\left(B_0(t) - \frac{\omega}{\gamma_{^3\rm He}}\right)^2 + B_1^2}} \cdot \cos(\omega t) + V_{\rm BG}, \tag{3.11}$$

$$V_{\rm NMR} = \eta n \omega \mu_0 Q M A, \tag{3.12}$$

where $V_{\rm NMR}$ is the amplitude of the induced voltage, and $V_{\rm BG}$ is the background. η is the filling factor which corrects for the finite length of the target chamber covered by the pick-up coil. If the target chamber is sufficiently longer than the pick-up coil, η is approximately 1. n is the number of turns of the pick-up coil, μ_0 is the vacuum permeability and A is the cross-sectional area of the pick-up coil. Q is the Q-value of the detecting system including the pick-up coil. M is the magnetization due to the polarized ^{3}He nuclei and is written by,

$$M = \frac{1}{2} g_{^3\rm He} \mu_{\rm N} P_{^3\rm He} N_{^3\rm He}, \tag{3.13}$$

where $g_{^3\rm He}$ is the g-factor of ^{3}He nucleus and $\mu_{\rm N}$ is the nuclear magneton. $P_{^3\rm He}$ and $N_{^3\rm He}$ is the ^{3}He polarization and the number of ^{3}He nuclei, respectively. Hence, $V_{\rm NMR}$ is proportional to the ^{3}He polarization $P_{^3\rm He}$. We performed the calibration of the NMR signal by the other methods as described below.

3.1.2 AFP-NMR Measurement System

We performed AFP-NMR measurements using the apparatus shown in Fig. 3.2. The system is controlled by a Linux computer via a GPIB. The static magnetic field is produced by the main coils and the gradient field coils that are driven with a DC power supply. Start of the magnetic field sweep is triggered by sending a transistor-transistor logic (TTL) signal to the DC power supply from a function generator (FG120, Yokogawa Test & Measurement Co.). We also use another function generator as a source of the RF current that is provided to the drive coil through an RF amplifier (T145-4016A, Thamway Co.). To obtain a sufficient strength of the RF magnetic field so as to satisfy the AFP conditions, the impedance of the drive coil circuit is minimized by using a resonance capacitor. The induce voltages in the pick-up coils are detected by lock-in amplifiers (SR830, SRS Inc.). For the pick-up coil at the target chamber, we use a parallel resonance circuit with a capacitor to narrow the frequency band width. In order to reduce the background voltage induced by the RF field, a sinusoidal voltage with the same frequency and amplitude is subtracted from the induced

Table 3.1: Typical AFP parameters.

RF frequency	85 kHz
B_0	2.62 mT
Sweeping range	$1.24 - 2.95$ mT
Sweeping rate	0.096 mT/sec
B_1	~ 2 μT

voltage of each pick-up coil (at the lock-in amplifier inputs). The amplitude and phase of the sinusoidal voltage are tuned so as to minimize the mixed voltage (the subtracted voltage) in the absence of the AFP-NMR signal. This tuning is performed every time before the NMR measurement. Typical AFP parameters are summarized in Table 3.1, and a typical NMR signal at the target chamber is shown in Fig. 3.3. The peak height of the NMR signal measured for the target chamber is obtained by fitting with Eq. (3.11). We take the errors of the signal heights from the uncertainty of the fitting results, which is ~ 2 % of the signal height. On the other hand, the NMR signal of the pumping chamber is much smaller than that of the target chamber. The typical signal height is on the order of 100 μV to 1 mV. Therefore, we obtained the signal height simply from the difference between the peak top and the baseline, and estimated the error from the standard deviation of the baseline. The error of the signal height at the pumping chamber fluctuates depending on the noise and the drift of the static magnetic field. As a result, we estimated the error to be about 5 to 10 %.

3.1.3 AFP-Loss

We observed a decrease of the ^{3}He polarization in the AFP-NMR measurement due to imperfect AFP conditions in our AFP-NMR ("AFP-loss"). It is necessary to know the AFP-loss in each of the chambers to evaluate the ^{3}He spin relaxation rate for the estimation of the cell temperature.

We measured the AFP-loss by performing a series of the NMR measurements about ten times in a short period. Figure 3.4 shows typical results of the AFP-losses for the Koganei and the Ishibashi cells. The AFP-loss in the Koganei cell at the pumping chamber is relatively large because this part of the Koganei cell is longer than that of the Ishibashi cell. In the AFP-loss measurement, the i-th NMR signal height is written by,

$$V_i = (1 - \alpha)^i V_0, \tag{3.14}$$

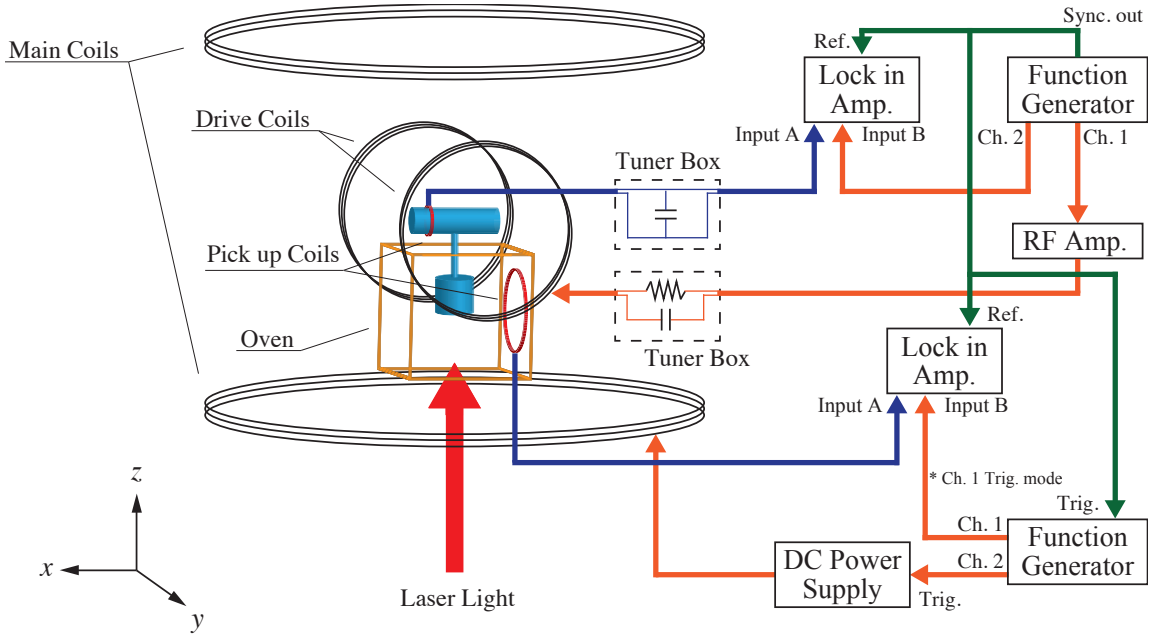

Figure 3.2: A schematic view of the AFP-NMR system.

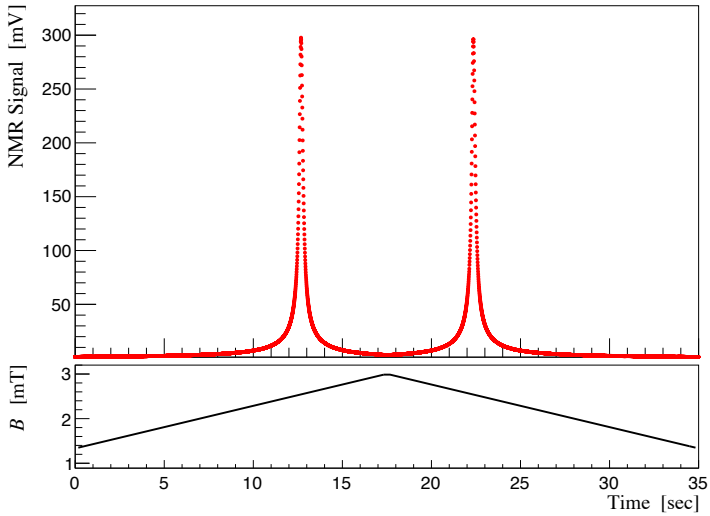

Figure 3.3: A typical NMR signal measured by the AFP-NMR system. Bottom panel shows the static magnetic field sweep.

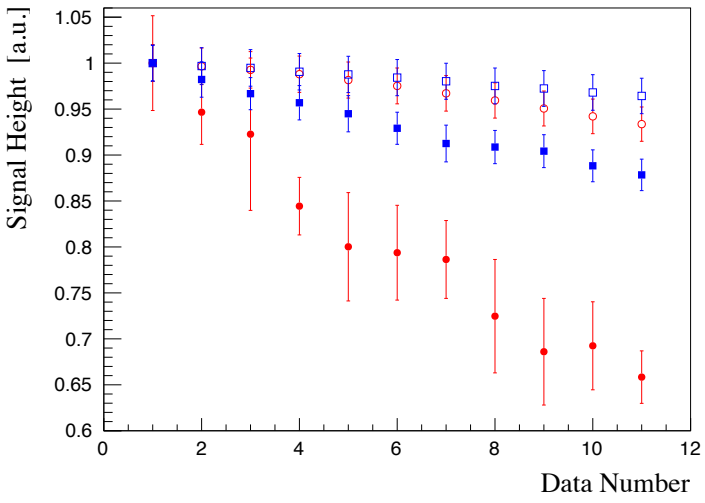

Figure 3.4: Typical results of the AFP-loss measurement. The red (blue) symbols are the data of the Koganei (Ishibashi) cell. The open (filled) circles and squares shows the AFP-loss in the target (pumping) chamber.

Table 3.2: AFP-losses per measurement in the target and pumping chamber in %.

Cell name	Target	Pumping
Koganei	0.7 ± 0.3	4.1 ± 0.6
Ishibashi	0.4 ± 0.3	1.3 ± 0.3

where α is the AFP-loss per measurement and V_0 is the initial signal height. Therefore, the AFP-loss is given by,

$$1 - \alpha = \left(\frac{V_i}{V_0} \right)^{\frac{1}{i}}. \tag{3.15}$$

Using Eq. (3.15) and comparing the initial and final ^{3}He polarization of the series of the measurements, we obtained the AFP-loss in the target and pumping chambers for both cells and listed in Table 3.2.

3.2 Electron Paramagnetic Resonance of Alkali Metals

The ^{3}He polarization can be evaluated from the frequency shift of the Zeeman resonance of alkali metals. This electron paramagnetic resonance (EPR) measurement has been applied to a calibration of the NMR signal. In this section, we describe principles of the EPR

Table 3.3: The electronic and nuclear g-factors for ^{85}Rb and ^{39}K [102]. m_e and $m_{\rm N}$ are the electron and nuclear mass, respectively.

Electron spin g-factor g_S	2.002
Electron orbital g-factor g_L	$1 - m_e/m_{\rm N}$
Nuclear g-factor g_I (^{85}Rb)	-2.936×10^{-4}
Nuclear g-factor g_I (^{39}K)	-1.419×10^{-4}

measurement and our EPR system.

3.2.1 Principle of the EPR Measurement

In the presence of an external magnetic field, the degenerate hyperfine structure levels of an alkali metal are split into sub levels characterized by magnetic quantum numbers (the Zeeman effect). The hyperfine interaction arises from the coupling of the nuclear spin $\boldsymbol{I}$ with the total spin $\boldsymbol{F} = \boldsymbol{I} + \boldsymbol{J}$, where $\boldsymbol{J} = \boldsymbol{L} + \boldsymbol{S}$ is the total angular momentum of the valence electron of an alkali metal. $\boldsymbol{L}$ and $\boldsymbol{S}$ are the orbital angular momentum of the valence electron and its spin, respectively. The Hamiltonian which describes the hyperfine structure for the two excited states of an alkali metal is given by [102],

$$H_{\rm hfs} = A_{\rm hfs}\boldsymbol{I}\cdot\boldsymbol{J} + B_{\rm hfs}\frac{3(\boldsymbol{I}\cdot\boldsymbol{J})^2 + \frac{3}{2}(\boldsymbol{I}\cdot\boldsymbol{J}) - I(I+1)J(J+1)}{2I(2I-1)J(2J-1)}, \tag{3.16}$$

where $A_{\rm hfs}$ is the magnetic dipole constant and $B_{\rm hfs}$ is the electric quadrupole constant for the hyperfine structure. In the presence of an magnetic field, the Hamiltonian which describes the Zeeman effect is

$$H_{\rm B} = \frac{\mu_{\rm B}}{\hbar}(g_S\boldsymbol{S} + g_L\boldsymbol{L} + g_I\boldsymbol{I})\cdot\boldsymbol{B}, \tag{3.17}$$

where g_S, g_L and g_I are the electron spin, electron orbital and nuclear g-factors, respectively. The values of these g-factors are summarized in Table 3.3. Therefore, the total hyperfine interaction in the presence of a magnetic field is written by,

$$H_{\rm total} = H_{\rm hfs} + H_{\rm B}. \tag{3.18}$$

In the case of the ground state ($L = 0$, $S = 1/2$), the energy eigenvalues of Eq. (3.18) are given by the Breit-Rabi formula [103];

$$E(F = I \pm 1/2, m_F) = -\frac{\Delta W}{2(2I+1)} + g_I\mu_{\rm B}m_F B_0 \pm \frac{\Delta W}{2}\left(1 + \frac{4m_F}{2I+1}x + x^2\right)^{\frac{1}{2}}, \tag{3.19}$$

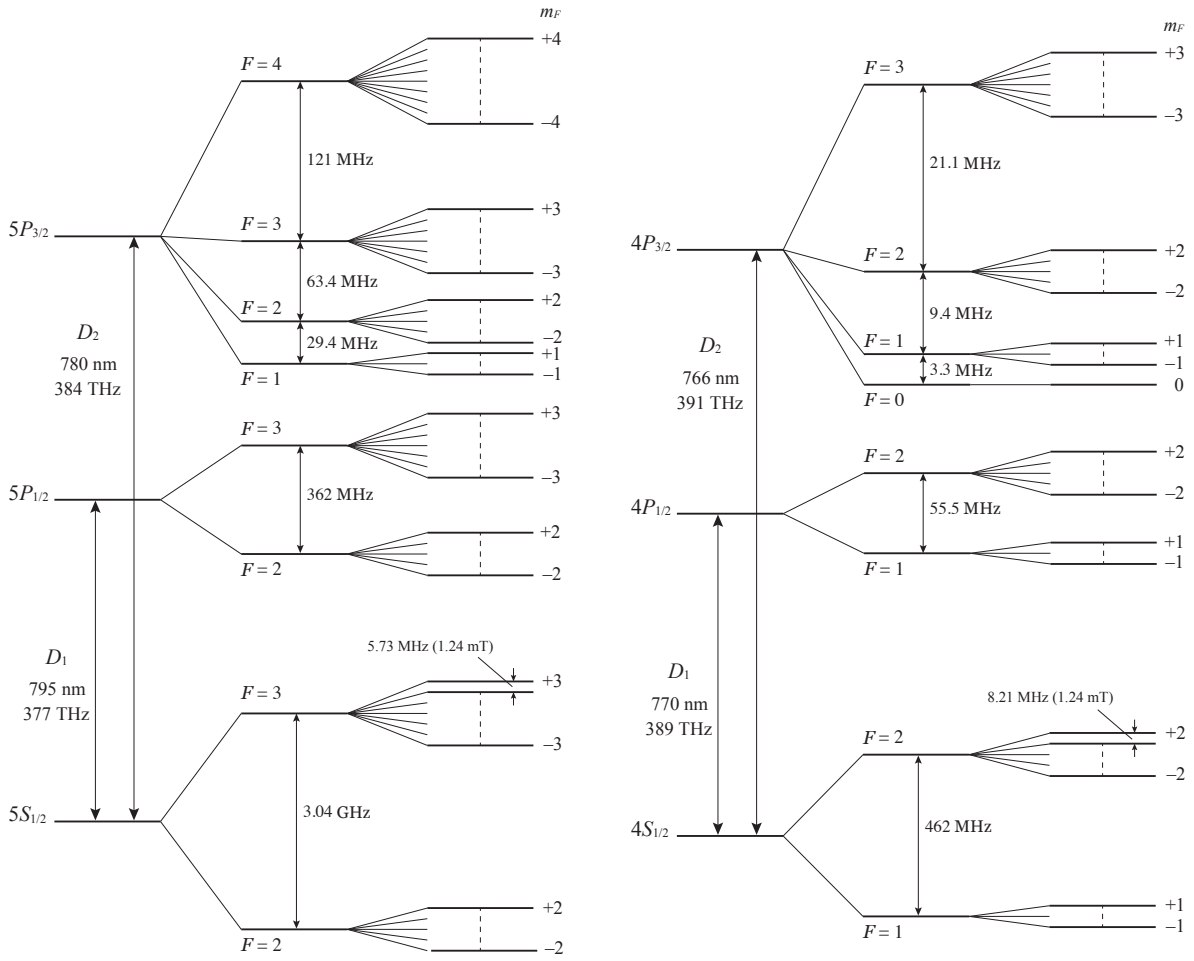

(a) ^{85}Rb, $I = 5/2$ (b) ^{39}K, $I = 3/2$

Figure 3.5: Energy levels of ^{85}Rb (a) and ^{39}K (b) with the hyperfine structure and the Zeeman splitting (not to scale).

$$x = \frac{(g_J - g_I)\mu_B}{\Delta W} B_0, \tag{3.20}$$

where $\Delta W = A_{\rm hfs}(I + 1/2)$ is the hyperfine splitting in the absence of a external magnetic field. g_J is the g-factor of the total angular momentum $\boldsymbol{J}$ of the electron. In this case (for the ground state), g_J is almost equal to g_S. The calculated energy levels of ^{85}Rb for the ground state ($5S_{1/2}$) as a function of the external magnetic field are shown in Fig. 3.6. By the optical pumping with circularly polarized (σ^+) light, alkali metal atoms are populated in $(F, m_F) = (3, +3)$ state for ^{85}Rb or $(F, m_F) = (2, +2)$ state for ^{39}K according to the selection rule of angular momenta. Applying an RF field with a frequency corresponding to the energy difference between the Zeeman sub levels (EPR frequency), the transition between these levels can be induced. The EPR frequency corresponding to the transition $(F, m_F) \to (F, m_F - 1)$ is written by,

$$\nu_{m \to m-1} = \frac{E(F, m_F) - E(F, m_F - 1)}{h}. \tag{3.21}$$

Expanding the third term of Eq. (3.19) to the second order in terms of x by a Taylor series, the following equation is obtained;

$$\frac{\Delta W}{2}\left(1 + \frac{4m_F}{2I+1}x + x^2\right)^{\frac{1}{2}} \approx \frac{\Delta W}{2}\left[1 + \frac{2m_F}{2I+1}x + \frac{1}{2}\left(1 - \frac{4m_F^2}{(2I+1)^2}\right)x^2\right]. \tag{3.22}$$

From Eq. (3.21) and (3.22), the EPR frequency is approximately,

$$\nu_{m \to m-1} \approx \frac{g_I \mu_B B_0}{h} + \frac{\Delta W}{h(2I+1)}x - \frac{(2m_F - 1)\Delta W}{h(2I+1^2)}x^2. \tag{3.23}$$

Using $g_J \gg g_I$ and $\Delta W = A_{\rm hfs}(I + 1/2)$, Eq. (3.23) is expressed as,

$$\begin{aligned}
\nu_{m \to m-1} &\approx \frac{\Delta W}{h(2I+1)}\frac{g_J \mu_B B_0}{\Delta W} - \frac{(2m_F - 1)\Delta W}{h(2I+1)^2}\left(\frac{g_J \mu_B B_0}{\Delta W}\right)^2 \\
&\approx \frac{\mu_B g_S}{h(2I+1)}\left(B_0 - \frac{(2m_F - 1)\mu_B g_S}{(2I+1)\Delta W}B_0^2\right) \\
&= \frac{\mu_B g_S}{h(2I+1)}\left(B_0 - \frac{2(2m_F - 1)}{(2I+1)^2}\frac{\mu_B g_S}{h A_{\rm hfs}}B_0^2\right),
\end{aligned} \tag{3.24}$$

where we used $g_J \approx g_S$. Figure 3.7 shows the EPR frequency for ^{85}Rb and ^{39}K as a function of the magnetic field, which is calculated by using Eq. (3.24).

The shift of the EPR frequency is caused by two effects. The first one is due to an effective magnetic field generated by the spin exchange interaction between ^{3}He nuclei and

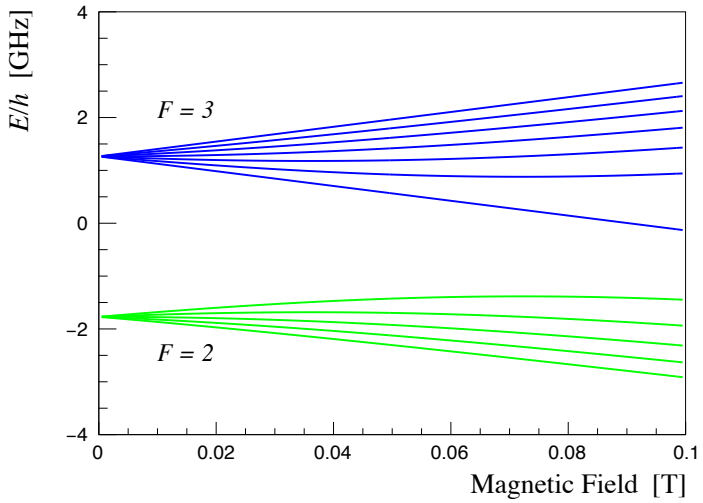

Figure 3.6: ^{85}Rb energy levels of the ground state ($5S_{1/2}$) as a function of the external magnetic field.

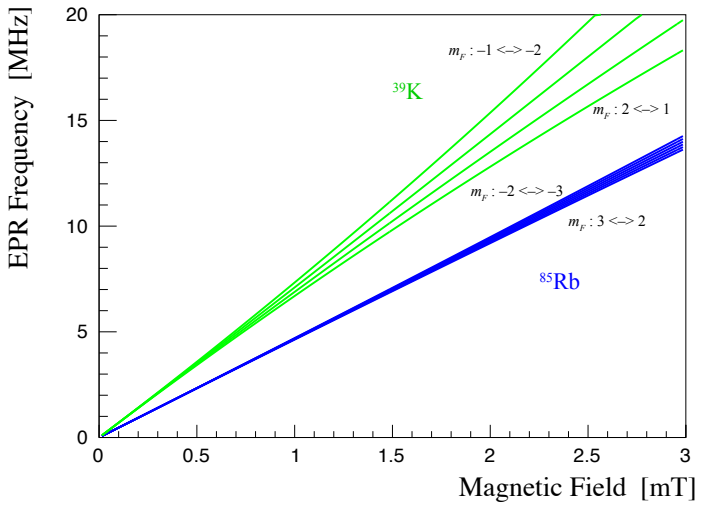

Figure 3.7: Frequency of the EPR transition $(F, m_F) \rightarrow (F, m_F - 1)$ for the ground state of ^{85}Rb and ^{39}K as a function of the external magnetic field.

alkali metal atoms. This effective magnetic field $B_{\rm SE}$ is written as follows [104];

$$B_{\rm SE} = \frac{2K_{\rm SE}\Gamma_{\rm SE}\hbar}{g_e\mu_{\rm B}}\langle K_z\rangle, \tag{3.25}$$

where $\Gamma_{\rm SE} = [^3{\rm He}]\langle\sigma_{\rm SE}v\rangle$ is the spin exchange rate per an alkali atom, and $\langle K_z\rangle$ is the z-component of the ^{3}He nuclear spin. Note that $P_{^3{\rm He}} = \langle K_z\rangle/K$. $K_{\rm SE}$ is a frequency shift parameter which is defined as the ratio of the imaginary and real parts of the spin exchange cross section [105]. Thus, the frequency shift due to this effective magnetic field $\Delta\nu_{\rm SE}$ is given by,

$$\Delta\nu_{\rm SE} = \frac{d\nu_{\rm ESR}}{dB}B_{\rm SE} = \frac{d\nu_{\rm ESR}}{dB}\frac{2K_{\rm SE}[^3{\rm He}]\langle\sigma_{\rm SE}v\rangle\hbar}{g_e\mu_{\rm B}}\langle K_z\rangle. \tag{3.26}$$

The other effect of the frequency shift arises from the classical magnetic field created by ^{3}He magnetization. Assuming that the magnetization created by polarized ^{3}He nuclei is spherically uniform, the magnetic field B_M is written as,

$$B_M = \frac{2\mu_0}{3}M = \frac{2\mu_0}{3}\mu_{^3{\rm He}}[^3{\rm He}]P_{^3{\rm He}}, \tag{3.27}$$

where $\mu_{^3{\rm He}}$ is the magnetic moment of ^{3}He nuclei. Therefore, the frequency shift due to this classical magnetic field $\Delta\nu_M$ is given by,

$$\Delta\nu_M = \frac{d\nu_{\rm ESR}}{dB}B_M = \frac{d\nu_{\rm ESR}}{dB}\frac{2\mu_0}{3}\mu_{^3{\rm He}}[^3{\rm He}]P_{^3{\rm He}}. \tag{3.28}$$

Consequently, the total frequency shift is expressed as the sum of Eqs. (3.26) and (3.28);

$$\begin{aligned}\Delta\nu &= \Delta\nu_{\rm SE} + \Delta\nu_M \\ &= \frac{d\nu_{\rm ESR}}{dB}(B_{\rm SE} + B_M) \\ &= \frac{2\mu_0}{3}\frac{d\nu_{\rm ESR}}{dB}\kappa_0\mu_{^3{\rm He}}[^3{\rm He}]P_{^3{\rm He}},\end{aligned} \tag{3.29}$$

where κ_0 is a dimensionless constant which depends on temperature. κ_0 has been measured for ^{85}Rb up to 350 °C and ^{39}K up to 230 °C, respectively [104, 106];

$$\kappa_0^{\rm Rb} = 6.39 + 0.00914(T - 200\ [^\circ{\rm C}]), \tag{3.30}$$

$$\kappa_0^{\rm K} = 5.99 + 0.0086(T - 200\ [^\circ{\rm C}]). \tag{3.31}$$

Therefore, from Eq. (3.24) and (3.29), the EPR frequency shift is obtained by,

$$\Delta\nu(m_F = \pm F) = \frac{2\mu_0}{3}\frac{\mu_{\rm B}g_S}{h(2I+1)}\left(1 \mp \frac{8I}{(2I+1)^2}\frac{\mu_{\rm B}g_SB_0}{hA_{\rm hfs}}\right)\kappa_0\mu_{^3{\rm He}}[^3{\rm He}]P_{^3{\rm He}}, \tag{3.32}$$

where we used $m_F = \pm F = \pm(I + 1/2)$. A typical frequency shift is on the order of 1 to 10 kHz, whereas the EPR frequency is on the order of 1 to 10 MHz in our conditions. Actually, in order to isolate the shift due to polarized ^{3}He, we measured the frequency difference between the two opposite polarization states.

3.2.2 EPR System

During optical pumping with circularly polarized (σ_+) light, most of the alkali metal atoms are in the $(F, m_F) = (3, +3)$ ground state for ^{85}Rb and the $(F, m_F) = (2, +2)$ ground state for ^{39}K. If we apply an RF magnetic field with a frequency corresponding to the $\Delta m_F = 1$ transition, the alkali metal atoms decay into the $(F, m_F - 1)$ ground state. In the case of hybrid SEOP, ^{39}K atoms are populated in the $m_F = +2$ state due to the spin exchange with ^{85}Rb atoms during the optical pumping since the spin exchange rate is very large ($\sim 10^5$–10^6 s^{-1}). Applying an RF field corresponding to the transition energy of ^{39}K depolarizes both ^{39}K and ^{85}Rb polarizations accordingly. Then, Rb atoms absorb the circularly polarized light and are excited to the $P_{1/2}$ state. Some of the excited Rb atoms are further excited to the $P_{3/2}$ state by collisions with other atoms. Although most of the excited atoms non-radiatively transition to the ground state by the N_2 buffer gas, a small fraction ($\sim$ 3 %) of the atoms decays with fluorescence emissions at D_1 and D_2 lines. The fluorescence intensity is the minimum under the normal optical pumping, but it instantaneously increases once an RF field at the transition energy is applied. The EPR frequency can be found by monitoring the fluorescence intensity change with a frequency modulated RF field.

Figure 3.8 shows the EPR system used in this work. The RF field is created by an EPR coil, which has three turns with a diameter of 10 cm, placed near the pumping chamber inside the oven. We detect the fluorescence from the cell by using a photodiode (S2387-1010R, Hamamatsu Photonics K.K.) and a band pass filter at the Rb D_2 line (VPFIT-12.5C-7800, SIGMAKOKI Co., Ltd.) to shut out the scattered laser light which has a same wavelength as the D_1 line of Rb. The center wavelength of the band pass filter is 780 nm and the FWHM is 4.25 nm. In order to block other light such as room light and collect the fluorescence, we use an aluminum pipe as a collimator. The photodiode is connected to a current to voltage converter (T-IVA001BZ, Turtle Industry Co., Ltd.), of which output is recorded on a digital oscilloscope (PicoScope 5243A, Pico Technology Ltd.). The digital oscilloscope has a signal generator output which can produce built-in functions

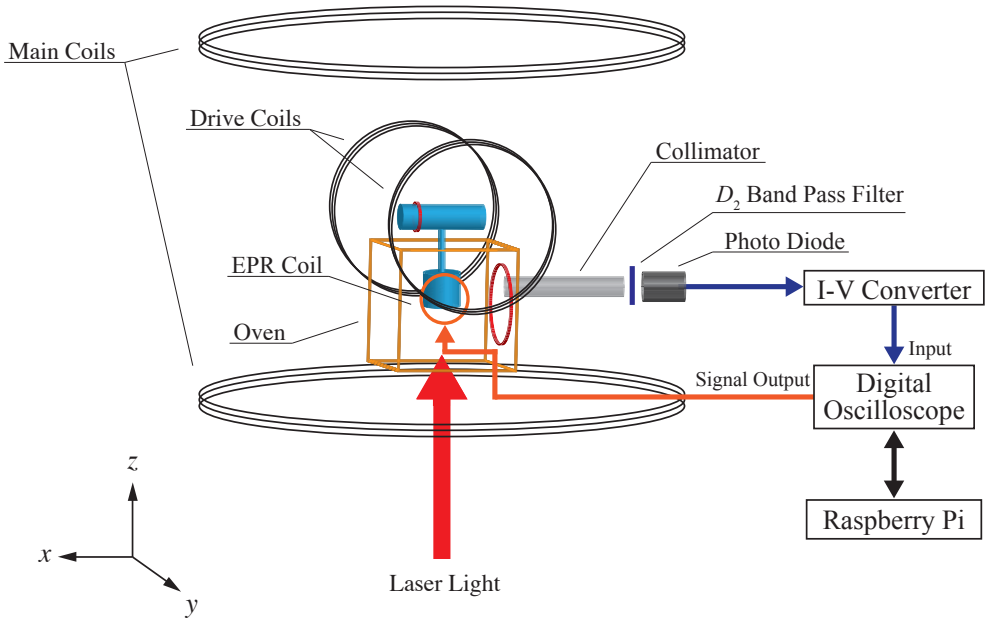

Figure 3.8: A schematic view of the EPR system.

Table 3.4: Operating parameters for the EPR measurement.

RF frequency (^{85}Rb transition)	$\sim$ 5.8 MHz
RF frequency (^{39}K transition)	$\sim$ 8.1 MHz
Modulation frequency	83 Hz
Frequency deviation	50 kHz
Measuring time	0.5 sec/data

and arbitrary waveforms. We use the function generator output of the oscilloscope as a source of the RF field. The RF frequency is modulated with a triangle wave in the build-in function generator. The digital oscilloscope is controlled by a computer (Raspberry Pi), and the recorded data is transferred to it. We perform phase-sensitive detection of the input voltage referenced to the modulation frequency on the Raspberry Pi computer. Using the result of the phase-sensitive detection, we also perform a feed-back control so that the center frequency of the modulated RF will match the EPR frequency, and the center frequencies are recorded on the computer. The operating parameters of the EPR measurement are listed in Table 3.4.

As described above, we measured the frequency difference between the two polarization states to isolate the frequency shift due to the ^{3}He polarization. The direction of ^{3}He spins was reversed by the AFP-NMR method. A typical data of the EPR measurement is shown

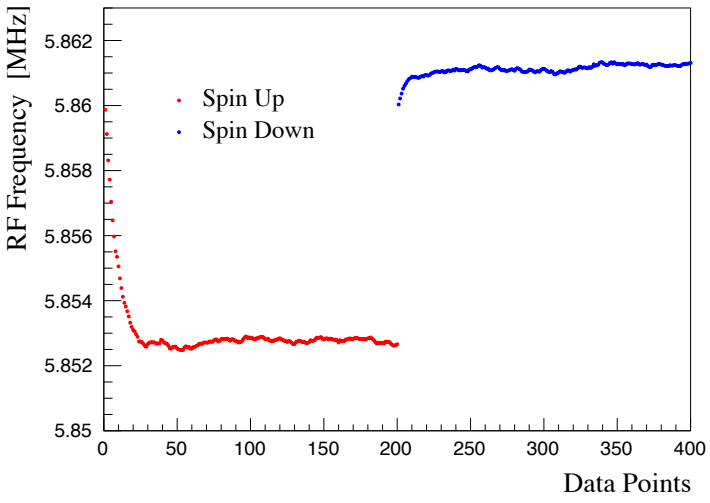

Figure 3.9: Typical data of the EPR frequency shift measurement. The red (blue) dots mean the direction of ^{3}He spin is upward (downward). It can be seen that the RF frequency is "locked" to the EPR frequency by the feed-back control.

in Fig. 3.9. The frequency difference between the two polarization states corresponds to $2\Delta\nu$. The EPR frequency shift was obtained with an error of less than 0.5 %, which mainly came from the fluctuations of the static magnetic field. The EPR method gives us only the ^{3}He polarization in the pumping chamber. In order to extract ^{3}He analyzing powers for p–^{3}He elastic scattering, we need to know the ^{3}He polarization in the target chamber where the proton beams enter during the scattering experiment. Therefore, it is necessary to consider polarization dynamics in the two chambers. In the following section, we discuss about the dynamics of SEOP in a double-chamber cell.

3.3 Polarization in a Target Chamber

It is needed to know the ^{3}He polarization in the target chamber for the measurement of ^{3}He analyzing powers. There is a polarization gradient between the two chambers since polarized ^{3}He is produced only at the pumping chamber by optical pumping and diffuses to the target chamber. However, we can't measure the polarization of the target chamber directly by our polarimetry system. In this section, we discuss the dynamics of SEOP in a double cell and estimate the ^{3}He polarization in the target chamber.

Table 3.5: Target cell volumes in cm^3.

Cell name	Target	Pumping	Transfer tube	Total
Koganei	157 ± 5	116 ± 5	3.1 ± 1.0	276 ± 7
Ishibashi	173.6 ± 0.5	102.9 ± 0.5	2.2 ± 0.1	278.7 ± 0.5

3.3.1 Cell Parameters

For discussing about the dynamics of SEOP, we first describe the parameters of the target cell, namely, volumes, densities and temperatures. These parameters are very important to evaluate the ^{3}He polarization of the target cell.

The volumes of the cells are necessary for corrections to the number density of ^{3}He because the temperatures of the two chambers are different during operation. We evaluated the volumes from the cell dimensions and glass thicknesses for the Koganei cell after the gas filling and by filling water for the Ishibashi cell before the gas filling. The volumes of the target cells are listed in Table 3.5. While the errors on the measurements with water are quite small, those on the cell dimensions are relatively large. The errors on the volumes of the Koganei cell are dominated by the measurements of glass thicknesses. This is because the glass thickness of the cell considerably varies. Hence, we measured the glass thicknesses at several points and evaluated the errors from the variation in the measured values. However, the errors of the volumes do not much affect the ^{3}He number density in each chamber as we will see in Eqs. (3.33) and (3.34).

The ^{3}He number density is necessary for an accurate EPR polarimetry since the EPR frequency shift is proportional to the ^{3}He number density as in Eq. (3.32). Our traditional method of determining the ^{3}He number density was the pressure measurement in the vacuum system during the cell filling with ^{3}He gas. However, the temperature inside the cell is uncertain because the cell is soaked in liquid N_2 while the cell is being sealed with a gas torch. In order to evaluate the ^{3}He number densities in the cells with high accuracy, we performed measurements of the neutron transmission for the cells in the previous study [107]. The neutron transmission measurement used the fact that ^{3}He nuclei have a large absorption cross section for low energy neutrons. We performed the measurement using a neutron source at RIKEN. The details of the experiment will be described in Chapter 4. Table 3.6 shows the ^{3}He number densities in the cells obtained in Ref. [107]. The ^{3}He number densities were obtained with errors of less than 5 %.

The pumping chamber was heated in an oven to obtain a sufficient amount of alkali

Table 3.6: ^{3}He number densities of the target cells obtained from the previous study [107]. The statistical and systematic errors are also shown.

Cell name	^{3}He number density $\times 10^{19}$ [cm^{-3}]
Koganei	$8.18 \pm 0.04_{(\mathrm{sta})} \pm 0.37_{(\mathrm{sys})}$
Ishibashi	$7.90 \pm 0.04_{(\mathrm{sta})} \pm 0.36_{(\mathrm{sys})}$

metal vapor while the target chamber was in ambient temperature. Thus, the temperatures of the two chambers are quite different. From the equation of state of the ideal gas, the ^{3}He number densities in the target and pumping chambers are given by,

$$n_{\mathrm{tc}} = \frac{n_0}{1 + \frac{V_{\mathrm{pc}}}{V_{\mathrm{tot}}} \left(\frac{T_{\mathrm{tc}}}{T_{\mathrm{pc}}} - 1 \right)}, \tag{3.33}$$

$$n_{\mathrm{pc}} = \frac{n_0}{1 + \frac{V_{\mathrm{tc}}}{V_{\mathrm{tot}}} \left(\frac{T_{\mathrm{pc}}}{T_{\mathrm{tc}}} - 1 \right)}, \tag{3.34}$$

where T_{tc} (T_{pc}) and V_{tc} (V_{pc}) are the temperature and the volume of the target (pumping) chamber, respectively. n_0 is the number density at thermal equilibrium (shown in Table 3.6), and V_{tot} is the total volume of the cell. Here we neglect the transfer tube because the volume of the tube is much smaller than those of the two chambers.

The temperature of the target cell was measured at four positions with thermocouples; two each of them were attached to the target chamber and the pumping chamber. A Pt100 was also mounted inside the oven to monitor the temperature. Figure 3.10 shows the positions of these thermometers. However, the temperature distribution inside the cell must be very complicated because the pumping chamber is further heated by the absorption of the laser light.

There are several works that have determined the interior temperature of the cell. The first work was performed by Walter *et al.* [108]. They used Raman spectroscopy to measure the temperature via the rotational and vibrational spectra of N_2 gas. In this work, a temperature elevation of 95°C with respect to that of the outer cell wall was found when the deposited energy of laser power was 22 W in a cell which contains 8.4 bar ^{3}He gas. They also indicated that convection plays a important role for the heat transport in a cell. Recently, Singh *et al.* extracted the interior temperature from the comparison between NMR signals with and without laser light [91]. They found the temperature differences of 20–50°C between these conditions for high pressure cells ($\sim$ 8 amg). Normand *et al.* used neutron transmission to measure the ^{3}He number density corresponding to the temperature

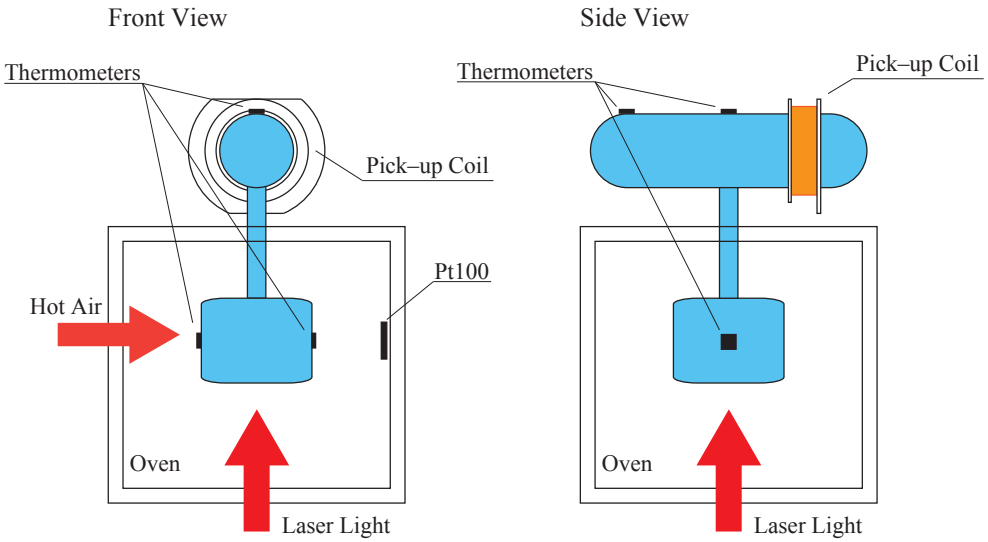

Figure 3.10: Positions of the thermocouples and the Pt100.

inside a cell [109]. They observed a 135°C temperature increase compared to the outer wall temperature of the cell which contains ^{3}He gas with a pressure of ~ 1 bar. They used a 200 W fiber-coupled laser for optical pumping.

In this study, we have estimated the temperature inside a cell using our target performance such as spin-up curves of ^{3}He polarization and ^{3}He spin relaxation rate. One can find a limit on the temperature because these parameters are closely related to the cell temperature. This estimation about the cell temperature will be described.

3.3.2 Polarization in a Double Cell

As shown in Eqs. (2.25) and (2.26), the rate equation and the time evolution of the ^{3}He polarization in the case of a single cell are given by,

$$\frac{dP_{^3\mathrm{He}}}{dt} = -(\gamma_{\mathrm{SE}} + \Gamma_{^3\mathrm{He}})P_{^3\mathrm{He}} + \gamma_{\mathrm{SE}}\overline{P}_{\mathrm{Rb}}, \tag{3.35}$$

$$P_{^3\mathrm{He}} = \overline{P}_{\mathrm{Rb}}\frac{\gamma_{\mathrm{SE}}}{\gamma_{\mathrm{SE}} + \Gamma_{^3\mathrm{He}}}\left[1 - e^{-(\gamma_{\mathrm{SE}}+\Gamma_{^3\mathrm{He}})t}\right]. \tag{3.36}$$

In the case of a double cell, ^{3}He nuclei are polarized in the pumping chamber and diffuses to the target chamber through the transfer tube. Therefore, the rate equation of the ^{3}He polarization in a double cell is described by the coupled differential equations [110, 111]:

$$\dot{P}_{\mathrm{pc}} = \gamma_{\mathrm{SE}}^{\mathrm{A}}(P_{\mathrm{A}} - P_{\mathrm{pc}}) - \Gamma_{\mathrm{pc}}P_{\mathrm{pc}} - d_{\mathrm{pc}}(P_{\mathrm{pc}} - P_{\mathrm{tc}}), \tag{3.37}$$

$$\dot{P}_{\mathrm{tc}} = -\Gamma_{\mathrm{tc}}P_{\mathrm{tc}} + d_{\mathrm{tc}}(P_{\mathrm{pc}} - P_{\mathrm{tc}}), \tag{3.38}$$

where $P_{\rm tc}$ ($P_{\rm pc}$) and $\Gamma_{\rm tc}$ ($\Gamma_{\rm pc}$) are the ^{3}He polarization and the spin relaxation rate in the target (pumping) chamber, respectively. $d_{\rm tc}$ ($d_{\rm pc}$) is the diffusion constant which shows the flux out of the target (pumping) chamber. These diffusion constants are related by,

$$f_{\rm tc} d_{\rm tc} = f_{\rm pc} d_{\rm pc}, \tag{3.39}$$

where $f_{\rm tc}$ ($f_{\rm pc}$) is the fraction of ^{3}He atoms in the target (pumping) chamber ($f_{\rm tc} + f_{\rm tc} = 1$). We neglect again the transfer tube because of the much smaller volume compared to that of the two chambers. Assuming the pressures of the two chambers are the same, the relation of $f_{\rm tc}$ and $f_{\rm pc}$ can be written as follows from the equation of state of the ideal gas,

$$f_{\rm tc} \frac{T_{\rm tc}}{V_{\rm tc}} = f_{\rm pc} \frac{T_{\rm pc}}{V_{\rm pc}}. \tag{3.40}$$

Thus, it can be expressed as,

$$f_{\rm tc} = 1 - f_{\rm pc} = \frac{V_{\rm tc}/V_{\rm pc}}{V_{\rm tc}/V_{\rm pc} + T_{\rm tc}/T_{\rm pc}}. \tag{3.41}$$

For sake of simplicity, the rate equations are rewritten as,

$$\dot{P}_{\rm pc} = a P_{\rm pc} + b P_{\rm tc} + B, \tag{3.42}$$

$$\dot{P}_{\rm tc} = c P_{\rm pc} + d P_{\rm tc}, \tag{3.43}$$

where

$$a = -(\gamma_{\rm SE}^{\rm A} + \Gamma_{\rm pc} + d_{\rm pc}), \tag{3.44}$$

$$b = d_{\rm pc}, \tag{3.45}$$

$$c = d_{\rm tc}, \tag{3.46}$$

$$d = -(\Gamma_{\rm tc} + d_{\rm tc}), \tag{3.47}$$

$$B = \gamma_{\rm SE}^{\rm A} P_{\rm A}. \tag{3.48}$$

From Eqs. (3.42) and (3.43), the rate equations can be written as second order differential equations as follows:

$$\ddot{P}_{\rm pc} - (a+d)\dot{P}_{\rm pc} - (bc - ad) P_{\rm pc} = -Bd, \tag{3.49}$$

$$\ddot{P}_{\rm tc} - (a+d)\dot{P}_{\rm tc} - (bc - ad) P_{\rm tc} = Bc. \tag{3.50}$$

The solutions of Eqs. (3.49) and (3.50) are given as the sum of the general solution and the particular solution;

$$P_{\rm pc}(t) = C_1 e^{-\Gamma_{\rm f} t} + C_2 e^{-\Gamma_{\rm s} t} + \frac{Bd}{bc-ad}, \tag{3.51}$$

$$P_{\rm tc}(t) = D_1 e^{-\Gamma_{\rm f} t} + D_2 e^{-\Gamma_{\rm s} t} - \frac{Bc}{bc-ad}, \tag{3.52}$$

where $\Gamma_{\rm f}$ and $\Gamma_{\rm s}$ are the eigenvalues of the general solution:

$$\Gamma_{\rm f} = -\frac{1}{2}(a+d)\left(1+\sqrt{1+\frac{4(bc-ad)}{(a+d)^2}}\right), \tag{3.53}$$

$$\Gamma_{\rm s} = -\frac{1}{2}(a+d)\left(1-\sqrt{1+\frac{4(bc-ad)}{(a+d)^2}}\right). \tag{3.54}$$

Finally, Eqs. (3.51) and (3.52) are expressed as,

$$P_{\rm pc}(t) = C_{\rm pc} e^{-\Gamma_{\rm f} t} + (P^0_{\rm pc} - P^\infty_{\rm pc} - C_{\rm pc}) e^{-\Gamma_{\rm s} t} + P^\infty_{\rm pc}, \tag{3.55}$$

$$P_{\rm tc}(t) = C_{\rm tc} e^{-\Gamma_{\rm f} t} + (P^0_{\rm tc} - P^\infty_{\rm tc} - C_{\rm tc}) e^{-\Gamma_{\rm s} t} + P^\infty_{\rm tc}, \tag{3.56}$$

where we defined the following relation:

$$C_{\rm pc} \equiv C_1 = P^0_{\rm pc} - P^\infty_{\rm pc} - C_2, \tag{3.57}$$

$$C_{\rm tc} \equiv D_1 = P^0_{\rm tc} - P^\infty_{\rm tc} - D_2, \tag{3.58}$$

$$P^0_{\rm pc} \equiv P_{\rm pc}(t=0), \tag{3.59}$$

$$P^0_{\rm tc} \equiv P_{\rm tc}(t=0), \tag{3.60}$$

$$P^\infty_{\rm pc} \equiv P_{\rm pc}(t=\infty) = \frac{Bd}{bc-ad}, \tag{3.61}$$

$$P^\infty_{\rm tc} \equiv P_{\rm tc}(t=\infty) = -\frac{Bc}{bc-ad}. \tag{3.62}$$

Therefore, the ratio of the ^{3}He polarization between the target and pumping chambers at $t \to \infty$ is given by,

$$\frac{P^\infty_{\rm tc}}{P^\infty_{\rm pc}} = -\frac{c}{d} = \frac{1}{1+\Gamma_{\rm tc}/d_{\rm tc}}. \tag{3.63}$$

3.3.3 Diffusion Constants

As described above, to evaluate the time variation of the ^{3}He polarization in a double cell, it is needed to consider diffusion terms. Here, we calculate the diffusion constant based on several assumptions.

In the presence of diffusion terms only, the rate equations of the ^{3}He polarization in a double cell are expressed as,

$$\dot{P}_{\rm pc} = -d_{\rm pc}(P_{\rm pc} - P_{\rm tc}), \tag{3.64}$$

$$\dot{P}_{\rm tc} = d_{\rm tc}(P_{\rm pc} - P_{\rm tc}). \tag{3.65}$$

In order to solve this equations, we consider the gas flux, which given by Fick's first law, due to a temperature gradient:

$$\boldsymbol{J} = -D(T)\nabla c, \tag{3.66}$$

where $\boldsymbol{J}$ is the flux, $D(T)$ is the diffusion coefficient and c is the concentration. In the one-dimensional case, Eq. (3.66) is expressed as,

$$J = -D(T)\frac{dc}{dz}. \tag{3.67}$$

Considering the flux of polarization transfers through the transfer tube, Eq. (3.67) is rewritten as [110],

$$J = -n(z)D(z)\frac{dP(z)}{dz}, \tag{3.68}$$

where $n(z)$ and $P(z)$ are the ^{3}He number density and the ^{3}He polarization. The diffusion coefficient for ^{3}He gas is given by [111],

$$D(z) = D_0\frac{n_0}{n(z)}\left(\frac{T(z)}{T_0}\right)^{m-1}, \tag{3.69}$$

where n is the number density of ^{3}He. D_0 is the empirical diffusion coefficient at a reference temperature T_0 and number density n_0. m is determined empirically. These values are listed in Table 3.7. Because the volume of the transfer tube is much smaller than that of the cell, we assume that the flux J is constant along the tube. Furthermore, we assume that the temperature gradient is linear along the tube. With these assumptions, the flux of polarization transfers is obtained from Eqs. (3.68) and (3.69):

$$J = -D_0 n_0 \frac{2-m}{T_0^{m-1}}\frac{T_{\rm pc} - T_{\rm tc}}{T_{\rm pc}^{2-m} - T_{\rm tc}^{2-m}}\frac{P_{\rm pc} - P_{\rm tc}}{L_{\rm tt}}, \tag{3.70}$$

where $L_{\rm tt}$ is the length of the transfer tube. Therefore, the diffusion constant which denotes the diffusion rate per atoms is given by,

$$d_{\rm pc} = \frac{A_{\rm tt}D_0}{V_{\rm pc}L_{\rm tt}}\frac{n_0}{n_{\rm pc}}\frac{2-m}{T_0^{m-1}}\frac{T_{\rm pc} - T_{\rm tc}}{T_{\rm pc}^{2-m} - T_{\rm tc}^{2-m}}, \tag{3.71}$$

$$d_{\rm tc} = \frac{A_{\rm tt}D_0}{V_{\rm tc}L_{\rm tt}}\frac{n_0}{n_{\rm tc}}\frac{2-m}{T_0^{m-1}}\frac{T_{\rm pc} - T_{\rm tc}}{T_{\rm pc}^{2-m} - T_{\rm tc}^{2-m}}, \tag{3.72}$$

Table 3.7: Diffusion coefficient parameters of ^{3}He gas [111].

D_0	2.789 cm^2/s
T_0	353.14 K
n_0	0.7733 amg
m	1.705

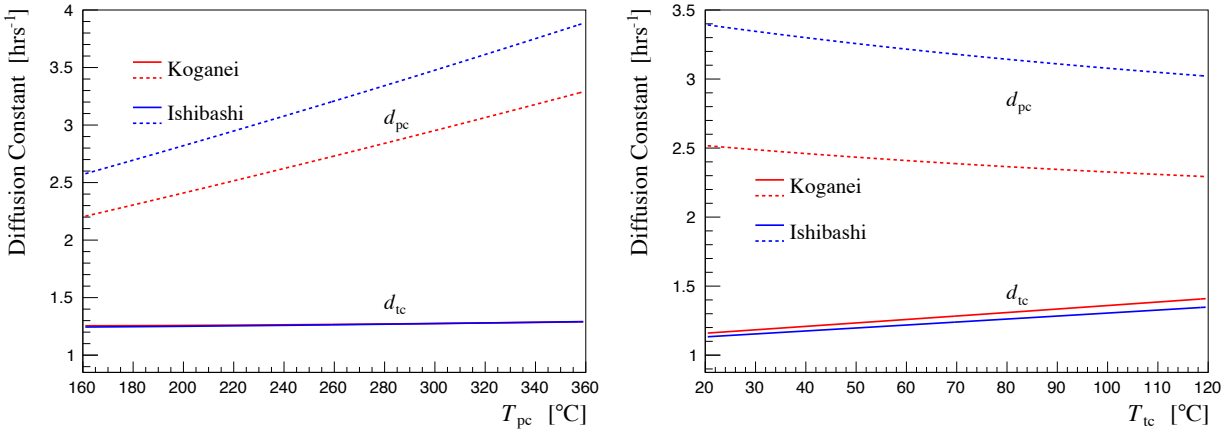

Figure 3.11: Calculated diffusion constants as functions of $T_{\rm pc}$ (left) and $T_{\rm tc}$ (right) for Koganei and Ishibashi cells. The solid (dotted) lines are the diffusion constant of the target (pumping) chamber. For the calculation as a function of $T_{\rm pc}$ ($T_{\rm tc}$), a constant value of $T_{\rm tc}$ ($T_{\rm pc}$) is used (see Table 3.8).

where $A_{\rm tt}$ is the cross-sectional area of the transfer tube.

Figure 3.11 shows the diffusion constants calculated by using Eqs. (3.71) and (3.72) as a function of temperature. The parameters used in this calculation are summarized in Table 3.8.

Table 3.8: Parameters for the calculation of the diffusion constant.

Parameters	Koganei	Ishibashi
$A_{\rm tt}$	0.503 cm^2	0.503cm^2
$L_{\rm tt}$	6.1 cm	6.0 cm
$T_{\rm tc}$ (const.)	60 °C	80 °C
$T_{\rm pc}$ (const.)	200 °C	250 °C

3.3.4 Numerical Simulation for the Evaluation of Cell Temperature

As discussed in the previous section, the gas temperature inside a cell being optically pumped with a high power laser is quite uncertain. The gas temperature directly affects several parameters in SEOP such as the density of alkali metal vapor, the spin exchange rate between alkali metal atoms and ^{3}He nuclei. The gas temperature can be estimated from the measured spin-up data because the time constant of spin-up curves depends on the spin exchange rate as shown in Eq. (2.26). In this section, we perform numerical simulations using the coupled differential equations, Eqs. (3.37) and (3.38), for estimating the gas temperatures inside a double cell.

First, we evaluate the ^{3}He spin relaxation rates in the target and pumping chambers from the measured relaxation data at room temperature ("cold relaxation"). In this condition, the rate equations of the ^{3}He polarization in a double cell are given by,

$$\dot{P}_{\rm pc} = -\Gamma_{\rm pc}P_{\rm pc} - d_{\rm pc}(P_{\rm pc} - P_{\rm tc}), \tag{3.73}$$

$$\dot{P}_{\rm tc} = -\Gamma_{\rm tc}P_{\rm tc} + d_{\rm tc}(P_{\rm pc} - P_{\rm tc}). \tag{3.74}$$

Additionally, the diffusion constants are obtained for $T_{\rm pc}/T_{\rm tc} \to 1$:

$$d_{\rm pc} = \frac{A_{\rm tt}D_0}{V_{\rm pc}L_{\rm tt}}\frac{n_0}{n_0^{\rm cell}}\frac{T_{\rm tc}^{m-1}}{T_0^{m-1}}, \tag{3.75}$$

$$d_{\rm tc} = \frac{A_{\rm tt}D_0}{V_{\rm tc}L_{\rm tt}}\frac{n_0}{n_0^{\rm cell}}\frac{T_{\rm tc}^{m-1}}{T_0^{m-1}}, \tag{3.76}$$

where $n_0^{\rm cell}$ is the ^{3}He number density of the cell at temperature equilibrium. We assume that the spin relaxation rates due to interactions with the glass walls are the same in any part inside the double cell. Moreover, the wall relaxation is dominant in the total spin relaxation rate as shown in Sec. 2.1.3. Thus, we assume that the spin relaxation rate in each chamber is related to the surface-to-volume ratio, S/V:

$$\Gamma_{\rm tc} = \frac{(S/V)_{\rm tc}}{(S/V)_{\rm pc}}\Gamma_{\rm pc}. \tag{3.77}$$

The surface-to-volume ratios of the Koganei and the Ishibashi cells are listed in Table 3.9.

Typical data of cold relaxation for the Koganei and the Ishibashi cells are shown in Fig. 3.12. When the pumping laser is turned off and the oven temperature is equal to room temperature, the ^{3}He polarization decays following an exponential function:

$$P_{^3{\rm He}}(t) = P_0 e^{-\Gamma_{^3{\rm He}}t}, \tag{3.78}$$

Table 3.9: Surface-to-volume ratios of each chamber.

Cell name	$(S/V)_{\rm tc}$	$(S/V)_{\rm pc}$
Koganei	1.42 ± 0.05	1.25 ± 0.06
Ishibashi	1.28 ± 0.01	1.26 ± 0.02

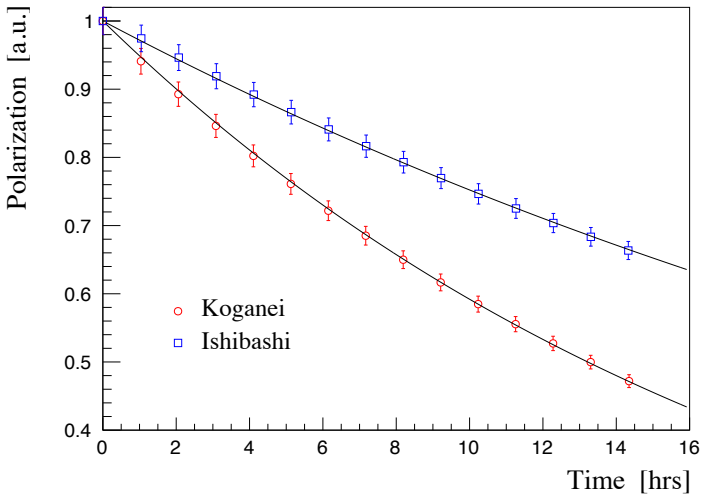

Figure 3.12: Typical data of cold relaxation for the Koganei and the Ishibashi cells. The solid lines are the fitted functions using Eq. (3.78).

where P_0 is the initial polarization at $t = 0$. As a result of fitting to the data, the time constants of cold relaxation for the Koganei and the Ishibashi cells are $1/\Gamma_{^3\rm He} = 19.1 \pm 0.2$ hrs and 35.1 ± 0.8 hrs, respectively.

Using Eqs. (3.73) and (3.74), we performed numerical simulations in the condition of cold relaxation. In this calculation, we applied depolarization due to the AFP-loss every 62 minutes (60 min. + the time for the AFP NMR measurement). We numerically determined $\Gamma_{\rm tc}$ and $\Gamma_{\rm pc}$ so as to reproduce the measured spin relaxation time. Figure 3.13 shows the results of the numerical calculations of cold relaxation. As a result, we obtained

$$\frac{1}{\Gamma_{\rm pc}} = 41 \pm 3 \ [\rm hrs]; \qquad \frac{1}{\Gamma_{\rm tc}} = 35 \pm 2 \ [\rm hrs], \tag{3.79}$$

for the Koganei cell and

$$\frac{1}{\Gamma_{\rm pc}} = 53 \pm 3 \ [\rm hrs]; \qquad \frac{1}{\Gamma_{\rm tc}} = 52 \pm 3 \ [\rm hrs], \tag{3.80}$$

for the Ishibashi cell, respectively. The estimated errors are mainly due to the uncertainties of the surface-to-volume ratios. However, these errors of the spin relaxation time

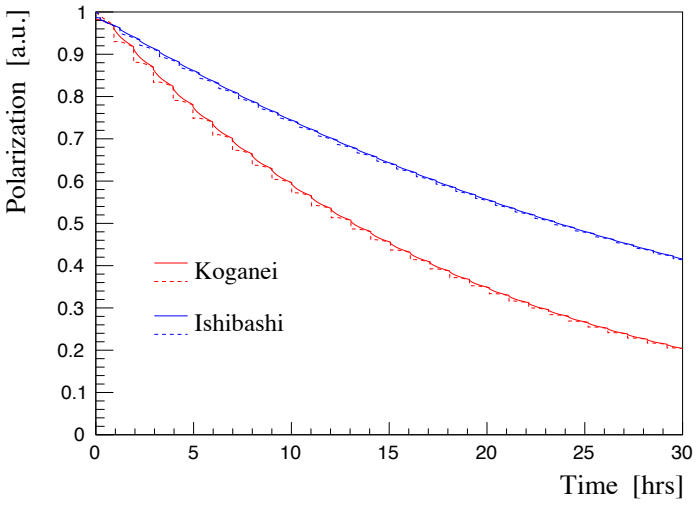

Figure 3.13: Numerical simulation of cold relaxation for the Koganei and the Ishibashi cells. The solid (dotted) lines denote the target (pumping) chamber.

correspond to only less than 1 °C for that of the gas temperature of the pumping chamber.

We also numerically determined the gas temperature of the pumping chamber so as to reproduce the measured values of spin-up time constants using Eqs. (3.37) and (3.38). In this simulation, the polarization of alkali metal atoms was fixed at 0.99. We assumed that the gas temperature of the target chamber is 60 °C (80 °C) for the Koganei (Ishibashi) cell based on the measured values on the surface of the chambers. Typical results of the numerical calculations are shown in Fig. 3.14. The time constants of the spin-up used as the boundary conditions are 12.1 hours for the Koganei cell and 9.25 hours for the Ishibashi cell in this calculation.

Figure 3.15 shows the temperature dependences of $T_{\rm pc}$ on $T_{\rm tc}$ obtained from the numerical simulations. Even if $T_{\rm tc}$ varies from 40 °C to 100 °C, $T_{\rm pc}$ decreases only about 5 °C. Therefore, $T_{\rm pc}$ is strongly limited by determining the time constant of the spin-up. In other words the time constant of the spin-up is very sensitive to the temperature inside the pumping chamber. Increasing the gas temperature in the pumping chamber by 5 °C, the time constant decreases by about 1 hour. Following the above results, in order to evaluate the number densities for the target cell, we used the $T_{\rm pc}$ value obtained from the numerical simulations. Meanwhile we adopted the average of the measured temperatures for the $T_{\rm tc}$ value. The uncertainties for $T_{\rm tc}$ and $T_{\rm pc}$ are estimated to be 5 °C from the fluctuations of the monitored temperatures by the thermocouples during the operation. These errors

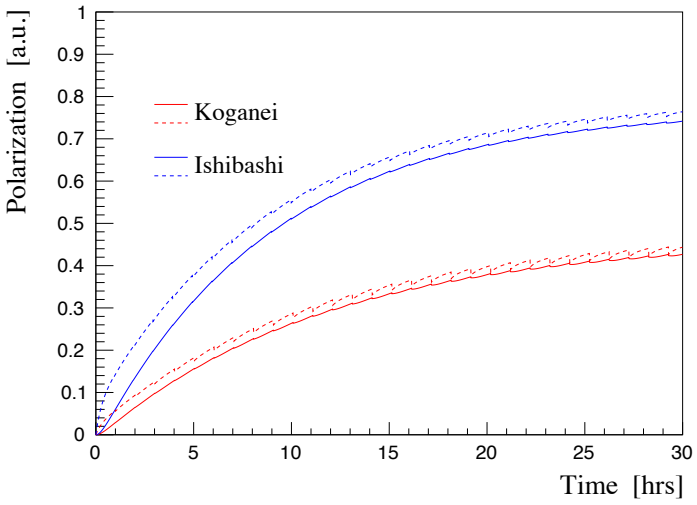

Figure 3.14: Numerical simulation of spin up for the Koganei and the Ishibashi cells. For description of lines see Fig. 3.13.

of the temperature contribute no more than 0.5 % to the number density of the target chamber and 1.5 % to that of the pumping chamber, respectively.

3.3.5 Target Conditions

In this study, we have performed the scattering experiments for the polarized ^{3}He target at CYRIC in December 2016, June 2017 and June 2018, and at RCNP in November 2018. The summary of target performance for these experiments is shown in Table 3.10. The target condition of the neutron transmission experiment performed in July 2019 at RANS (RIKEN Accelerator-driven compact Neutron Sources) is also shown.

We perform the calibration of the AFP-NMR at each experiment by the EPR measurement. The ^{3}He number densities are corrected by using the estimated $T_{\rm tc}$ and $T_{\rm pc}$ as shown in Table 3.10. The NMR signal of the pumping chamber is calibrated by the EPR method directly. The equilibrium ^{3}He polarization of the target chamber is extracted from that of the pumping chamber by using Eq. (3.63), and the NMR signal of the target chamber is calibrated accordingly. Calibration results of the AFP-NMR at the pumping chamber are shown in Fig. 3.16. The relations between the NMR signal and the ^{3}He polarization of the pumping chamber were determined by a linear fit for the Koganei cell as,

$$P_{\rm pc} = (0.379 \pm 0.009) \times 10^{-3} \cdot V_{\rm NMR}^{\rm pc}, \tag{3.81}$$

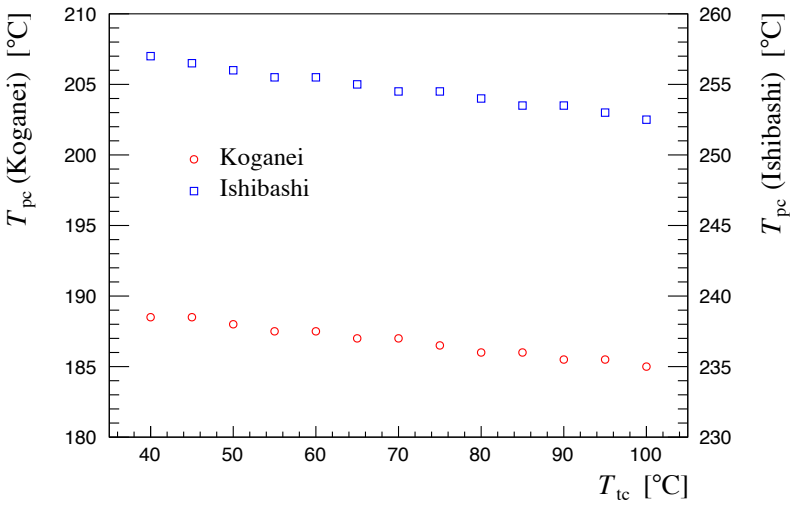

Figure 3.15: Gas temperature of the pumping chamber T_{pc} as a function of T_{tc} for the Koganei and the Ishibashi cells.

Table 3.10: Target conditions for the scattering experiments at CYRIC and RCNP. The target conditions of the measurement of the ^{3}He polarization at RANS is also shown. Kog (Ishi) denotes the Koganei (Ishibashi) cell. P_{laser} is the output power of a laser entering the cell. $P^{\infty}_{^3He}$ is the equilibrium ^{3}He polarization in the target chamber. T_{tc} and T_{pc} are the measured temperature at the target and pumping chambers. T_{calc} is the calculated temperature of the pumping chamber obtained from the numerical simulation. D = [K]/[Rb] is the vapor density ratio at operating temperature. τ_{up} and $\Gamma^{-1}_{^3He}$ are the measured time constants of the spin-up and cold relaxation. Γ_{tc} and Γ_{pc} are the spin relaxation rates at each chambers obtained from the numerical simulation. An asterisk indicates nominal value for T_{tc}. The numbers in parentheses represent errors.

Exp.	Cell	P_{laser} [W]	$P^{\infty}_{^3He}$	T_{tc} [°C]	T_{pc} [°C]	T_{calc} [°C]	D	τ_{up} [hrs]	$\Gamma^{-1}_{^3He}$ [hrs]	Γ^{-1}_{tc} [hrs]	Γ^{-1}_{pc} [hrs]
CYRIC, Dec. '16	Kog	48	0.31(2)	60*	200	211	0	7.67(14)	21.7(1)	47	53
CYRIC, Jun. '17	Kog	26	0.24(2)	60*	178	185	0	12.8(7)	19.5(1)	37	42
CYRIC, Jun. '18	Ishi	46	0.40(3)	70*	230	242	3.57(3)	13.0(1)	39.2(1)	63	64
RCNP, Nov. '18	Ishi	49	0.37(2)	65	259	266	3.88(4)	6.34(9)	24.4(4)	32	32
RANS, Jul. '19	Kog	20	0.23(2)	52	183	188	0	12.1(1)	19.1(2)	35	41
	Ishi	24	0.33(2)	73	241	254	3.73(3)	9.25(7)	35.1(8)	52	53

Table 3.11: Operating conditions at the AFP-NMR calibrations for the Koganei and Ishibashi cells.

	Koganei	Ishibashi
$T_{\rm tc}$	58 °C	76 °C
$T_{\rm pc}$	218 °C	257 °C
$T_{\rm calc}$	212 °C	254 °C
$\tau_{\rm up}$	7.23(3) hrs	9.10(40) hrs

and for the Ishibashi cell as,

$$P_{\rm pc} = (0.299 \pm 0.007) \times 10^{-3} \cdot V_{\rm NMR}^{\rm pc}, \tag{3.82}$$

where $V_{\rm NMR}^{\rm pc}$ is the NMR signal voltage of the pumping chamber in μV. The operating conditions in the AFP-NMR calibrations are listed in Table 3.11. Using the calibration results of the AFP-NMR at the pumping chamber and Eq. (3.63), the equilibrium ^{3}He polarization of the target chamber was evaluated. Comparing the NMR signal voltage of the target chamber, we obtained the relation between the NMR signal and the ^{3}He polarization of the target chamber for the Koganei cell as,

$$P_{\rm tc} = (1.20 \pm 0.05) \times 10^{-3} \cdot V_{\rm NMR}^{\rm tc}, \tag{3.83}$$

and for the Ishibashi cell as,

$$P_{\rm tc} = (1.09 \pm 0.03) \times 10^{-3} \cdot V_{\rm NMR}^{\rm tc}, \tag{3.84}$$

where $V_{\rm NMR}^{\rm tc}$ is the NMR signal voltage of the target chamber in mV. However, in the scattering experiment at RCNP, the gain of the pick-up coil was different because the coil has been placed far from the target chamber to measure the scattered particles at a certain angle. Therefore, we independently calibrated the NMR signal voltage following the above numerical simulations. The obtained relation between $V_{\rm NMR}^{\rm tc}$ and $P_{\rm tc}$ for the experiment at RCNP were given as,

$$P_{\rm tc} = (5.68 \pm 0.34) \times 10^{-3} \cdot V_{\rm NMR}^{\rm tc}. \tag{3.85}$$

The ^{3}He polarizations evaluated from the NMR measurements and the conversion coefficients in Eqs. (3.83) and (3.84) need to be corrected for the ^{3}He number density differences (in the target chambers due to the temperature variation in the experiments). However, this correction is at most about 1 %. Therefore, it was ignored in this work.

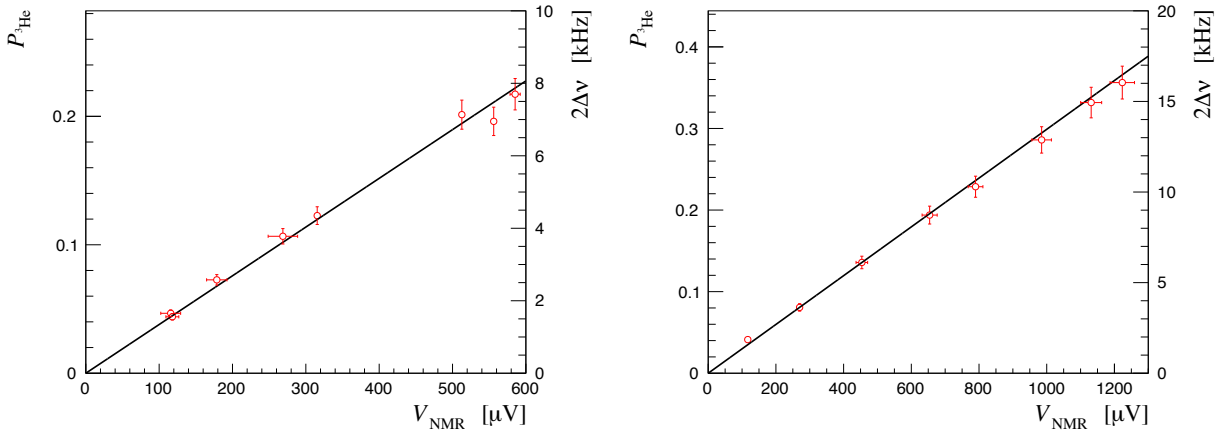

Figure 3.16: Relations between the NMR signal and the ^{3}He polarization by the EPR measurement of the pumping chamber for the Koganei (left) and Ishibashi (right) cells. The solid lines show linear fits.

Chapter 4

Measurement of the Absolute ^{3}He Polarization at RANS

We performed a direct measurement of the absolute ^{3}He polarization of the target chamber by a breakthrough technique based on neutron transmission. This experiment was carried out at RANS (RIKEN Accelerator-driven compact Neutron Sources), RIKEN. In this chapter, we describe principles of the measurement and the detail of the experiment.

4.1 Outline of the Experiment

4.1.1 Principle of Measurement

Neutron transmission for polarized ^{3}He nuclei T_n can be written as,

$$T_n = e^{-o}\cosh(P_{\rm He}o), \tag{4.1}$$

$$o = \sigma_{\rm abs} n_{\rm He} d, \tag{4.2}$$

where o is the opacity, $\sigma_{\rm abs}$ is the spin-averaged neutron absorption cross section of ^{3}He, $n_{\rm He}$ is the ^{3}He number density, d is the thickness of the ^{3}He gas and $P_{\rm He}$ is the ^{3}He polarization, respectively. Here, we ignore the elastic scattering cross section, which is 3 barn [112] and enough small compared to $\sigma_{\rm abs}$ at energies of our interest. $\sigma_{\rm abs}$ was measured by Keith *et al.* at low energies (0.1–400 eV) [113];

$$\sigma_{\rm abs} = (849.77 \pm 0.14_{\rm (sta)} \pm 1.02_{\rm (sys)})E_n^{-1/2} - (1.25 \pm 0.00_{\rm (sta)}{}^{+0.01}_{-0.05({\rm sys})}) \text{ [barn]}, \tag{4.3}$$

where E_n is the neutron energy in eV. Therefore, the ^{3}He polarization is calculated as,

$$P_{\rm He} = -\frac{1}{\ln T_{n,0}} \cosh^{-1}\left(\frac{T_n}{T_{n,0}}\right), \tag{4.4}$$

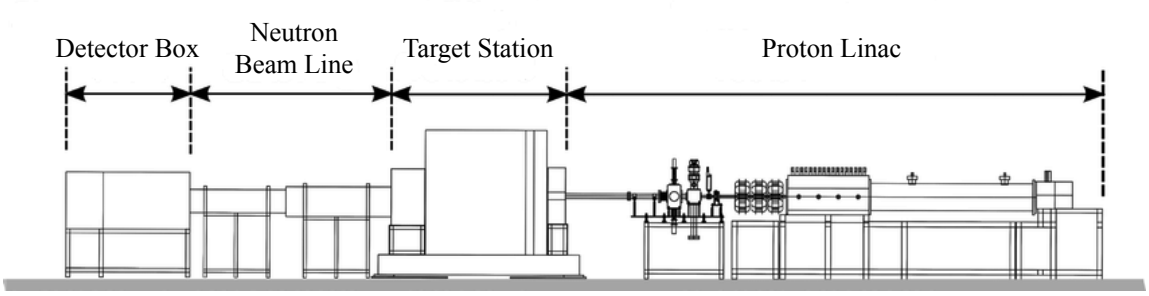

Figure 4.1: Schematic view of RANS [115]. A total length is about 15 m.

where $T_{n,0}$ is the neutron transmission for the unpolarized ^{3}He gas. Thus, the ^{3}He polarization of the target chamber can be obtained from the ratio of T_n to $T_{n,0}$. In addition, the ^{3}He number density in the target chamber can be deduced from the measurement of $T_{n,0}$ as,

$$n_{\mathrm{He}} = -\frac{1}{\sigma_{\mathrm{abs}} d} \ln T_{n,0}. \tag{4.5}$$

4.1.2 RIKEN Accelerator-Driven Compact Neutron Sources

RANS is a compact accelerator-based neutron source build at RIKEN for neutron scattering measurements and other applications [114]. A schematic view of RANS is shown in Fig. 4.1. It consists of a proton linear accelerator, a target station for producing neutron beams, a neutron beam line and a detector box. Protons are extracted in an ion source and accelerated by the linac up to 7 MeV. Proton beams are injected to a Be target with a thickness of 0.3 mm placed inside the target station. Neutrons are produced via the charge-exchange reaction: Be(p, n), and are moderated in a polyethylene moderator with a thickness of 40 mm. Thus, the thermal neutrons ($E_n \sim 0.05$ eV) can be extracted from the target station. The energy distribution of the neutrons has peaks around 1.5 MeV and 50 meV [114]. The neutron beams from the target station are transported to the detector box through the neutron beam line surrounded by borated polyethylene. The detector box is shielded with borated polyethylene and B_4C sheets for reducing background neutrons. Table 4.1 shows the specifications of RANS [114].

Table 4.1: Specifications of the proton linac, the target and the moderator at RANS [114].

Proton energy	7 MeV
Current	20–100 μA
Beam pulse repetition	20–200 Hz
Beam pulse width	8–200 μsec
Target	Be ($\phi = 50$ mm)
Target thickness	0.3 mm
Moderator	Polyethylene ($\phi = 180$ mm)
Moderator thickness	40 mm

4.2 Experimental Setup

Figure 4.2 shows the experimental setup of the neutron transmission measurement. The polarized ^{3}He target was installed downstream of the neutron beam line. We also installed B_4C slit collimators before and after the polarized ^{3}He target as well as the neutron beam line so that the neutron beams passed only through the center of the target chamber. B_4C is commonly used for thermal neutron shielding because boron has a large absorption cross section for neutrons. The B_4C slit collimator consists of four B_4C plates with a thickness of 5 mm mounted on a finely movable stage. The collimation size of these B_4C slit collimators was set to 10×10 mm^2 in this experiment. The neutron detector was covered by a B_4C sheet except for neutron beam to reduce background neutrons. The distance from the moderator surface to the detector was 4.56 m. During the experiment we monitored the average current of the proton pulses by measuring the voltage induced by the proton pulses using a 50 Ω resistance connected to the Be target.

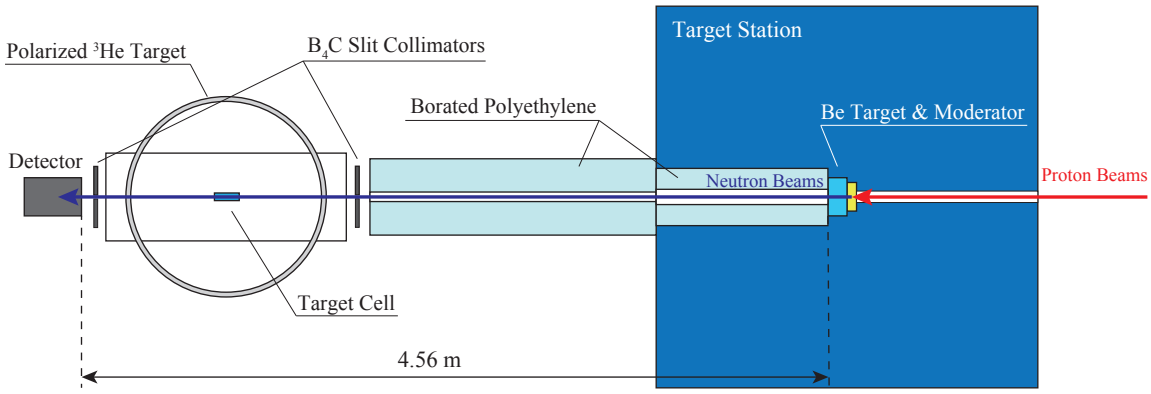

Figure 4.2: Experimental setup of the neutron transmission measurement (top view).

Table 4.2: Specifications of the neutron detector.

Scintillator	ZnS(Ag)/^{6}LiF
Scintillator thickness	0.25 mm
Effective area	$\phi = 90$ mm
Efficiency	30 % (for cold neutron)
Spatial resolution	0.8 mm (FWHM)

The neutron detector consists of a ZnS(Ag)/^{6}LiF scintillator optically coupled with a position sensitive photo multiplier tube (RPMT). A ZnS(Ag)/^{6}LiF scintillator has a large light yield for thermal neutrons. This RPMT (R3292, Hamamatsu Photonics K.K.) has a 12-stage mesh dynode and an anode wire structure crossing in the x-axis and y-axis directions. Output currents from each anode wire are divided into two signals by resistors. The position of detected neutrons can be obtained from the ratio of these currents [116]. Specifications of the neutron detector are shown in Table 4.2. The neutron energy was determined by the time-of-flight (ToF) between a signal from the proton linac and the event trigger of the detector.

We performed the neutron transmission measurements under several experimental conditions as follows:

(A) Neutron beam intensity measurement

(B) Transmission measurement for a blank cell

(C) Transmission measurement for an unpolarized target cell at room temperature

(D) Transmission measurement for an unpolarized target cell under the operating condition

(E) Transmission measurement for a polarized target cell under the operating condition

(F) Background measurement

The measurements (A) and (B) were used for estimating the neutron transmission for GE180 glass of the cell. The ^{3}He number density of the cell at temperature equilibrium was obtained by the measurement (C). The measurement (D) was used to determine the ^{3}He polarization using Eq. (4.1). This measurement was also used for comparison between the experimental results and the estimation of the gas temperature inside the cell by the

Table 4.3: Proton beam conditions at the RANS measurement.

Pulse current	20 μA
Pulse repetition rate	125 Hz
Pulse width	20 μsec

numerical simulation described in Chapter 3. During this measurement, we performed the "bad" AFP spin flip at short periods (a few minutes) to maintain unpolarization. Sweeping the static magnetic field while applying the RF field which has very small amplitude, ^{3}He nuclei are imperfectly spin flipped by AFP-NMR with this bad AFP conditions. The transmission measurement (E) was continued for three days after the start-up of the optical pumping until the ^{3}He polarization was saturated since the polarization build-up time was 10 hrs. For the measurement (F), we placed a B_4C mask with thickness of 13 mm between the target cell and the neutron detector to shut off thermal neutrons. The experimental conditions are listed in Table 4.3.

4.3 Data Analysis

The neutron transmission for the ^{3}He gas in a target cell can be rewritten as,

$$T_n = \frac{N_{\rm He} - N_{\rm BG}}{N_{\rm Blank} - N_{\rm BG}}, \tag{4.6}$$

where N is the number of detected neutrons. The subscripts He, Blank and BG denote the measurements for a ^{3}He cell, a blank cell and the background, respectively. Note that $N_{\rm He}$, $N_{\rm Blank}$ and $N_{\rm BG}$ are each normalized by the proton beam intensity.

Figure 4.3 shows typical two-dimensional images of the detected neutron positions for each measurement. The neutrons passed through the B_4C slit collimator of an area of 10×10 mm^2 can be clearly seen. We selected neutrons with positions in a ϕ9 mm circle as shown in Fig. 4.3. Figure 4.4 shows typical ToF spectra of detected neutrons. The slow neutrons are completely absorbed by the ^{3}He cell, and the very fast ones penetrate through the B_4C slit collimators. Thus, we also roughly selected neutrons in the range of $E_n = 10$ meV (ToF ~ 3300 μsec) to 600 meV (ToF ~ 430 μsec) in order to eliminate these neutrons.

Figure 4.5 shows projections of the neutron positions onto the x-axis. The neutrons are selected by the ToF cut, and the counts are normalized by the proton intensities. It is

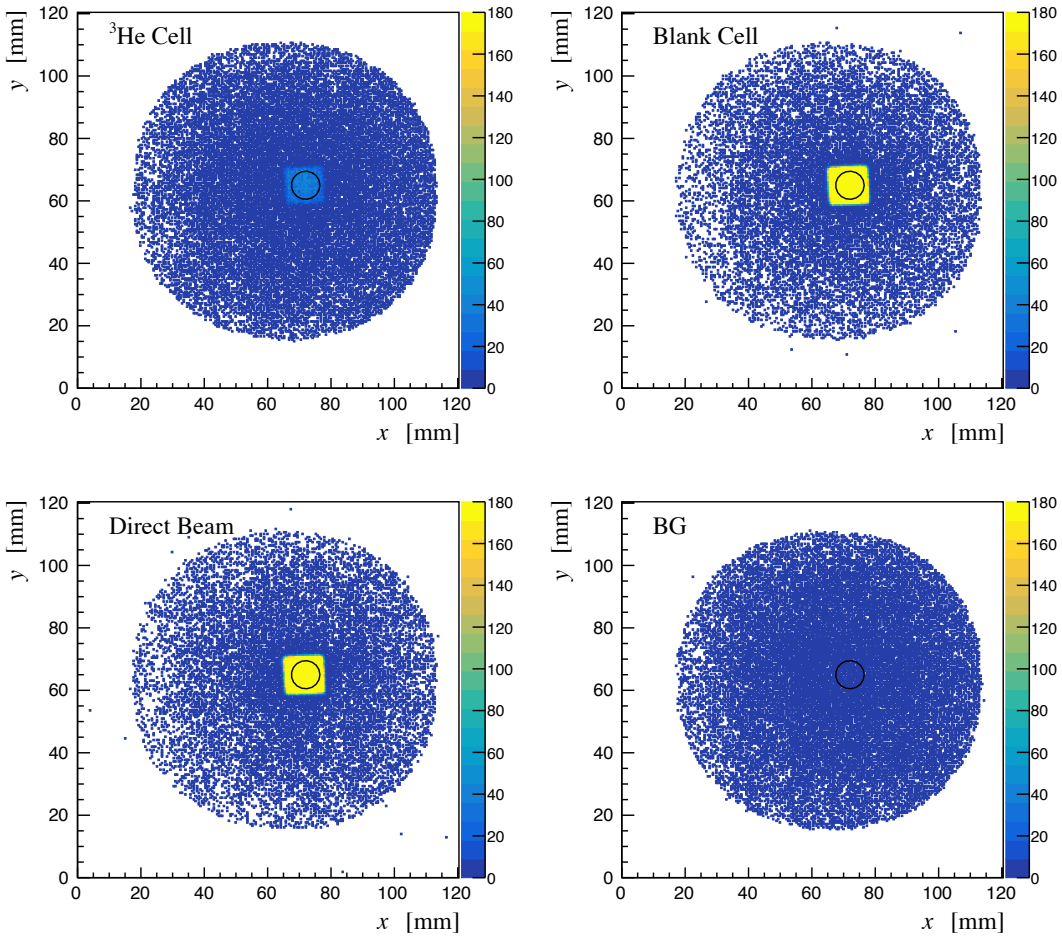

Figure 4.3: Typical two-dimensional images of the detected neutron positions of the transmission measurement for the ^{3}He cell (upper left) and the blank cell (upper right), the direct beam measurement (bottom left) and the background measurement (bottom right). The neutrons within the solid circles, diameters of 9 mm, are used for the analysis.

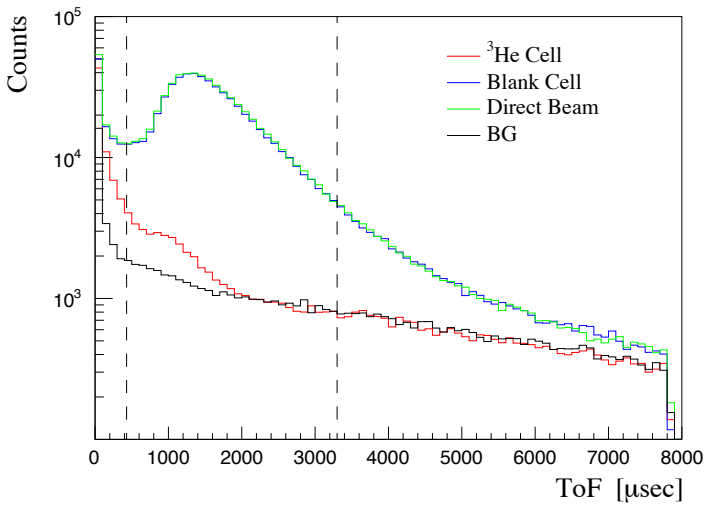

Figure 4.4: Typical time-of-flight (ToF) spectra for the transmission measurement with the ^{3}He cell (red) and the blank cell (blue), the direct beam measurement (green) and the background measurement (black). The number of counts are each normalized by the proton intensity. The vertical dashed lines are the roughly cuts to eliminate the slow and fast neutrons.

clearly seen that the neutrons passed through the ^{3}He cell decrease due to the absorption by ^{3}He gas.

4.4 Experimental Results

4.4.1 ^{3}He Number Densities

We show the experimental results of the ^{3}He number densities for the Koganei and the Ishibashi cells in Fig. 4.6 with statistical errors. Figure 4.6 shows the evaluated ^{3}He number densities to the neutron energy for the conditions where both laser and oven are on and off. It can be seen that the ^{3}He number densities of the target chamber increase by heating with the laser and the oven.

We estimated the systematic error of the ^{3}He number density from three uncertainties: the neutron energy, the inner length of the cell and the proton beam intensity. Using Eq. (4.5), the systematic error is given by,

$$\left(\frac{\Delta n_{\mathrm{He}}}{n_{\mathrm{He}}}\right)_{\mathrm{sys}} = \sqrt{\left(\frac{\Delta\sigma_{\mathrm{abs}}}{\sigma_{\mathrm{abs}}}\right)^2 + \left(\frac{\Delta d}{d}\right)^2 + \left(\frac{1}{\ln T_{\mathrm{n},0}}\frac{\Delta T_{\mathrm{n},0}}{T_{\mathrm{n},0}}\right)^2}. \tag{4.7}$$

The uncertainties of the inner length of the target chamber were estimated as 0.6 % for the

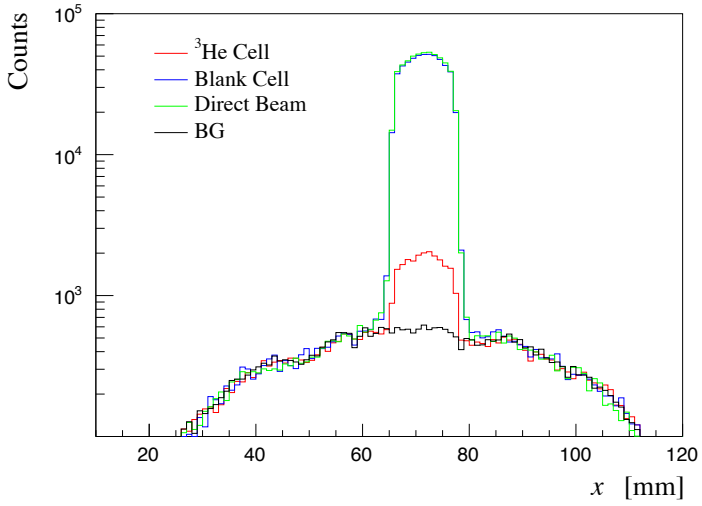

Figure 4.5: Projections of the detected neutron positions onto the x-axis for each measurement. The neutrons are selected by the ToF cut, and the counts are normalized by the proton intensities. For description of lines, see Fig. 4.4.

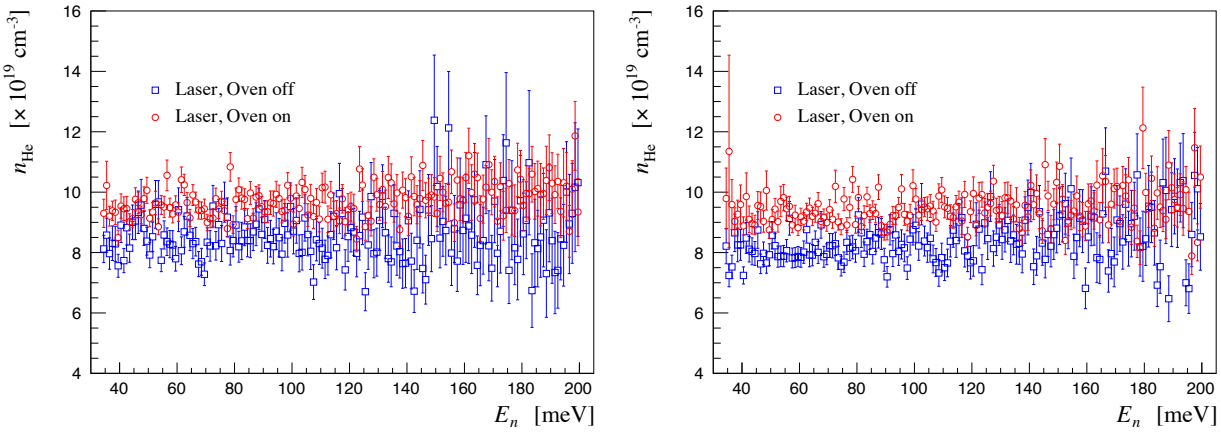

Figure 4.6: Evaluated ^{3}He number densities for the Koganei cell (left) and the Ishibashi cell (right). The blue (red) dots represents for both laser and oven off (on).

Koganei cell and 1.1 % for the Ishibashi cell from the measurement errors. We assumed that thermal neutrons are sufficiently slow and can be treated non-relativistically; thus, the neutron energy is written by,

$$E_n = \frac{1}{2} m_n \left(\frac{L}{t} \right)^2 , \tag{4.8}$$

where m_n is the neutron mass, L is the distance from the moderator surface to the neutron detector and t is the ToF. As shown in Eq. (4.3), the neutron absorption cross section of ^{3}He $\sigma_{\rm abs}$ depends on the E_n. Therefore, the determination accuracy of E_n affects the error on $\sigma_{\rm abs}$. The error on the neutron absorption cross section due to the neutron energy uncertainty is given by,

$$\frac{\Delta\sigma_{\rm abs}}{\sigma_{\rm abs}} = \sqrt{\left(\frac{\Delta L}{L} \right)^2 + \left(\frac{\Delta t}{t} \right)^2}. \tag{4.9}$$

We measured the distance L with an accuracy of 0.2 %. The uncertainty of the ToF was taken from the beam pulse width and the moderation time of neutrons. We adopt the uncertainty of the ToF due to the beam pulse width as ± 10 μsec since this width was 20 μsec in this experiment. The moderation time width was estimated to be 30 μsec for 10–20 meV neutrons by Ikeda *et al.* [114]. The neutron moderation time gets shorter at higher energies, but we take ± 15 μsec as a worse case here. Thus, the uncertainty of the ToF become ± 25 μsec as the sum of these uncertainties. In this work, we selected neutrons in an energy range of 35 to 100 meV to evaluate the ^{3}He number density with a sufficient statistical accuracy. We take this systematic error to be 2.4 % at the maximum because the ToF is 1040 μsec at 100 meV.

The systematic error of the neutron transmission $T_{n,0}$ comes from the uncertainty of the proton beam intensity. Using Eq. (4.6), it is given by,

$$\frac{\Delta T_{\rm n,0}}{T_{\rm n,0}} = \frac{\Delta\alpha}{\alpha} \sqrt{\left(\frac{N_{\rm Blank}}{N_{\rm Blank} - N_{\rm BG}} \right)^2 + \left(\frac{N_{\rm BG}(N_{\rm He} - N_{\rm Blank})}{(N_{\rm He} - N_{\rm BG})(N_{\rm Blank} - N_{\rm BG})} \right)^2}, \tag{4.10}$$

$$\frac{\Delta N_{\rm Blank}}{N_{\rm Blank}} = \frac{\Delta N_{\rm BG}}{N_{\rm BG}} \equiv \frac{\Delta\alpha}{\alpha}, \tag{4.11}$$

where α is the normalization factor from the proton intensity. The error of the normalization factor was evaluated from the deviation of the average pulse current for each run because the measurements were performed with the same beam conditions throughout the experiment. The error was quite small (less than 0.3 %) for the ^{3}He number density. The systematic errors on the evaluation of the ^{3}He number density are listed in Table 4.4.

Table 4.4: Systematic errors of the ^{3}He number densities for the Koganei and the Ishibashi cells.

Source	Koganei	Ishibashi
Inner length of the cell	0.6 %	1.1 %
Beam intensity	$\leq$ 0.1 %	0.3 %
ToF	2.2 %	2.2 %
Total	2.2 %	2.4 %

The ^{3}He number density at temperature equilibrium was obtained for the Koganei cell as,

$$n_{\mathrm{He}} = (8.37 \pm 0.07_{(\mathrm{sta})} \pm 0.18_{(\mathrm{sys})}) \times 10^{19} \quad [\mathrm{cm}^{-3}], \tag{4.12}$$

and for the Ishibashi cell as,

$$n_{\mathrm{He}} = (8.02 \pm 0.05_{(\mathrm{sta})} \pm 0.19_{(\mathrm{sys})}) \times 10^{19} \quad [\mathrm{cm}^{-3}]. \tag{4.13}$$

The statistical error was 0.8 % for the Koganei cell and 0.6 % for the Ishibashi cell, respectively. These results are in good agreements with the ^{3}He number densities obtained from the previous work shown in Table 3.6 within 2 %. We also evaluated the ^{3}He number density of the target chamber under the operating condition in the same manner for the Koganei cell as,

$$n_{\mathrm{tc}} = (9.44 \pm 0.04_{(\mathrm{sta})} \pm 0.22_{(\mathrm{sys})}) \times 10^{19} \quad [\mathrm{cm}^{-3}], \tag{4.14}$$

and for the Ishibashi cell as,

$$n_{\mathrm{tc}} = (9.20 \pm 0.04_{(\mathrm{sta})} \pm 0.22_{(\mathrm{sys})}) \times 10^{19} \quad [\mathrm{cm}^{-3}], \tag{4.15}$$

with the statistical error of 0.4 %. Using Eq. (3.33) and the temperatures inside the cell estimated from the numerical simulations listed in Table 3.10, the ^{3}He number density under the operating condition was calculated for the Koganei cell as,

$$n_{\mathrm{tc}} = (9.56 \pm 0.11) \times 10^{19} \quad [\mathrm{cm}^{-3}], \tag{4.16}$$

and for the Ishibashi cell as,

$$n_{\mathrm{tc}} = (9.20 \pm 0.07) \times 10^{19} \quad [\mathrm{cm}^{-3}], \tag{4.17}$$

where we used the measured ^{3}He number densities at temperature equilibrium. These results agree well with the numbers by the neutron transmission measurement, and this fact firmly supports the numerical simulations in Section 3.3.

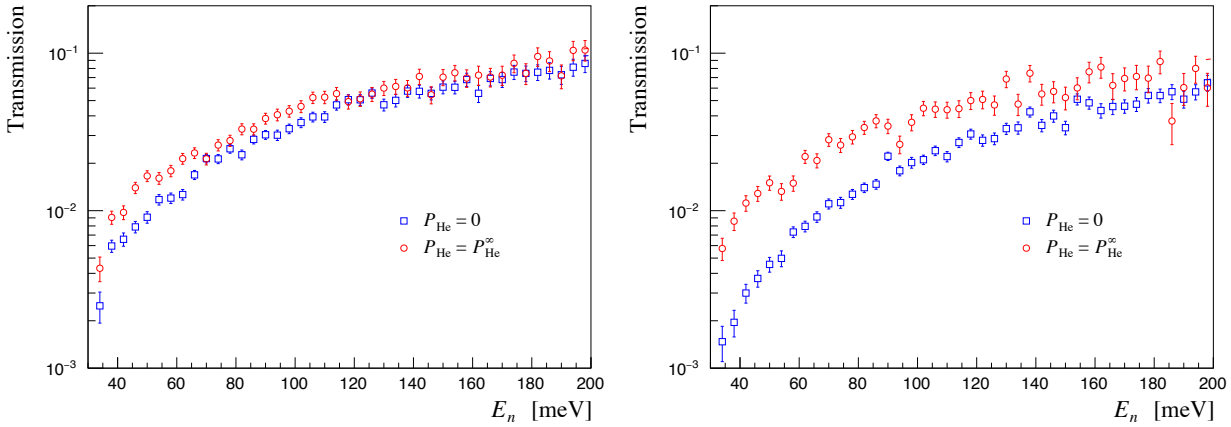

Figure 4.7: Energy dependence of the neutron transmission for the Koganei cell (left) and the Ishibashi cell (right). The blue squares (red circles) show the data using the unpolarized (polarized) target cell.

4.4.2 Target Polarization

Figure 4.7 shows the results of the absolute ^{3}He polarization measurement for the Koganei and the Ishibashi cells. Energy dependence of the neutron transmissions is presented in the blue squares for the unpolarized ^{3}He gas in the target chamber and the red circles for the saturated polarized ^{3}He gas.

We estimated systematic errors from the uncertainty of the proton beam intensity similarly in the analysis of the ^{3}He number density. Using Eq. (4.4), the error of the ^{3}He polarization is given by,

$$\left(\frac{\Delta P_{\mathrm{He}}}{P_{\mathrm{He}}}\right)^2 = \left(\frac{1}{\ln T_{n,0}} + \frac{1}{\cosh^{-1}(T_n/T_{n,0})}\frac{1}{\sqrt{(T_n/T_{n,0})^2-1}}\frac{T_n}{T_{n,0}}\right)^2 \left(\frac{\Delta T_{n,0}}{T_{n,0}}\right)^2 + \left(\frac{1}{\cosh^{-1}(T_n/T_{n,0})}\frac{1}{\sqrt{(T_n/T_{n,0})^2-1}}\frac{T_n}{T_{n,0}}\right)^2 \left(\frac{\Delta T_n}{T_n}\right)^2. \tag{4.18}$$

The systematic errors of the ^{3}He polarization due to the uncertainty of the proton intensity are listed in Table 4.5.

Using Eq. (4.4) and taking the weighted average value in the energy range of 35–200 meV, the absolute ^{3}He polarization of the target chamber was obtained for the Koganei cell as,

$$P_{\mathrm{tc}} = 0.220 \pm 0.008_{(\mathrm{sta})} \pm 0.004_{(\mathrm{sys})}, \tag{4.19}$$

Table 4.5: Systematic errors of the ^{3}He polarization for the Koganei and the Ishibashi cells.

	Koganei	Ishibashi
$T_{n,0}$	0.8 %	0.4 %
T_n	1.6 %	0.2 %
Total	1.8 %	0.5 %

with the statistical error of 3.7 %, and for the Ishibashi cell as,

$$P_{\rm tc} = 0.331 \pm 0.006_{\rm (sta)} \pm 0.002_{\rm (sys)}, \tag{4.20}$$

with the statistical error of 1.8 %.

We have made an absolute calibration for the NMR using the results obtained above. Taking the NMR signals before and after the neutron transmission measurements, the calibration coefficients, the ratios of the NMR signal height to the absolute ^{3}He polarization, were determined for the Koganei cell as,

$$P_{\rm tc} = (1.16 \pm 0.05) \times 10^{-3} \cdot V_{\rm NMR}^{\rm tc}, \tag{4.21}$$

and for the Ishibashi cell as,

$$P_{\rm tc} = (1.10 \pm 0.03) \times 10^{-3} \cdot V_{\rm NMR}^{\rm tc}, \tag{4.22}$$

where the statistical errors were only shown. These results agree well with the calibration results of the off-line measurement using the numerical simulations.

Chapter 5

Measurement of ^{3}He Analyzing Power

We performed the measurement of ^{3}He analyzing powers for p–^{3}He elastic scattering at 70 and 100 MeV. The experiments at 70 MeV were conducted three times, December 2016, June 2017 and June 2018, at Cyclotron and Radioisotope Center (CYRIC) in Tohoku University. The experiment at 100 MeV was carried out at Research Center for Nuclear Physics (RCNP), Osaka University in November 2018. In this chapter we describe the procedures of the experiments and the data analysis.

5.1 Overview of Experiment at CYRIC

The experiments at 70 MeV were performed by using the proton beam at CYRIC. In Fig. 5.1 shows a schematic view of CYRIC. Proton beams were provided by an electron cyclotron resonance (ECR) ion source, and then were accelerated up to 70 MeV by an azimuthally varying field (AVF) cyclotron. The beams were transported to the 4th target room (TR4) and bombarded the polarized ^{3}He target which was installed along the 41 beam line course. The experimental setup around the polarized ^{3}He target is shown in Fig. 5.2. Charge collection of the beam was performed by using a Faraday cup (FC) placed downstream of the target. Relative values of the beam intensities were monitored by a beam line monitor installed in the vacuum chamber upstream of the polarized ^{3}He target.

The polarized ^{3}He target was placed in the atmosphere as shown in Fig. 5.2. An aluminum-made beam duct coupled with an aluminum-made flange was connected to the vacuum chamber. The vacuum was separated Kapton film with thickness of 50 μm prior to the ^{3}He target. The vacuum chamber was evacuated by a rotary pump and a turbo

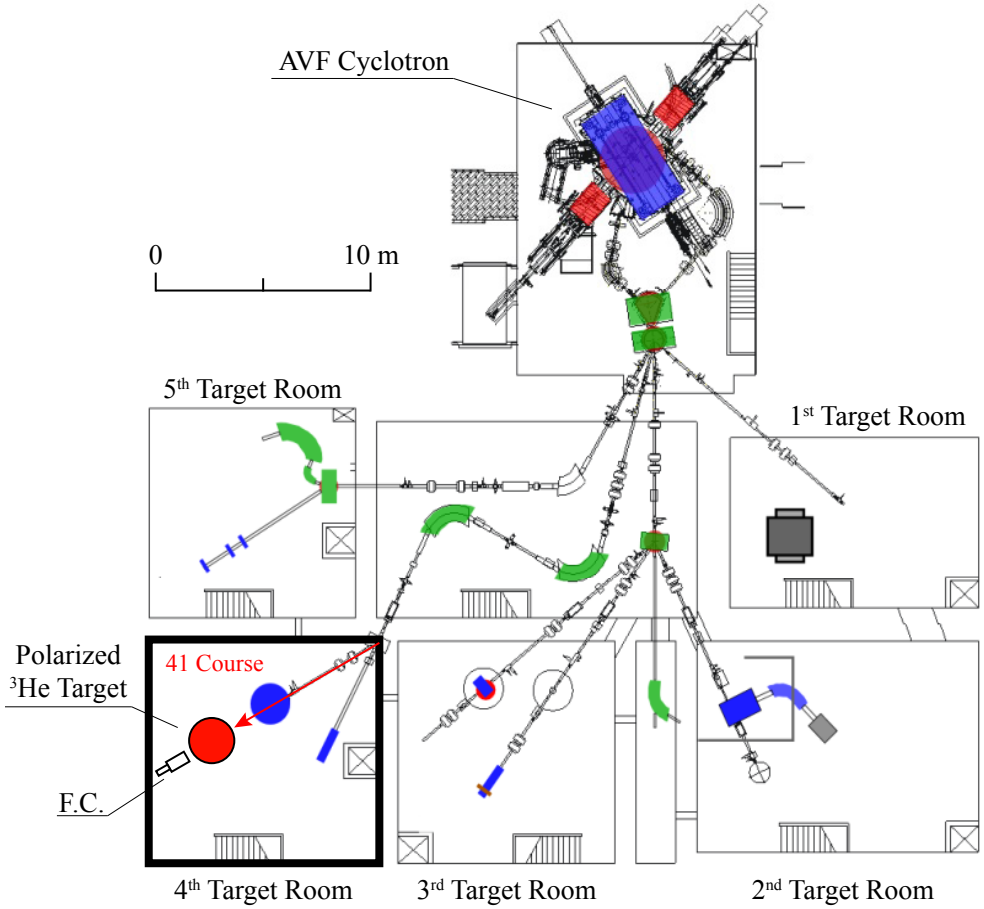

Figure 5.1: Schematic view of CYRIC. The experiment was performed at the 4th target room.

molecular pump to a pressure of 10^{-3} Pa.

The elastically scattered protons from the ^{3}He target were detected by $\Delta E-E$ detectors. The detectors were symmetrically placed in left and right positions in the horizontal plane. To estimate background events the measurement with the blank cells was also performed. The blank cells had almost the same dimensions to those of the ^{3}He target cells and they contained N_2 gas.

The experimental conditions for each measurement are summarized in Table 5.1.

5.2 Overview of Experiment at RCNP

The experiment at 100 MeV was performed by using the unpolarized proton beam at RCNP. Figure 5.3 shows a schematic view of RCNP. Proton beams provided by an atomic

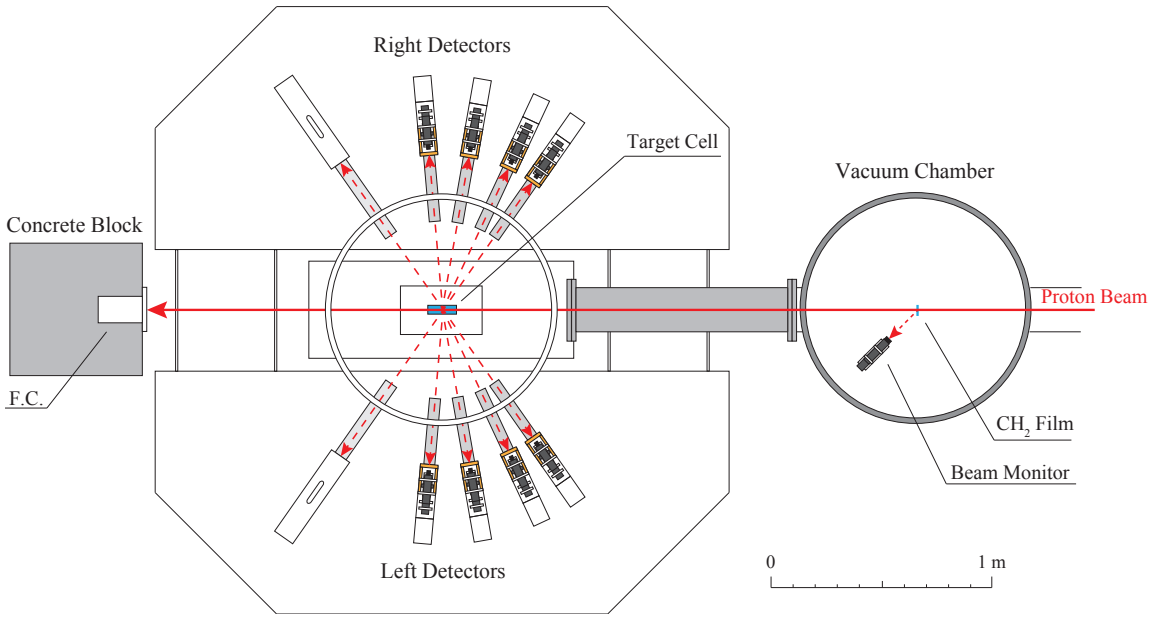

Figure 5.2: Experimental setup in the 4th target room.

Table 5.1: Experimental conditions for the measurement of ^{3}He analyzing power at CYRIC.

Beam	Proton
Incident energy	70 MeV
Beam intensity	5–10 nA
Target	^{3}He gas ($\sim$ 2 mg/cm^2)
Detectors	ΔE–E detectors
Measured angle	$\theta_{\rm cm} = 46°$–$141°$

Table 5.2: Experimental conditions for the measurement of ^{3}He analyzing power at RCNP.

Beam	Proton
Incident energy	100 MeV
Beam intensity	$\sim$ 30 nA
Target	^{3}He gas ($\sim$ 2 mg/cm^2)
Detectors	ΔE–E detectors
Measured angle	$\theta_{\rm cm} = 47°$–$149°$

beam type polarized ion source were accelerated up to 21.9 MeV by the injector cyclotron AVF, and then up to 100 MeV by the Ring cyclotron. The beams were transported to the east experimental hall. The experiment with the polarized ^{3}He target was conducted at the ENN beam line. The layout of the experimental setup is shown in Fig. 5.4. The polarized ^{3}He target was installed just downstream of the doublet quadrupole magnets (QM9D-ENN). To separate the vacuum the beam ducts upstream as well as downstream of the target were sealed by Havar foils with thickness of 10 μm. Charge collection of the beam was performed by using a FC. The beam line polarimeter was used as a beam monitor for this experiment. The detectors for p–^{3}He elastic scattering were set symmetrically in left and right positions as were similar to those in the measurement at CYRIC. The experimental conditions are summarized in Table 5.2.

5.3 Experimental Apparatus

5.3.1 Polarized ^{3}He Target

During the course of the experiment the ^{3}He polarization was monitored by using the AFP-NMR method. Together with this the direction of the ^{3}He nuclear spin was flipped every hour. We used the Koganei cell as the target for the experiments performed in December 2016, and June 2017, and the Ishibashi cell for the experiments performed in June 2018, and November 2018.

Figures 5.5, 5.6, 5.7 and 5.8 show the ^{3}He polarization of the target chamber during the experiment in December 2016, June 2017, June 2018, and November 2018, respectively. The open red circles (blue squares) denote the spin-up (down) state of the ^{3}He polarization. We calibrated the NMR signal using the experimental results of the neutron transmission measurement. The errors shown in the figures come from the uncertainties of the results of the neutron transmission measurement and those from fitting the NMR signals obtained.

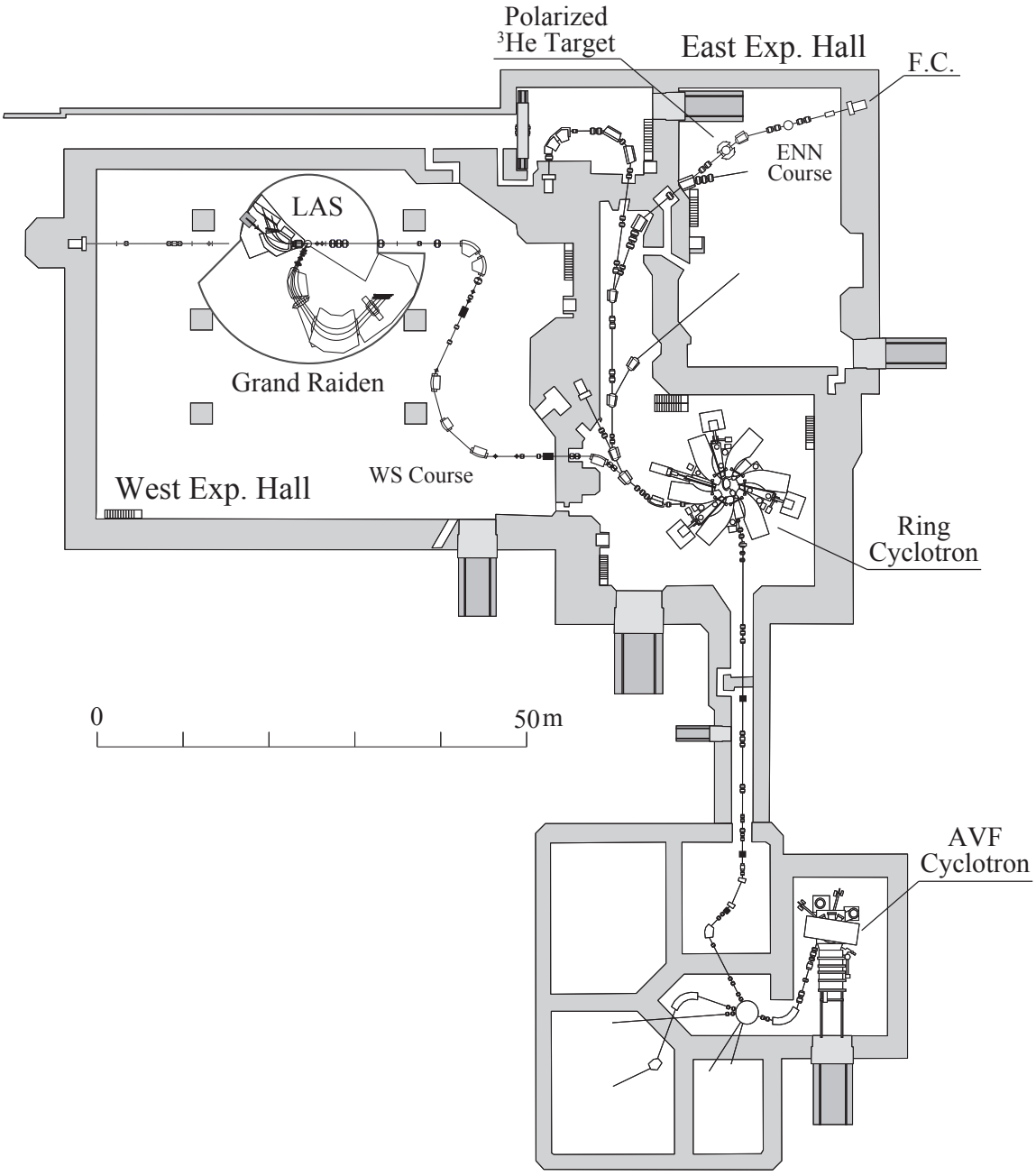

Figure 5.3: Schematic view of RCNP. The experiment was performed at the east experimental hall.

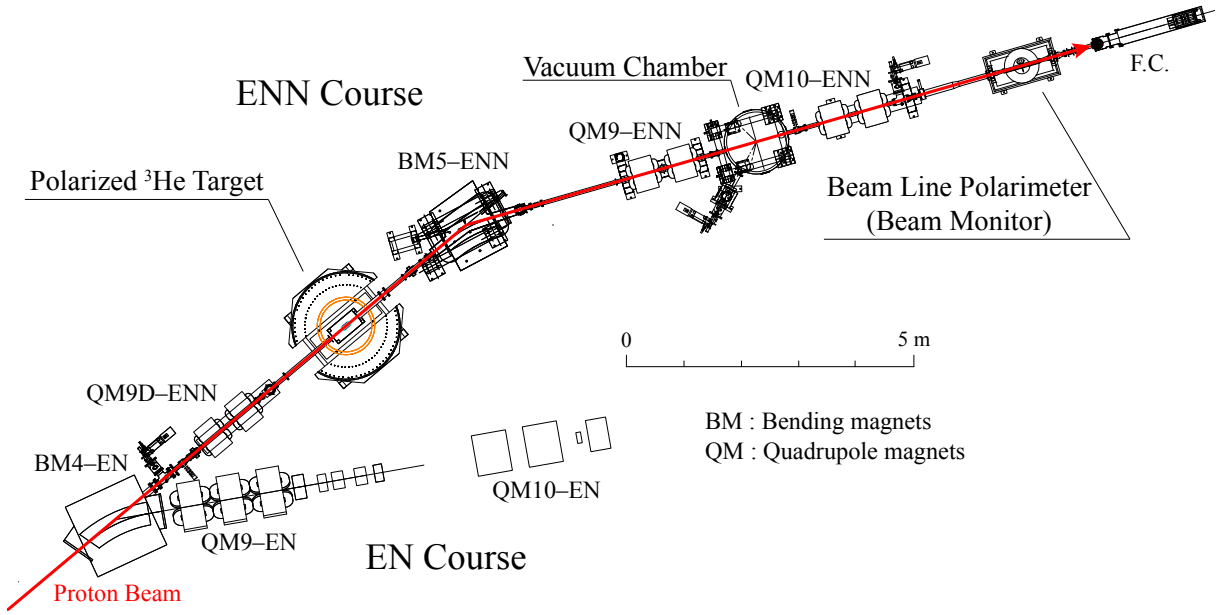

Figure 5.4: Layout of the ENN course in the east experimental hall. The polarized ^{3}He target were installed downstream of doublet quadrupole magnets QM9D-ENN.

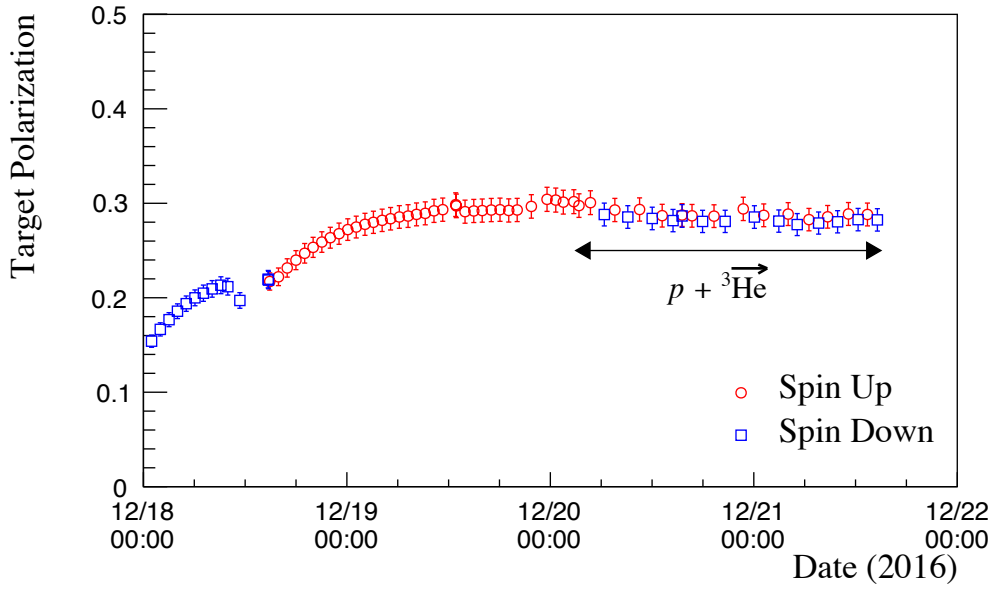

Figure 5.5: ^{3}He polarization of the Koganei cell measured by the AFP-NMR method during the experiment in December, 2016. The open circles (squares) show the spin-up (down) state of the ^{3}He polarization. The horizontal arrow is the period of the measurement of ^{3}He analyzing power.

The ^{3}He polarization suddenly decreases at 10:00 am on 7 June 2017 and at 12:00 pm on 21 November 2018. The first is due to the fact that the quarter-wave plates were not rotated to an appropriate angle after reversing the direction of ^{3}He spin axis by the AFP-NMR method. The second occurred when the laser operation was stopped accidentally. As for this we restarted the laser operation immediately. The maximum and average values of the ^{3}He polarization of the experiments are summarized in Table 5.3. After the measurement of ^{3}He analyzing power, we performed the measurement with the unpolarized ^{3}He target to estimate the false asymmetry of elastically scattered protons from the target.

5.3.2 Detectors for p–^{3}He Elastic Scattering

Elastically scattered protons were detected by ΔE–E detectors which were placed symmetrically in left and right positions. A ΔE detector is a thin plastic scintillator (BC-408) coupled with a photomultiplier tube (PMT) to measure the energy loss of charged particles. A E detector is a thick plastic scintillator or NaI(Tl) scintillator coupled with a PMT to measure the total energy of charged particles. The layouts of ΔE–E detector sets #1 and #2, and #3 are shown in Figs. 5.9, 5.10 and 5.11, respectively. The #1 and #2 sets were used in the experiment at CYRIC, and the #3 set was used in the experiment at RCNP.

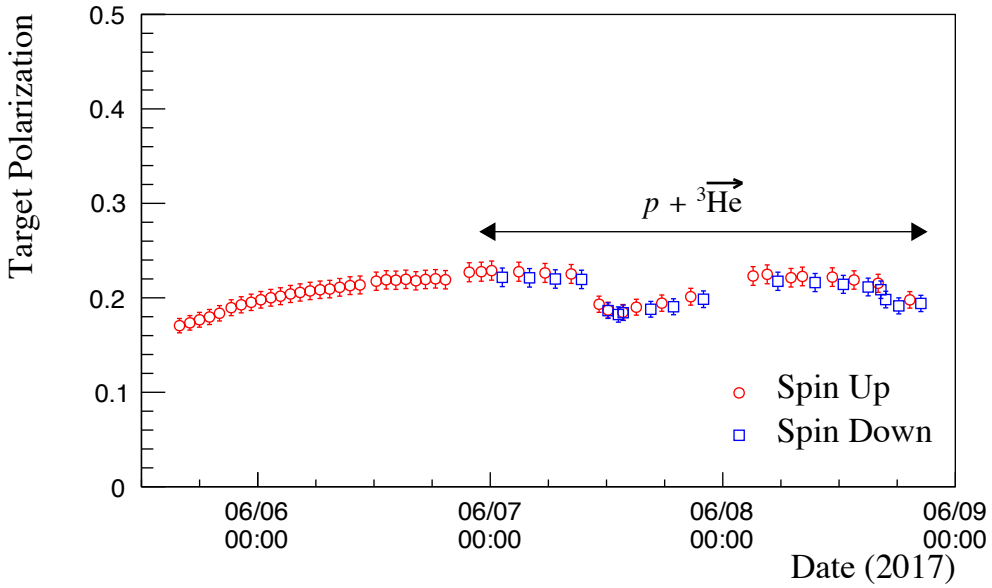

Figure 5.6: ^{3}He polarization of the Koganei cell measured by the AFP-NMR method during the experiment in June, 2017. For description of data and an arrow see Fig. 5.5.

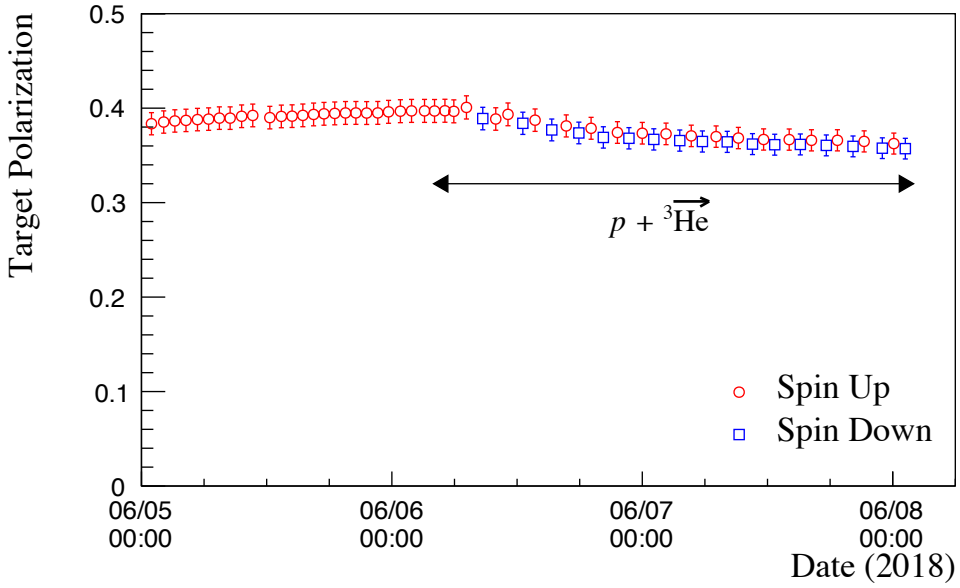

Figure 5.7: ^{3}He polarization of the Ishibashi cell measured by the AFP-NMR method during the experiment in June, 2018. For description of data and an arrow see Fig. 5.5.

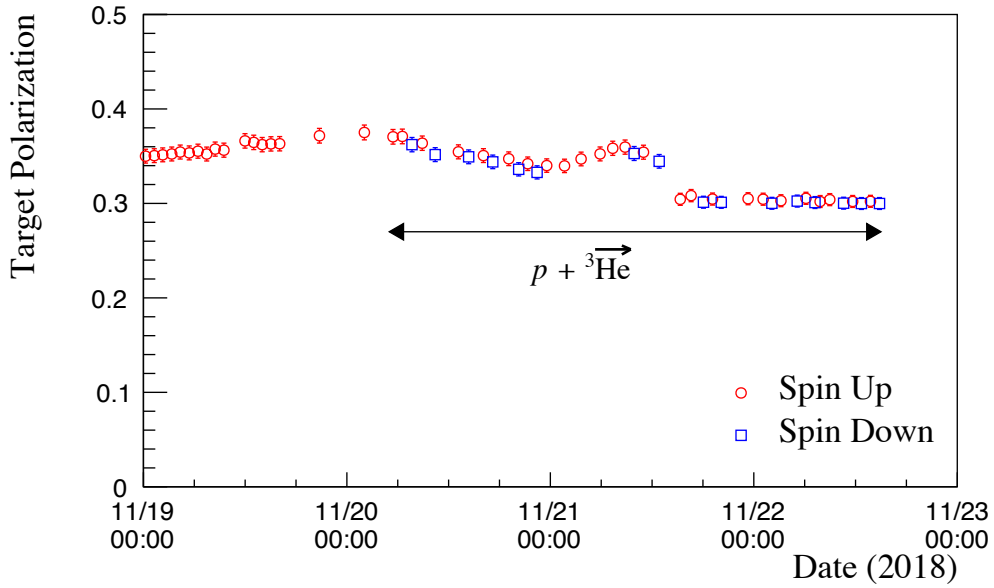

Figure 5.8: ^{3}He polarization of the Ishibashi cell measured by the AFP-NMR method during the experiment in November, 2018. For description of data and an arrow see Fig. 5.5.

Table 5.3: Maximum and average values of the ^{3}He polarization of the target chamber during the measurement of ^{3}He analyzing power.

Exp.	Cell	Max.	Ave.
CYRIC, Dec. '16	Koganei	0.300(11)	0.287(11)
CYRIC, Jun. '17	Koganei	0.229(9)	0.211(8)
CYRIC, Jun. '18	Ishibashi	0.401(9)	0.372(9)
RCNP, Nov. '18	Ishibashi	0.371(22)	0.327(20)

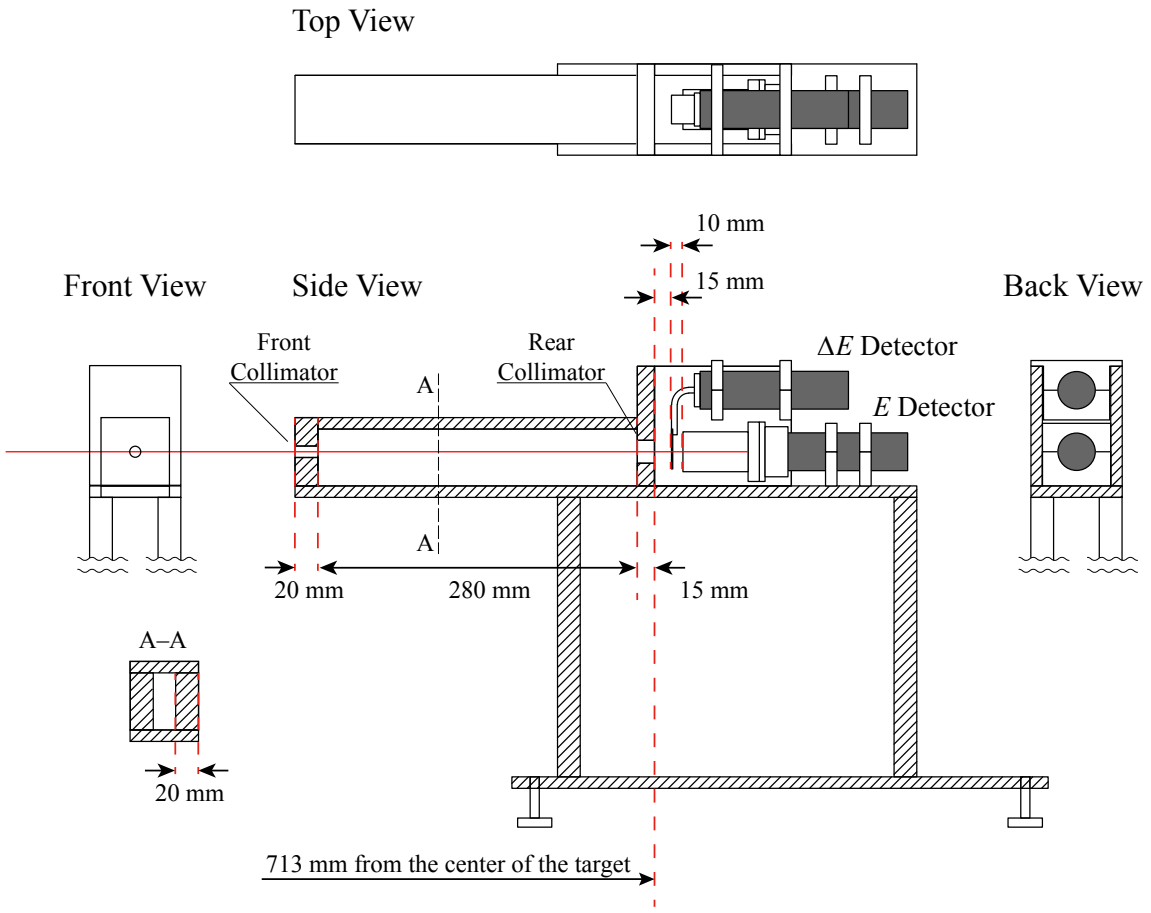

Figure 5.9: ΔE–E detector set #1 used in the experiment at CYRIC.

The specifications of the detector sets are summarized in Table 5.4. For all the detector sets, double-slit collimators were set to determine the target thickness and the solid angles. Collimators with different diameters were applied in order to restrict the event rates. The detector sets #1 and #3 were covered with brass plates to reduce the background events, e.g. protons scattered from Kapton films / Havar foils and other sources from the FC. As for the set #1 the detectors were shielded by lead blocks.

5.3.3 Beam Monitoring System

Relative values of the beam intensities were monitored by the beam monitor in the experiments. For the experiments at CYRIC, the beam monitor was installed in the vacuum chamber placed upstream of the ^{3}He target. A polyethylene (CH_2) film with target thickness of 1.8 mg/cm^2 was mounted on a target ladder in the vacuum chamber. The scattered

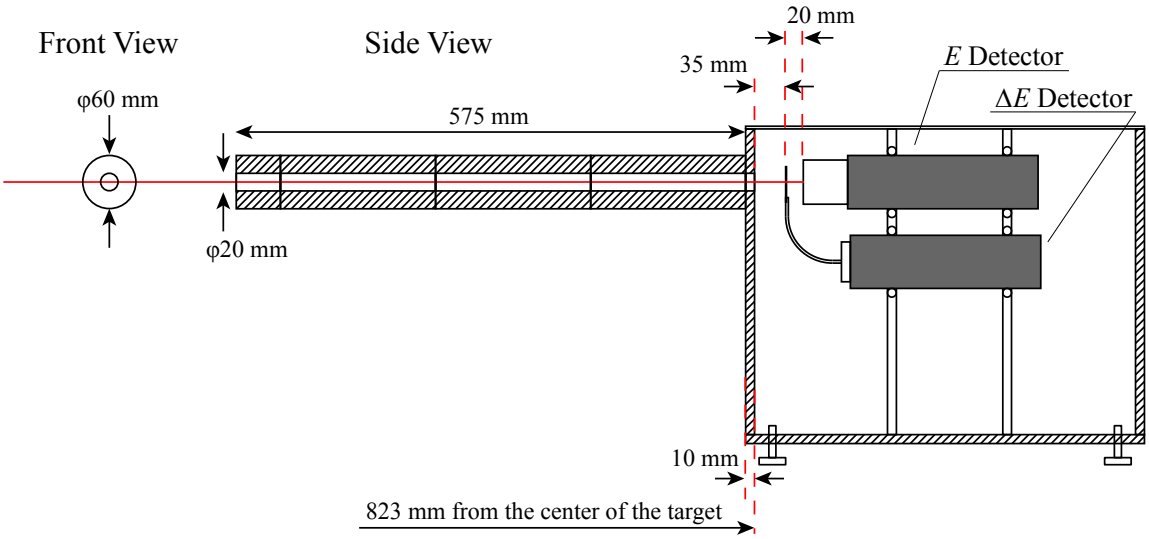

Figure 5.10: ΔE–E detector set #2 used in the experiment at CYRIC.

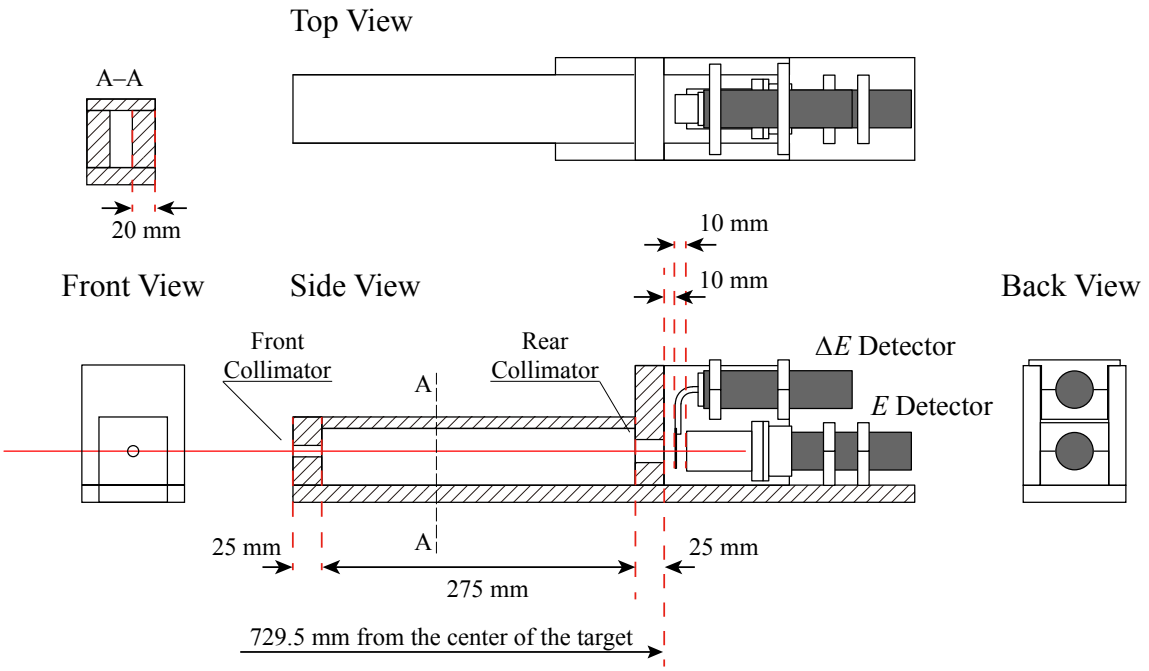

Figure 5.11: ΔE–E detector set #3 used in the experiment at RCNP.

Table 5.4: Specifications of the ΔE–E detector sets #1, #2 and #3. For the detectors sets #1 and #3, F (R) denotes the front (rear) collimator.

Detector sets	#1	#2	#3
	ΔE detector		
Scintillator	Plastic (BC-408)	Plastic (BC-408)	Plastic (BC-408)
PMT	H7415	H1161	H7415
Scintillator size	$25^{\mathrm{W}} \times 30^{\mathrm{H}}$ mm	$40^{\mathrm{W}} \times 40^{\mathrm{H}}$ mm	$25^{\mathrm{W}} \times 30^{\mathrm{H}}$ mm
Scintillator thickness	$0.2, 0.5, 1$ mm	1 mm	$0.5, 1, 2$ mm
	E detector		
Scintillator	NaI(Tl)	Plastic (BC-408)	NaI(Tl)
PMT	H7415	H1161	H7415
Scintillator size	$31^{\mathrm{W}} \times 31^{\mathrm{H}}$ mm	ϕ50 mm	$31^{\mathrm{W}} \times 31^{\mathrm{H}}$ mm
Scintillator thickness	50 mm	50 mm	50 mm
	Collimators		
Material	Al (F) Brass (R)	Al	Brass (F) Brass (R)
Collimator diameter	$5.0, 6.8, 8.4, 10$ mm (F) $9.0, 12, 15, 20$ mm (R)	20 mm	$5.0, 10$ mm (F) $9.0, 20$ mm (R)
Solid angle	$0.11, 0.20, 0.30, 0.46$ msr	0.46 msr	$0.11, 0.43$ msr
Acceptance	$\pm 1.3^\circ, 1.7^\circ, 2.1^\circ, 2.7^\circ$	$\pm 2.0^\circ$	$\pm 1.2^\circ, 2.6^\circ$

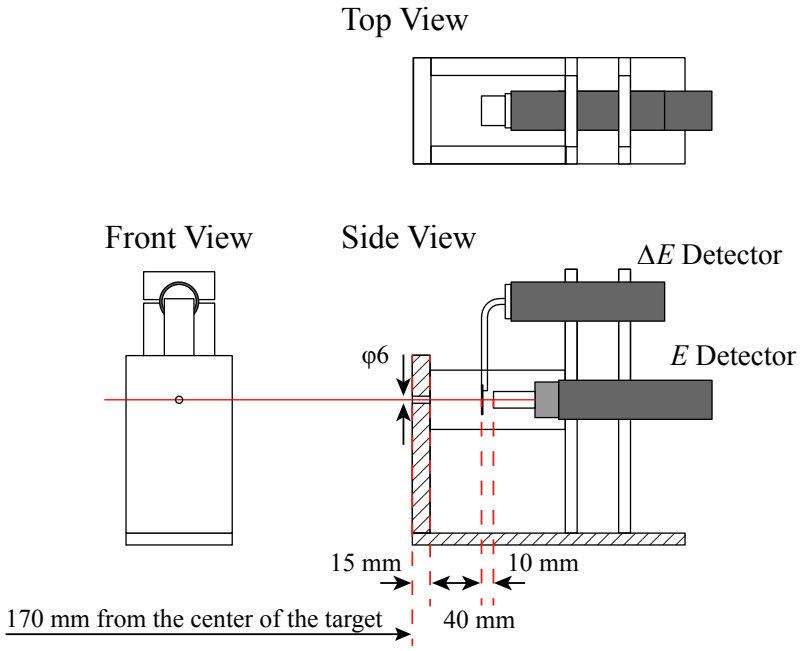

Figure 5.12: Layout of the detector set of the beam monitor for the experiment at CYRIC.

Table 5.5: Specifications of the beam monitor for the experiment at CYRIC.

	ΔE detector	E detector
Scintillator	Plastic (BC-408)	NaI(Tl)
PMT	H7415MOD	H7415MOD
Scintillator size	$25^{\mathrm{W}} \times 25^{\mathrm{H}}$ mm	ϕ14 mm
Scintillator thickness	2 mm	35 mm
Solid angle	0.86 msr	

protons from the film were detected by a ΔE–E detector set placed at 45° in the laboratory system. The layout of the beam monitor is shown in Fig. 5.12. A ΔE detector is a thin plastic scintillator with thickness of 2 mm coupled with a PMT to measure the energy loss of charged particles. A E detector is a NaI(Tl) scintillator with thickness of 30 mm coupled with a PMT to measure the total energy of charged particles. A ϕ6 slit collimator made of brass was set to determine the solid angle. In order to reduce the background, the detector set was covered with brass plates. The thickness of the collimator and the brass plates is 15 mm. The specifications of the beam monitor are shown in Table 5.5.

Monitor of the relative beam intensities was performed by using the elastic scattered protons from ^{12}C in the polyethylene film. Figure 5.13 shows a two-dimensional plot of the light outputs of the ΔE–E detectors and a one-dimensional energy spectrum of that

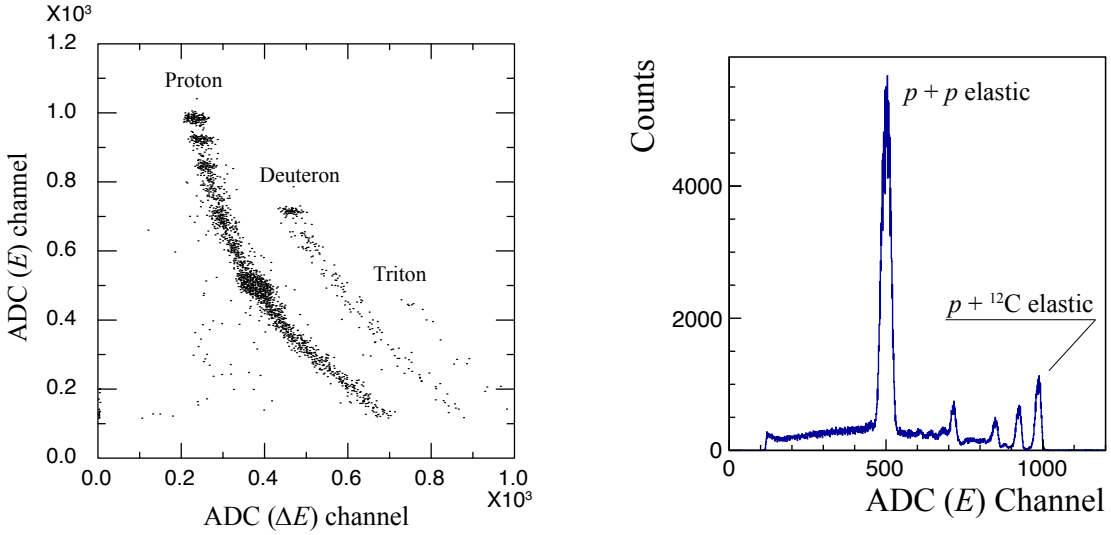

Figure 5.13: Two-dimensional light outputs of the ΔE–E detector set (left panel) for the experiment at CYRIC. The right panel shows a one-dimensional light output of the E counter.

of the E detector. Loci of protons, deuterons and tritons are clearly shown in Fig. 5.13. The peak at the highest channel corresponds to the p–^{12}C elastic scattering events in the energy spectrum of the E detector. We fitted this peak with Gaussian and obtained events in the range of $\pm 4\sigma$ as the relative value of the beam intensity. The standard deviation of the ratio of the relative beam intensity and the collected beam charge by the FC was about 3 % to the average ratio through the experiment. In this work, we used the collected beam charge by the FC as the beam intensity for the data analysis.

Relative beam intensities were also monitored by the beam monitor for the experiment at RCNP. In this experiment, the beam line polarimeter which was installed upstream of the FC (see Fig. 5.4) was used as a beam monitor. A stack of the CH_2 and the deuterated polyethylene (CD_2) films was used as the target. The target thickness was 9.2 mg/cm^2 for the CH_2 film and 10 mg/cm^2 for the CD_2 film, respectively. This target was mounted on the target ladder in the vacuum chamber. The vacuum chamber has four exit windows with opening angles being from 17° to 163° in the horizontal and vertical planes. The scattered protons from the target were detected by a NaI(Tl) scintillator coupled with a PMT. This detector was placed at $\theta_{\rm lab} = 45°$ in the down vertical position. The layout of the beam monitor for the experiment at RCNP is shown in Fig 5.14 and the specifications are summarized in Table 5.6.

Monitor of the relative beam intensities was performed by using the elastic scattered

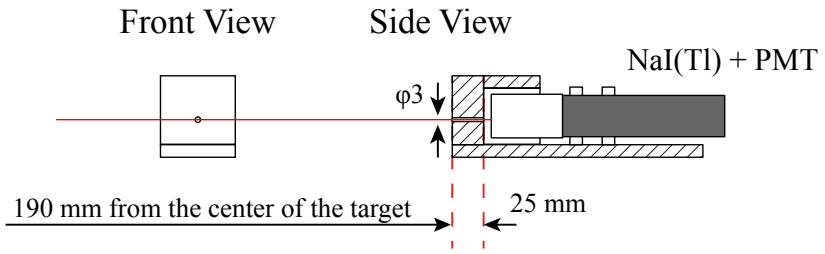

Figure 5.14: Layout of the beam monitor for the experiment at RCNP.

Table 5.6: Specifications of the beam monitor for the experiment at RCNP.

Scintillator	NaI(Tl)
PMT	H7415MOD
Scintillator size	$31^{\mathrm{W}} \times 31^{\mathrm{H}}$ mm
Scintillator thickness	50 mm
Solid angle	0.15 msr

protons from ^{12}C in the polyethylene film similarly to that in the measurement at CYRIC. Figure 5.15 shows a one-dimensional energy spectrum of the light output of the detector. The peak at the highest channel corresponds to the p–^{12}C elastic scattering events. We fitted this peak with Gaussian and counted events in the range of $\pm 4\sigma$ as the relative beam intensity. The standard deviation of the ratio of the relative beam intensity and the collected beam charge by the FC was about 4 % to the average ratio through the experiment. We used the collected beam charge by the FC as the beam intensity for the data analysis.

5.3.4 Trigger and Data Acquisition System

The schematic diagram to make a trigger is shown in Fig. 5.16. Anode signals of the PMTs for the ΔE counters were sent to the constant fraction discriminators (CFD; CF8000, ORTEC). CF8000 has an analog output that buffers the input signal (E-out). The analog output was sent to 200 nsec delay and then digitized by a charge-integrating fast encoding and readout ADC (FERA) to get the pulse height information. One of the NIM logic outputs provided by the CFD was sent to 200 nsec delay and subsequently sent to a FERA via a time-to-FERA converter (TFC) in order to get the arrival timing information of the particle. The other logic signal from the CFD was used to make a trigger. All the logic signals for the ΔE counters and the signal from the beam monitor after a rate divider were

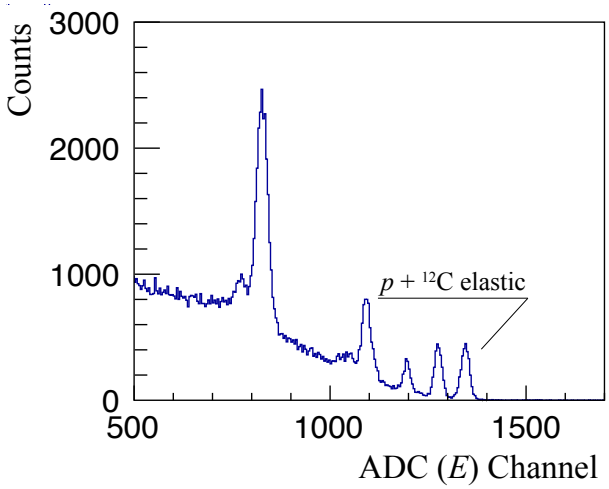

Figure 5.15: One-dimensional light output of the beam monitor for the experiment at RCNP.

summed as the event trigger.

Anode signals of the PMTs for the thick-plastic E counters were sent to the CFD. The analog output was sent to 200 nsec delay and then digitized by a FERA to get the pulse height information. The NIM logic output provided by the CFD was sent to 200 nsec delay and subsequently sent to a FERA via a TFC to get the arrival timing information of the particle. Anode signals of the PMTs for the NaI(Tl) scintillators were divided into two signals. One of the signals was sent to 200 nsec delay and then digitized by a FERA for the pulse height information. The other signal was sent to a CFD (ORTEC 935) after a timing filter amplifier (TFA; ORTEC 474). The logic signal from the CFD was sent to 200 nsec delay and then to a FERA via a TFC for encoding the timing information. As for the accelerator RF signals, the timing information was also read out by using a FERA.

The digitized data through the above process were transferred to a high speed memory module (HSM) in a VME system through the FERA bus. The stored data in the HSM were transferred to a Linux personal computer via an optical cable. Manufacturer names and model numbers of the modules used in the DAQ system are summarized in Table 5.7.

5.4 Data Analysis

The procedure of the data analysis to obtain the ^{3}He analyzing power is described in this section. At first, we performed the particle identification by the ΔE–E method. Second, we selected the events of p–^{3}He elastic scattering by using the light output spectra of the E

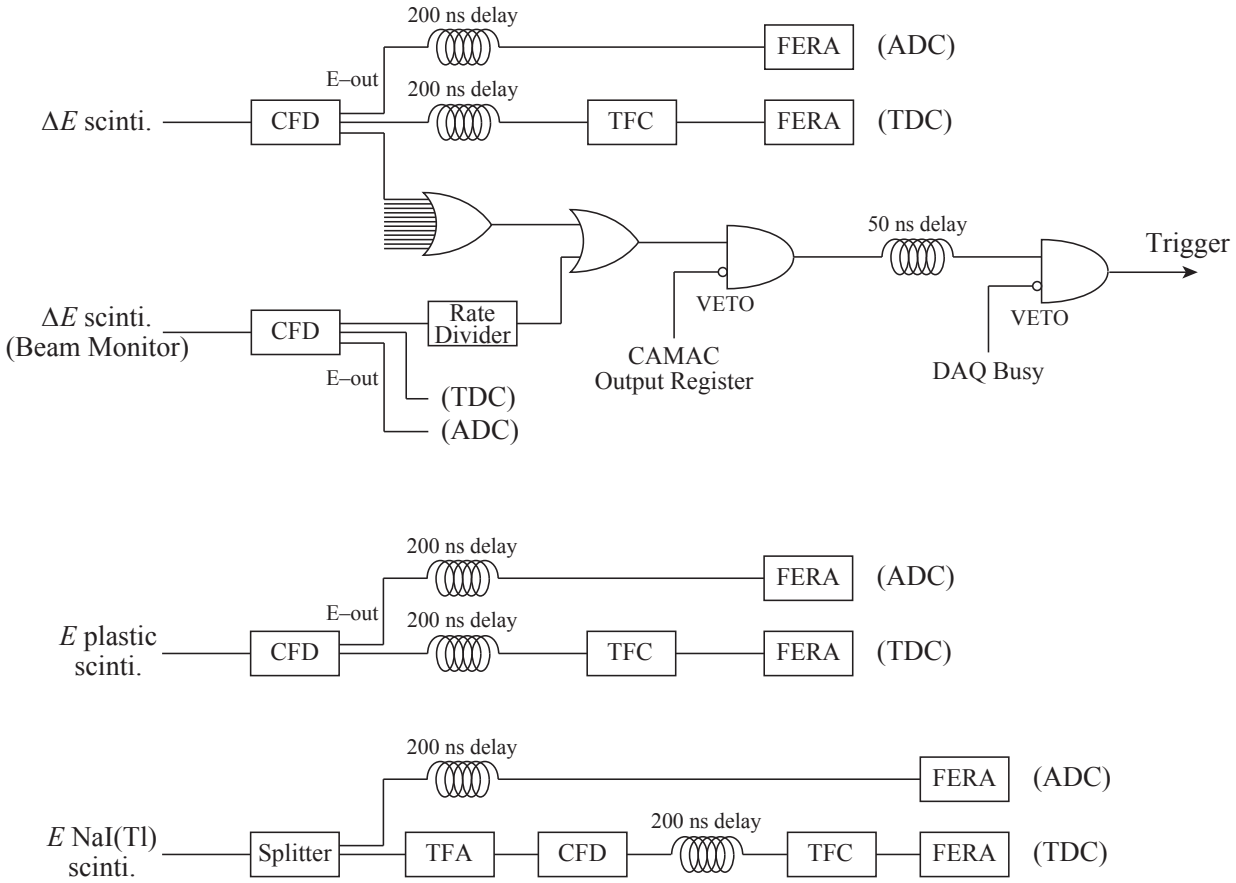

Figure 5.16: Block diagram of the trigger production circuit and the DAQ system of the plastic and NaI(Tl) scintillators for the measurement.

Table 5.7: Manufacturer names and model numbers of the modules used in the DAQ system.

Modules	Manufacturer	Model number
CFD	ORTEC	CF8000
	ORTEC	935
ADC, TDC	LeCroy Co.	4300B
TFC	LeCroy Co.	4303
TFA	ORTEC	474
HSM	Creative Electronic Systems S.A.	8170

detectors. Finally, we extracted the ^{3}He analyzing powers from the events and the target polarization.

5.4.1 Particle Identification

Scattered particles from the target were identified by the ΔE–E method based on the Bethe-Bloch formula:

$$\Delta E \propto \frac{Z^2}{E}, \tag{5.1}$$

where Z is the atomic number of incident particles. Figure 5.17 shows two-dimensional light outputs of the ΔE and E detectors at $\theta_{\rm lab} = 45°$, 65° and 85° at the experiment of CYRIC. The E detectors at $\theta_{\rm lab} = 45°$ and 85° were NaI(Tl) scintillators, and the detector at $\theta_{\rm lab} = 65°$ was a plastic scintillator. Figure 5.18 shows two-dimensional light outputs of the ΔE and E detectors at $\theta_{\rm lab} = 100°$ for the target cell as the Koganei and the Ishibashi cells. In Fig. 5.19, the two-dimensional light outputs of the ΔE and E detectors at the experiment of RCNP are also shown for $\theta_{\rm lab} = 65°$, 85°, 105° and 115°. Loci of protons are clearly seen and distinguished from the other particles in Figs. 5.17, 5.18 and 5.19.

To select scattered protons, we performed a linear correction of the two-dimensional plots. We fit the proton loci of each two-dimensional plot with an exponential function, and corrected them by using the fitting results. Figures 5.20 and 5.21 show corrected two-dimensional light outputs of the ΔE and E detectors at the experiment of CYRIC. Corrected two-dimensional light outputs of the ΔE and E detectors at the experiment of RCNP are also shown in Fig. 5.22. Particle identification of the scattered protons was performed by the gates for the corrected two-dimensional plots.

Figures 5.23, 5.24 and 5.25 show light output spectra of the E detectors obtained from by projecting the proton-gated spectra of Figs. 5.20, 5.21 and 5.22 on the y-axis, respectively. The large peaks clearly seen for all the measured angles are from the events of p–^{3}He elastic scattering.

The peaks at the highest channels found at rather forward angles are from elastically scattered proton events from ^{14}N. For reference the spectra obtained with the blank cell which contained ^{14}N gas are shown as cyan lines in Figs. 5.23, 5.24 and 5.25. Differences of the peak positions, energy resolutions, peak heights seen in p–^{14}N elastic events are due to the differences of the thickness of the glass target cells and the amount of ^{14}N gas in the cells, which is very difficult to control in our target production system. However the background spectra indicate that background events around the p–^{3}He elastic peaks have

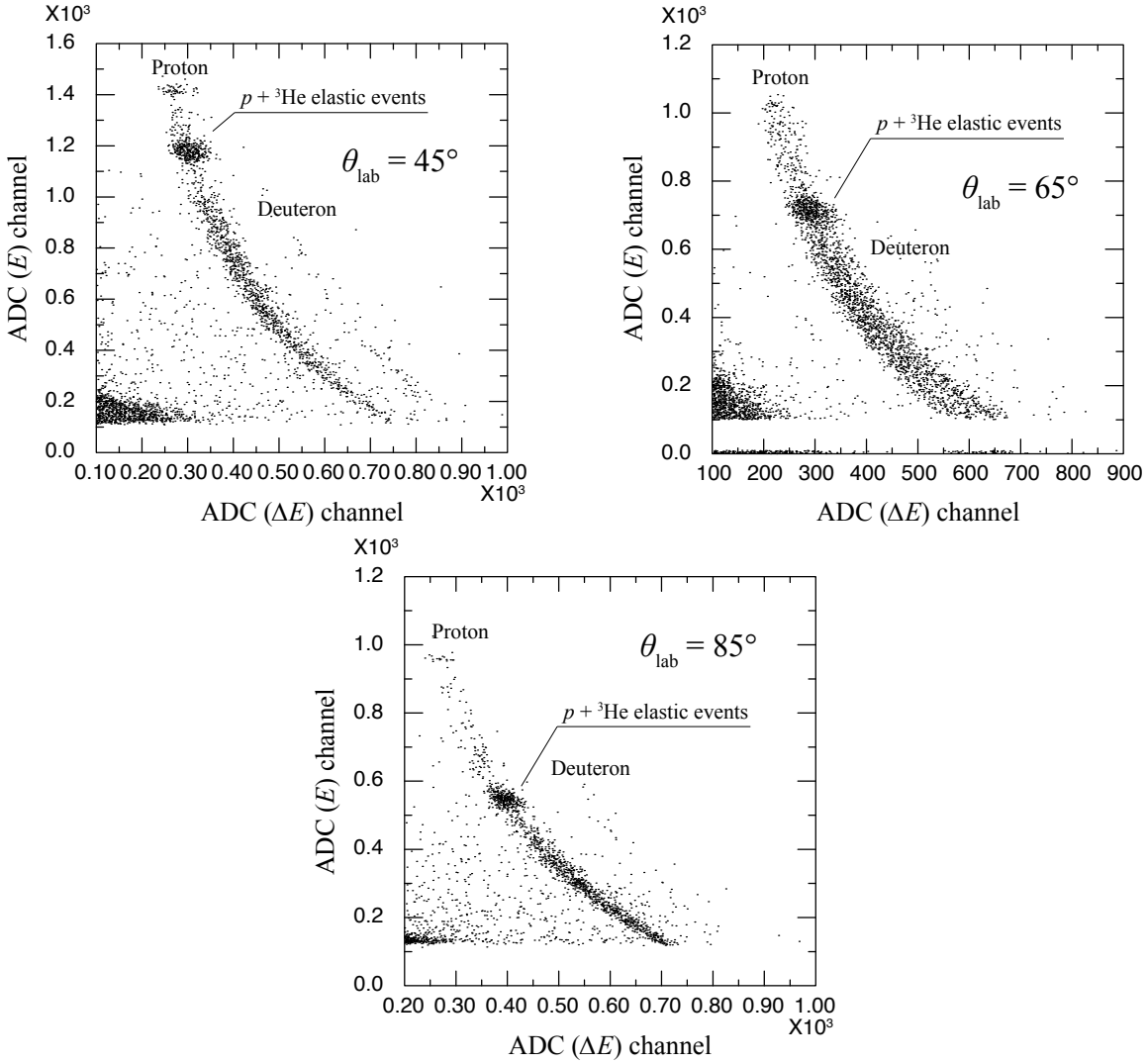

Figure 5.17: Two-dimensional light outputs of the ΔE–E detectors for $\theta_{\rm lab} = 45°$, 65° and 85° at the experiment of CYRIC.

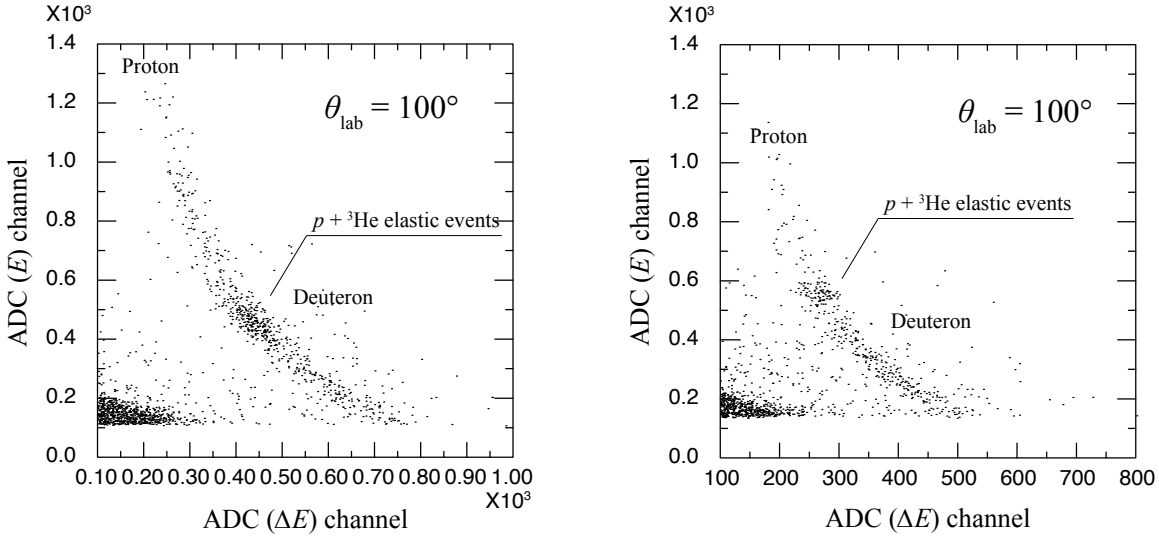

Figure 5.18: Two-dimensional light outputs of the ΔE–E detectors for $\theta_{\rm lab} = 100^\circ$ at the experiment of CYRIC. The left (right) panel shows the light output when the ^{3}He target was the Koganei (Ishibashi) cell.

almost linear structure. Together with this the events seen below the p–^{3}He elastic peaks are identified as the inelastic p–^{3}He scattering.

One should also note the spectra obtained at the same angles of $\theta_{\rm lab} = 100^\circ$ but with the different target cells shown in Fig. 5.24. The Ishibashi cell with 1 mm thickness of the side surface provides better energy resolution (0.82 MeV) than that by the Koganei cell with 2 mm thickness (1.4 MeV).

5.4.2 Event Selection

In order to extract the events from the p–^{3}He elastic events we performed background subtraction. We fitted the light output spectra with the function combining a gaussian for p–^{3}He elastic peak, a linear function for the background around the elastic peak, and a phenomenological function for the inelastic p–^{3}He scattering events. The fitting was performed around and slightly below the p–^{3}He peak positions. The phenomenological function is expressed as [117],

$$f_{\rm inela} = a\left\{1 - \exp\left(\frac{x-b}{c}\right)\right\} \times \left\{1 + \left(\frac{d-x}{e}\right)^2\right\}^{-1}. \tag{5.2}$$

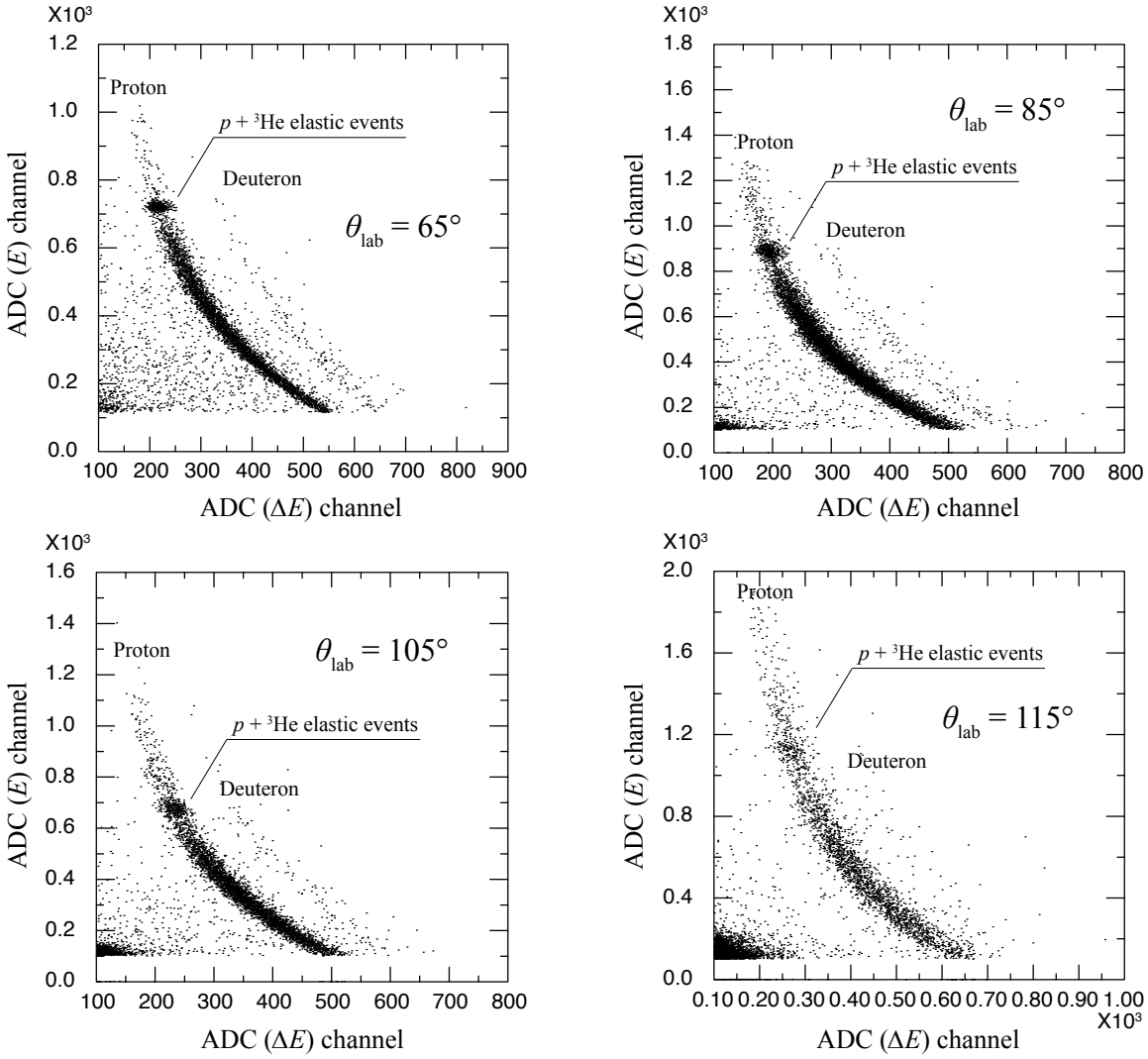

Figure 5.19: Two-dimensional light outputs of the ΔE–E detectors for $\theta_{\rm lab} = 65°$, 85°, 105° and 115° at the experiment of RCNP.

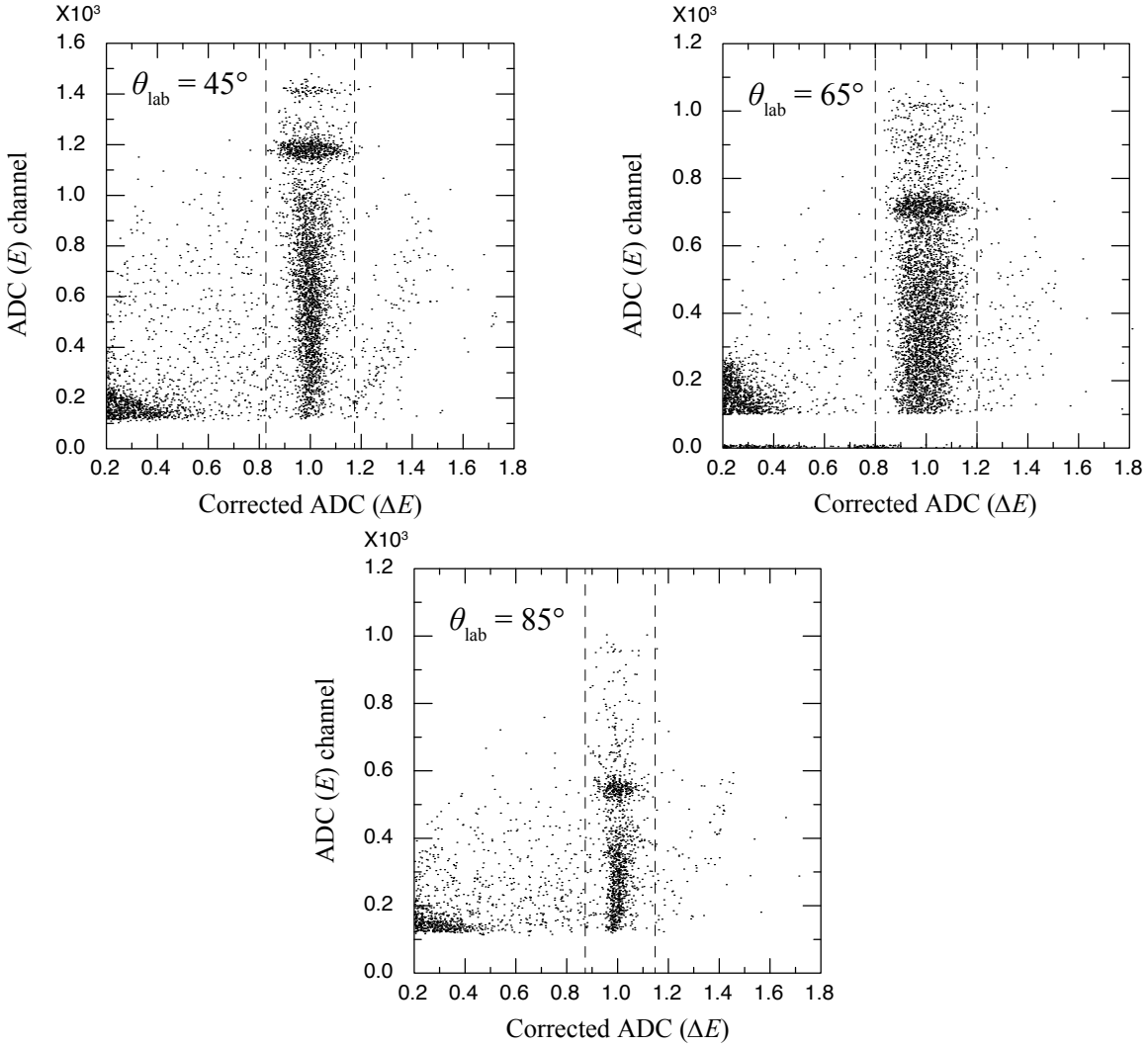

Figure 5.20: Corrected two-dimensional light outputs of the ΔE–E detectors for $\theta_{\rm lab}$ = 45°, 65° and 85° at the experiment of CYRIC. The vertical dashed lines are the gates for particle identification.

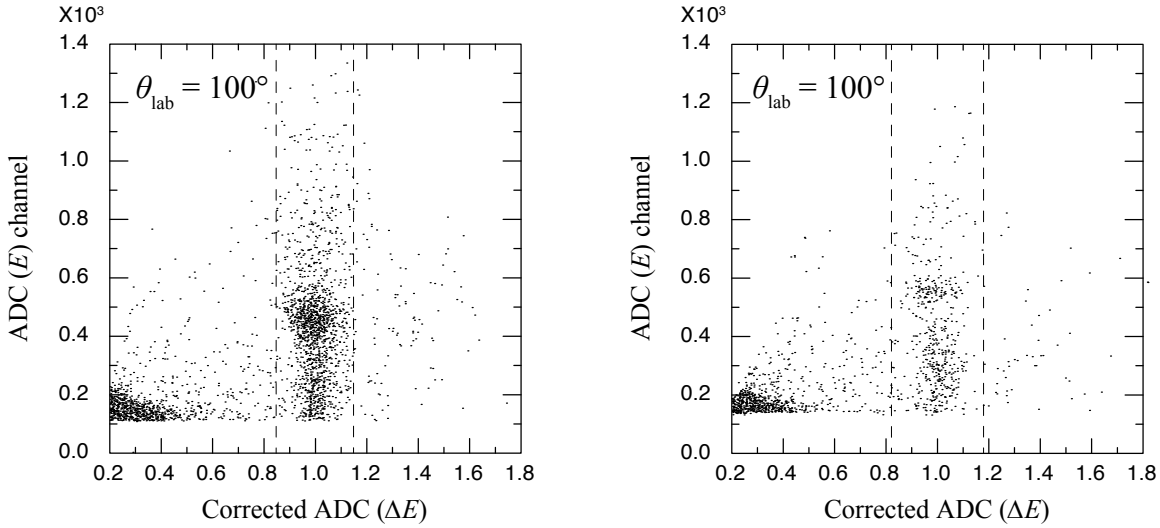

Figure 5.21: Corrected two-dimensional light outputs of the ΔE–E detectors for $\theta_{\rm lab} = 100°$ at the experiment of CYRIC. The left (right) panel shows the light output when the ^{3}He target was the Koganei (Ishibashi) cell. The vertical dashed lines are the gates for particle identification.

This function well describe the structure of the quasi-free reaction of ^{208}Pb$(n,p)^{208}$Tl at both 198 and 458 MeV as well as the $(\pi^{\pm},\pi^0)$ reaction for a wide range of targets and energies [118,119]. The threshold channels b in Eq. (5.2) were determined by the kinematics of p+^{3}He and the energy calibration for each light output spectrum of the E detector. We assumed that the threshold channels of the inelastic scattering are lower than the p+^{3}He elastic peaks by the proton separation energy of ^{3}He, $S_p = 5.49$ MeV.

The deposited energies of scattered protons in the E detectors can be calculated from the kinematics. In this calculation, we considered the energy loss of protons by passing through the glass of the ^{3}He cells, air and the ΔE detectors. Tables 5.8 and 5.9 show the calculated energies of protons at the E detectors from kinematics with incident energies of 70 MeV for CYRIC and 100 MeV for RCNP. The energy calibration was performed by using the elastic scattering peak positions of p+^{3}He for each detector and each run. The origin of the calibration was set to the pedestals of each detector. Here, we assumed that the relation between the ADC channels and the energies deposited in the E detectors is linear.

Figures 5.26 and 5.27 show the results of the fitting to the light output spectra of the E detectors at the experiment of CYRIC. The fitting results for the light output spectra at the experiment of RCNP are shown in Fig. 5.28. Using the fitting results, we counted

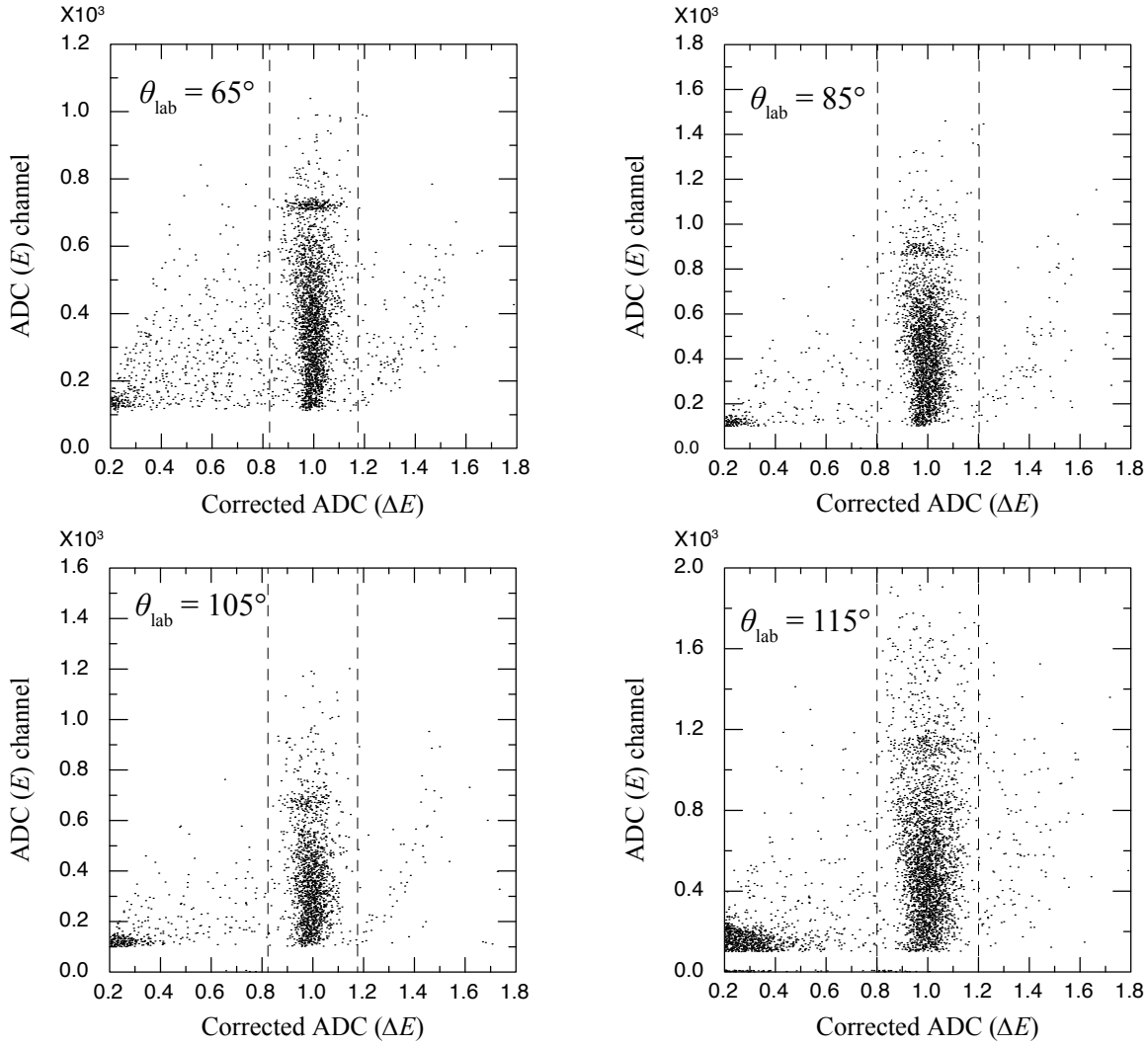

Figure 5.22: Corrected two-dimensional light outputs of the ΔE–E detectors for $\theta_{\rm lab} = 65°$, 85°, 105° and 115° at the experiment of RCNP. The vertical dashed lines are the gates for particle identification.

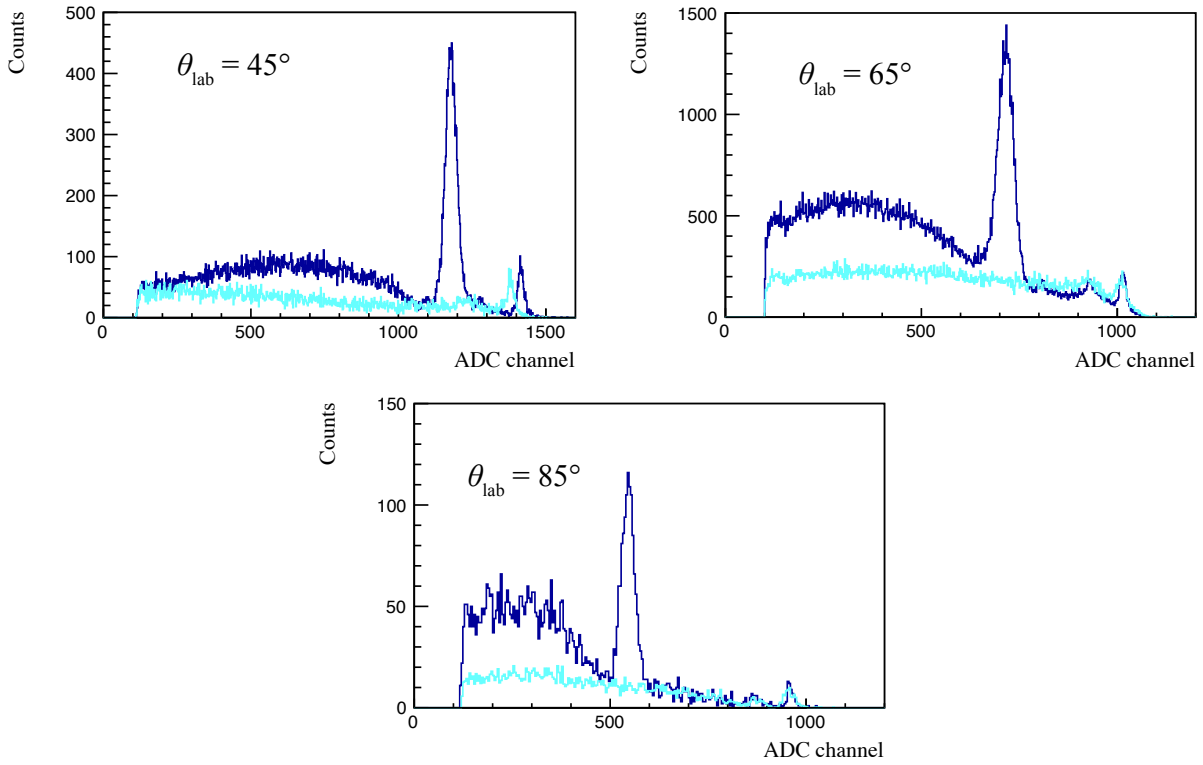

Figure 5.23: Light output spectra of the E detectors for $\theta_{\rm lab} = 45°$, 65° and 85° at the experiment of CYRIC. The cyan solid lines are the spectra of the blank cell.

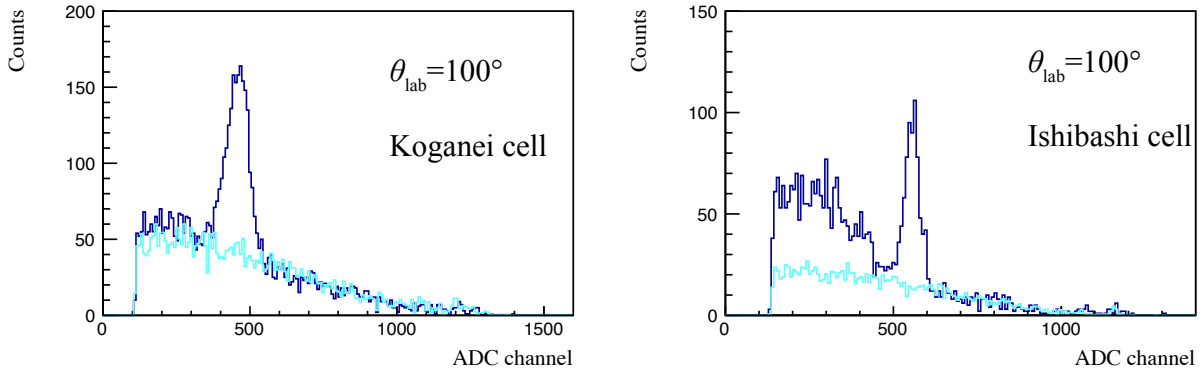

Figure 5.24: Light output spectra of the E detectors for $\theta_{\rm lab} = 100°$ at the experiment of CYRIC. The left (right) panel shows the spectrum when the ^{3}He target was the Koganei (Ishibashi) cell. The cyan solid lines are the spectra of the blank cell.

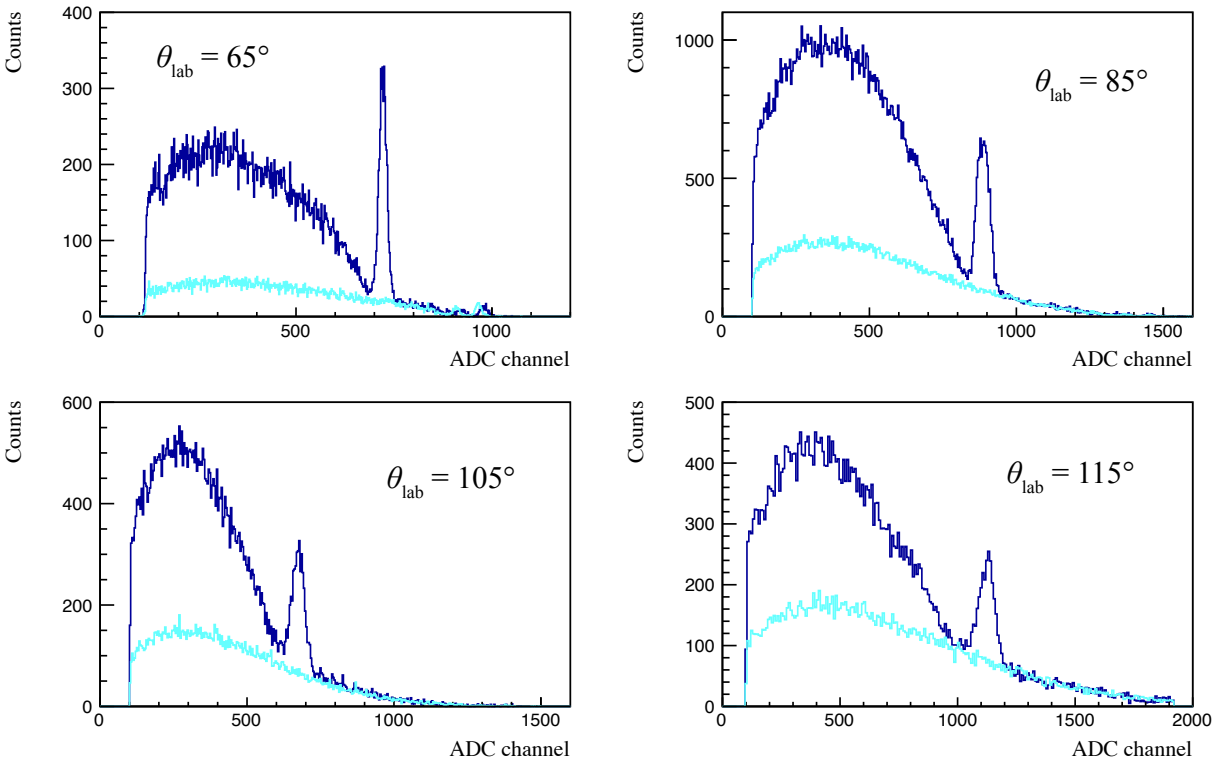

Figure 5.25: Light output spectra of the E detectors for $\theta_{\rm lab} = 65°$, $85°$, $105°$ and $115°$ at the experiment of RCNP. The cyan solid lines are the spectra of the blank cell.

Table 5.8: Calculated proton energies E_p deposited in the E detectors for p+^{3}He and p+^{14}N at the experiment of CYRIC with a incident energy of 70 MeV. An asterisk denotes the Koganei cell for the target.

$\theta_{\rm lab}$	$\theta_{\rm cm}$	E_p (p+^{3}He ela.) [MeV]	E_p (p+^{3}He inela.) [MeV]	E_p (p+^{14}N ela.) [MeV]
35	46.6	47.9*	41.4*	54.7*
45	59.3	44.4*	38.0*	55.0*
55	71.6	39.7*	33.1*	54.3*
65	83.4	34.5*	27.7*	53.3*
70	89.0	31.8*	24.8*	52.7*
		35.0	28.6	54.9
75	94.6	30.1*	23.2*	52.7*
80	99.9	27.4*	20.2*	52.0*
85	105.2	25.4*	18.0*	51.6*
		27.4	20.6	52.8
95	115.1	17.9*	7.8*	49.1*
100	119.8	16.4*	5.5*	48.8*
		21.3	13.8	51.1
110	128.9	10.2*	–	47.1*
115	133.2	15.5	6.1	49.1
125	141.3	11.0	–	47.6

Table 5.9: Calculated proton energies E_p deposited in the E detectors for p+^{3}He and p+^{14}N at the experiment of RCNP with a incident energy of 100 MeV. The target cell is the Ishibashi cell.

$\theta_{\rm lab}$	$\theta_{\rm cm}$	E_p (p+^{3}He ela.) [MeV]	E_p (p+^{3}He inela.) [MeV]	E_p (p+^{14}N ela.) [MeV]
35	46.9	83.0	77.2	92.7
55	71.9	69.0	63.2	89.8
65	83.7	61.1	55.3	87.8
75	94.9	53.4	47.4	85.6
85	105.5	47.2	41.2	84.1
95	115.4	40.5	34.3	81.7
105	124.8	34.4	28.1	79.5
115	133.4	29.9	23.4	77.7
125	141.6	24.1	16.7	75.2
135	149.2	20.7	12.7	73.7

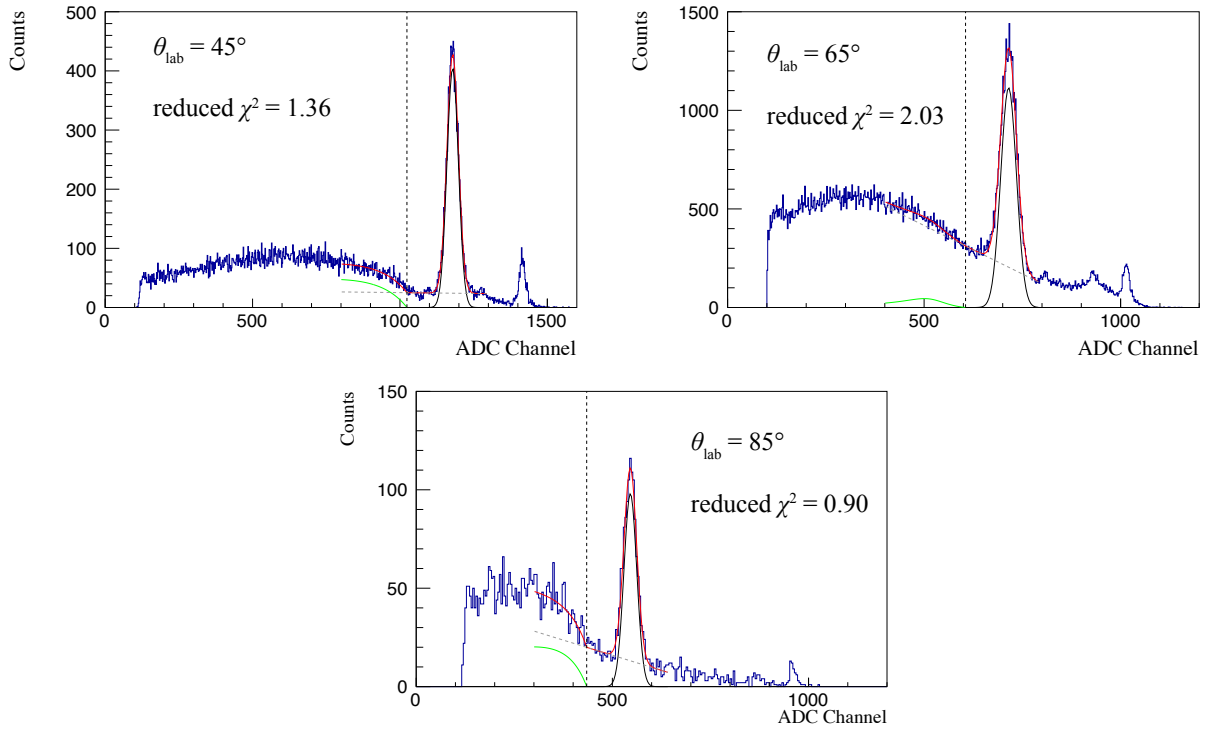

Figure 5.26: Results of the fitting to light output spectra of the E detectors for $\theta_{\rm lab} = 45°$, 65° and 85° at the experiment of CYRIC. The red lines are the fitting function, the black lines are the Gaussian fitted to the p+^{3}He elastic peaks. The inelastic functions and the linear backgrounds are shown in the green lines and the gray dashed lines, respectively. The vertical dashed lines denote the threshold of the p–^{3}He inelastic scattering. The reduced χ^2 values for the fitting are also shown.

the range of $\pm 2\sigma$ from the peak centroid of the Gaussian as the events of the p–^{3}He elastic scattering. We also evaluated the background in the $\pm 2\sigma$ range by calculating the area of trapezoid from the fitting results of linear functions. The uncertainty of the ^{3}He analyzing power due to the backgrounds was evaluated from the varying range of the events and the fittings. This uncertainty was within the statistical error of the ^{3}He analyzing power.

The structure of the inelastic events probably has the energy spread since the angular acceptance of the counters has a finite value. We evaluated the contamination of the inelastic events to the elastic ones by using the folding for Eq. (5.2) with the Gaussian function. We assumed that the standard deviation of the Gaussian was the same as that of p+^{3}He elastic peaks. As a result, we confirmed that there was no contaminants of the inelastic events to the range of elastic ones. In addition, the uncertainty of the ^{3}He

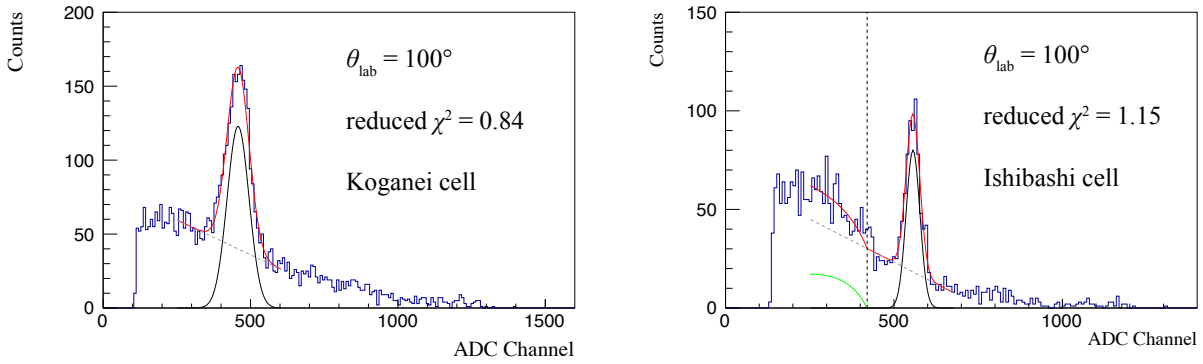

Figure 5.27: Results of the fitting to light output spectra of the E detectors for $\theta_{\rm lab} = 100°$ at the experiment of CYRIC. The left (right) panel shows the light output when the ^{3}He target was the Koganei (Ishibashi) cell. For the description of the lines see Fig. 5.26.

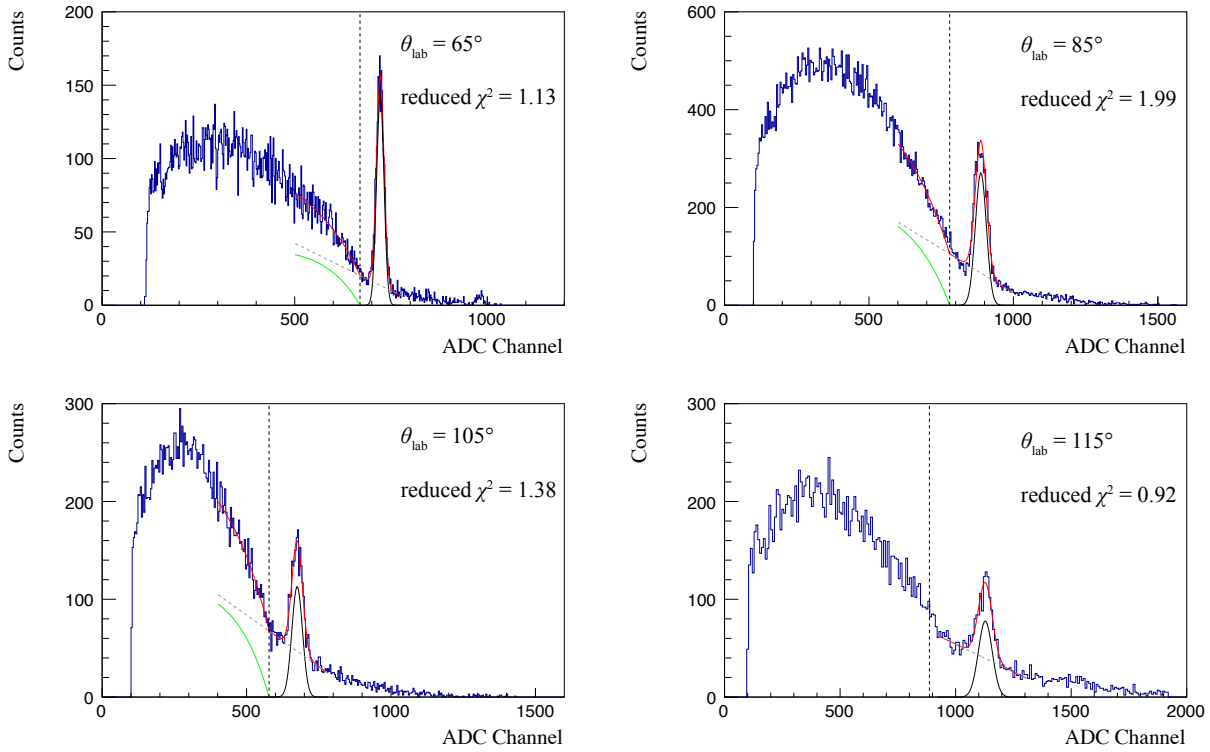

Figure 5.28: Results of the fitting to light output spectra of the E detectors for $\theta_{\rm lab} = 65°$, 85°, 105° and 115° at the experiment of RCNP. For the description of the lines see Fig. 5.26.

analyzing power from the contamination was negligible small.

5.4.3 Extraction of ^{3}He Analyzing Powers

The ^{3}He analyzing power is expressed by,

$$A_{0y} = \frac{1}{p_y}\frac{n_{\rm L}^{\uparrow} - n_{\rm L}^{\downarrow}}{n_{\rm L}^{\uparrow} + n_{\rm L}^{\downarrow}} = \frac{1}{p_y}\frac{n_{\rm R}^{\downarrow} - n_{\rm R}^{\uparrow}}{n_{\rm R}^{\uparrow} + n_{\rm R}^{\downarrow}}, \tag{5.3}$$

where n is the normalized yield of p–^{3}He elastic events. Here, we define subscripts L and R as left and right sides scattering, and superscripts $\uparrow$ and $\downarrow$ as the spin axis of the target polarization alined up ($+y$) and down ($-y$) directions. The yield normalized by the beam intensity is given by,

$$n = \frac{Y}{It\epsilon}, \tag{5.4}$$

where Y is the yield of p–^{3}He elastic events, I is the number of incident beams per unit time, t is the measurement time and ϵ is the efficiency of detectors. To extract ^{3}He analyzing powers, we used the collected beam charge by the FC as the number of incident beams and the DAQ efficiency as the overall efficiency for the detection of scattered protons. In addition, the ^{3}He analyzing power can be written as the combination from with the yields of left and right counters for spin up and down states ("cross asymmetry"):

$$A_{0y} = \frac{1}{p_y}\frac{R-1}{R+1}, \tag{5.5}$$

$$R \equiv \sqrt{\frac{Y_{\rm L}^{\uparrow}}{Y_{\rm L}^{\downarrow}}\frac{Y_{\rm R}^{\downarrow}}{Y_{\rm R}^{\uparrow}}}. \tag{5.6}$$

In this method, A_{0y} can be obtained without depending on the charge collections and the solid angles of the left and right counters.

We extracted ^{3}He analyzing powers A_{0y} by the cross asymmetry method according to the following process:

1. Extracting A_{0y} by adjoining data runs with the ^{3}He spin up and down directions for each detector.

2. Obtaining the weighted average of all over the data runs for each detector.

For extraction of ^{3}He analyzing powers, we used the average values of the target polarization measured before and after the data run.

Table 5.10: Experimental results of ^{3}He analyzing powers for the experiment of CYRIC from the method of cross asymmetry. An asterisk denotes the Koganei cell for the target.

$\theta_{\rm lab}$ [deg]	$\theta_{\rm c.m.}$ [deg]	A_{0y}	$\Delta A_{0y}^{\rm stat}$	$\Delta A_{0y}^{\rm sys}$	$\Delta A_{0y}^{\rm pol}$	$\Delta A_{0y}^{\rm asym}$
35	46.58	0.048*	0.011*	0.002*	0.002*	0.0004*
45	59.29	−0.093*	0.011*	0.004*	0.004*	0.0001*
55	71.58	−0.272*	0.008*	0.011*	0.011*	0.001*
65	83.35	−0.295*	0.008*	0.012*	0.012*	0.001*
70	89.03	−0.266*	0.003*	0.010*	0.010*	0.001*
		−0.251	0.006	0.006	0.006	0.0002
75	94.56	−0.258*	0.010*	0.011*	0.010*	0.003*
80	99.93	−0.196*	0.014*	0.008*	0.008*	0.002*
85	105.15	−0.146*	0.009*	0.005*	0.005*	0.001*
		−0.138	0.009	0.004	0.003	0.002
95	115.1	−0.013*	0.009*	0.0005*	0.0005*	0.0001*
100	119.85	0.055*	0.017*	0.002*	0.002*	0.0005*
		0.054	0.015	0.002	0.001	0.001
110	128.87	0.304*	0.015*	0.013*	0.011*	0.007*
115	133.16	0.385	0.017	0.018	0.009	0.016
125	141.34	0.432	0.027	0.022	0.010	0.020

5.5 Experimental Results

The experimental results of ^{3}He analyzing power for the experiment at CYRIC and RCNP are shown in Tables 5.10 and 5.11, respectively. The statistic errors and systematic errors of the ^{3}He analyzing powers are also shown in the tables.

We estimated the systematic error of the ^{3}He analyzing powers from two uncertainties: i) the target polarization $\Delta A_{0y}^{\rm pol}$ and ii) the false asymmetry $\Delta A_{0y}^{\rm asym}$. From the measurement of neutron transmission at RANS described in Chapter 4, we obtained the target polarization of the Koganei cell and the Ishibashi cell with accuracies of 3.7 % and 1.8 % for the experiment at CYRIC, respectively. We also obtained the target polarization with an accuracy of 6.0 % for the experiment at RCNP as described in Chapter 3. The systematic error due to the false asymmetry was estimated by the measurement with the unpolarized ^{3}He target. We evaluated the standard deviations of scattering asymmetries

Table 5.11: Experimental results of ^{3}He analyzing powers for the experiment of RCNP from the method of cross asymmetry. The target cell is the Ishibashi cell.

$\theta_{\rm lab}$ [deg]	$\theta_{\rm c.m.}$ [deg]	A_{0y}	$\Delta A_{0y}^{\rm stat}$	$\Delta A_{0y}^{\rm sys}$	$\Delta A_{0y}^{\rm pol}$	$\Delta A_{0y}^{\rm asym}$
35	46.86	0.075	0.007	0.004	0.004	0.0003
55	71.94	−0.261	0.015	0.016	0.016	0.002
65	83.73	−0.221	0.024	0.014	0.013	0.002
75	94.94	−0.227	0.036	0.014	0.014	0.004
85	105.52	−0.225	0.018	0.014	0.014	0.002
95	115.45	−0.230	0.026	0.014	0.014	0.004
105	124.75	−0.063	0.041	0.004	0.004	0.001
115	133.44	0.157	0.059	0.010	0.010	0.003
125	141.58	0.377	0.078	0.025	0.023	0.009
135	149.24	0.221	0.054	0.014	0.013	0.004

$A_{\rm asym}$,

$$A_{\rm asym} = \frac{R-1}{R+1}, \tag{5.7}$$

$$R = \sqrt{\frac{Y_{\rm L}^{\uparrow}}{Y_{\rm L}^{\downarrow}}\frac{Y_{\rm R}^{\downarrow}}{Y_{\rm R}^{\uparrow}}}, \tag{5.8}$$

during the unpolarized runs as the systematic errors from the false asymmetry. These estimated uncertainties for the systematic errors are also shown in Tables 5.10 and 5.11. Finally, we estimated the systematic errors of the ^{3}He analyzing powers as the propagation of these two systematic errors. Statistical uncertainties are less than 0.02, and the systematic uncertainties are estimated to be 0.02 or less for the data at 70 MeV. The data taken independently with the different targets are consistent within the estimated uncertainties. For the data at 100 MeV, statistical uncertainties are less than 0.04 at the forward angles ($\theta_{\rm lab} \leq 95^\circ$), and are from 0.05 to 0.08 at the backward angles ($\theta_{\rm lab} \geq 115^\circ$). The systematic uncertainties are estimated to be 0.02 or less except for the angle of $\theta_{\rm lab} = 125^\circ$. Figure 5.29 shows the experimental results of ^{3}He analyzing power versus the scattering angle in the center-of-mass system with incident energies at 70 and 100 MeV.

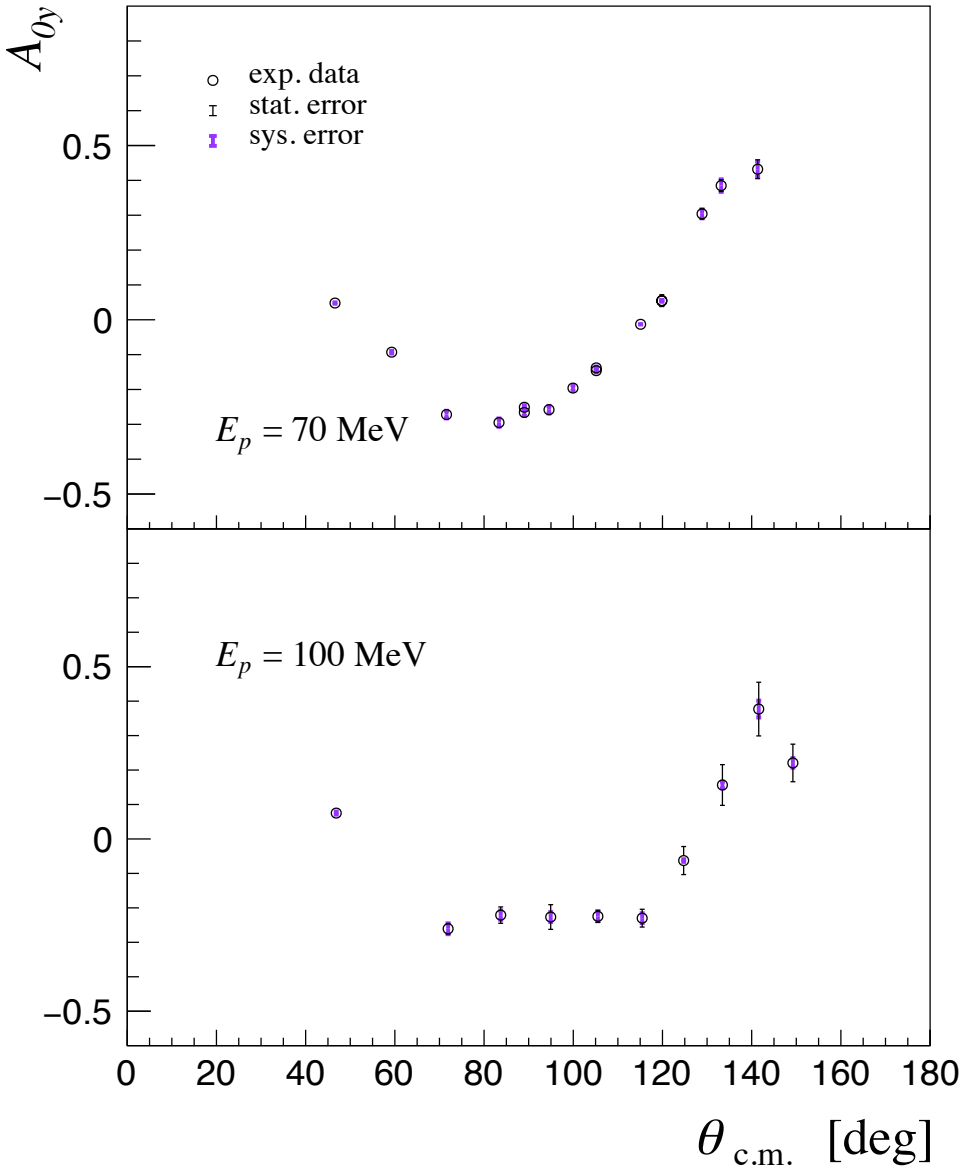

Figure 5.29: Experimental results of ^{3}He analyzing power for p–^{3}He elastic scattering at 70 MeV (top panel) and 100 MeV (bottom panel).

Chapter 6

Discussion

In this chapter, we compare the experimental data of ^{3}He analyzing powers with the theoretical predictions performed by Deltuva [120]. The brief descriptions of the theoretical calculations are given in Sec. 6.1. In Sec. 6.2, the comparison of the experimental data with the theoretical predictions is presented.

6.1 Theoretical Calculations

Theoretical calculations of the four-nucleon ($4N$) scattering above the $4N$ breakup threshold are technically very difficult owing to complicated singularities or boundary conditions. Deltuva and Fonseca have succeeded in performing the calculation for the p–^{3}He scattering above the threshold by using the AGS equations and solving them by the complex-energy method [52]. They reported the calculations of the differential cross section, the proton and ^{3}He analyzing powers, the spin-correlation coefficients and the spin-transfer coefficients at proton energies of up to 35 MeV.

In this thesis, we show the theoretical predictions based on the several 2NF potentials at 70 MeV; the AV18 [5, 22], INOY04 [53, 54], CD-Bonn [23] and semilocal momentum-space regularized (SMS) chiral NN potential [34]. We also compare the data with the calculation based on the CD-Bonn+Δ potential [28] which provides the effective three- and four-nucleon forces. The SMS potential is the currently most precise chiral EFT NN potential which introduces a semilocal regularization in momentum space for the pion-exchange contributions. This potential is considered up to fifth-order in the chiral expansion (N^{4}LO$^+$) and describes the NN data with a precision which is comparable to modern phenomenological potentials. The INOY04 potential is also compared to the

experimental data of ^{3}He analyzing powers at 100 MeV.

6.2 Comparison of Data with Theoretical Calculations

First let us show the comparison between the data of ^{3}He analyzing power A_{0y} at 8.5, 19.4, and 30.0 MeV taken from Refs. [62, 64, 65] with the theoretical calculations [52] to see how the A_{0y} data at low energies are explained by the calculations in Fig. 6.1. The theoretical predictions are based on the AV18, CD-Bonn and INOY04 NN potentials. In the calculations, all the states with total angular momentum $j \leq 6$ are taken into account so that the results are well converged. The calculations agree well with the data over the whole energy range. The calculations show small sensitivity to the NN interactions used for the A_{0y} maximum region at 8.5 MeV and the A_{0y} minimum region at 19.4 and 30.0 MeV. Generally the calculations based on the INOY04 have better agreement to the data. The INOY04 potential predict the binding energy of ^{3}He of 7.73 MeV, while the AV18 and CD Bonn potentials provide 6.92 MeV, and 7.26 MeV, respectively. Note, the experimental value of ^{3}He binding energy is 7.72 MeV. In Ref. [52] the authors have concluded that the observed sensitivity of the NN interaction models seems to be mostly due to the different predicted values of the ^{3}He binding energy and the effects of 3NFs are very probably not observed for the ^{3}He analyzing power at these energies.

We compare the newly obtained data of ^{3}He analyzing power at 70 and 100 MeV with state of the art calculations of $4N$ scattering by A. Deltuva [120] in Fig. 6.2. The experimental data are shown with the statistical errors as well as the systematic errors estimated in Chapter 5. All the states with total angular momentum $j \leq 3$ are taken into account in the calculations, for which convergence has been checked. We show the theoretical predictions based on the AV18, INOY04, SMS51, SMS53, CD-Bonn ($+\Delta$) potentials at proton energy of 70 MeV. The theoretical prediction using the INOY04 potential is only shown at 100 MeV. The SMS51 (SMS53) potentials denote that a momentum-space cutoff Λ is chosen to be 400 (500) MeV/c. As for the proton energy of 70 MeV, the predictions based on the various nuclear potentials are very close to each other except for the angular region of the A_{0y} maximum around $\theta_{\rm c.m.} = 140°$. They clearly underestimate the data in the minimum region around $\theta_{\rm c.m.} = 80°$–$100°$ and overestimate the data in the maximum region around $\theta_{\rm c.m.} = 130°$–$140°$. At low energies the INOY04 provides better descriptions of the data. However, at 70 and 100 MeV, the calculations based on this potential do not explain the data at the A_{0y} minimum as well as its maximum, and the differences found in com-

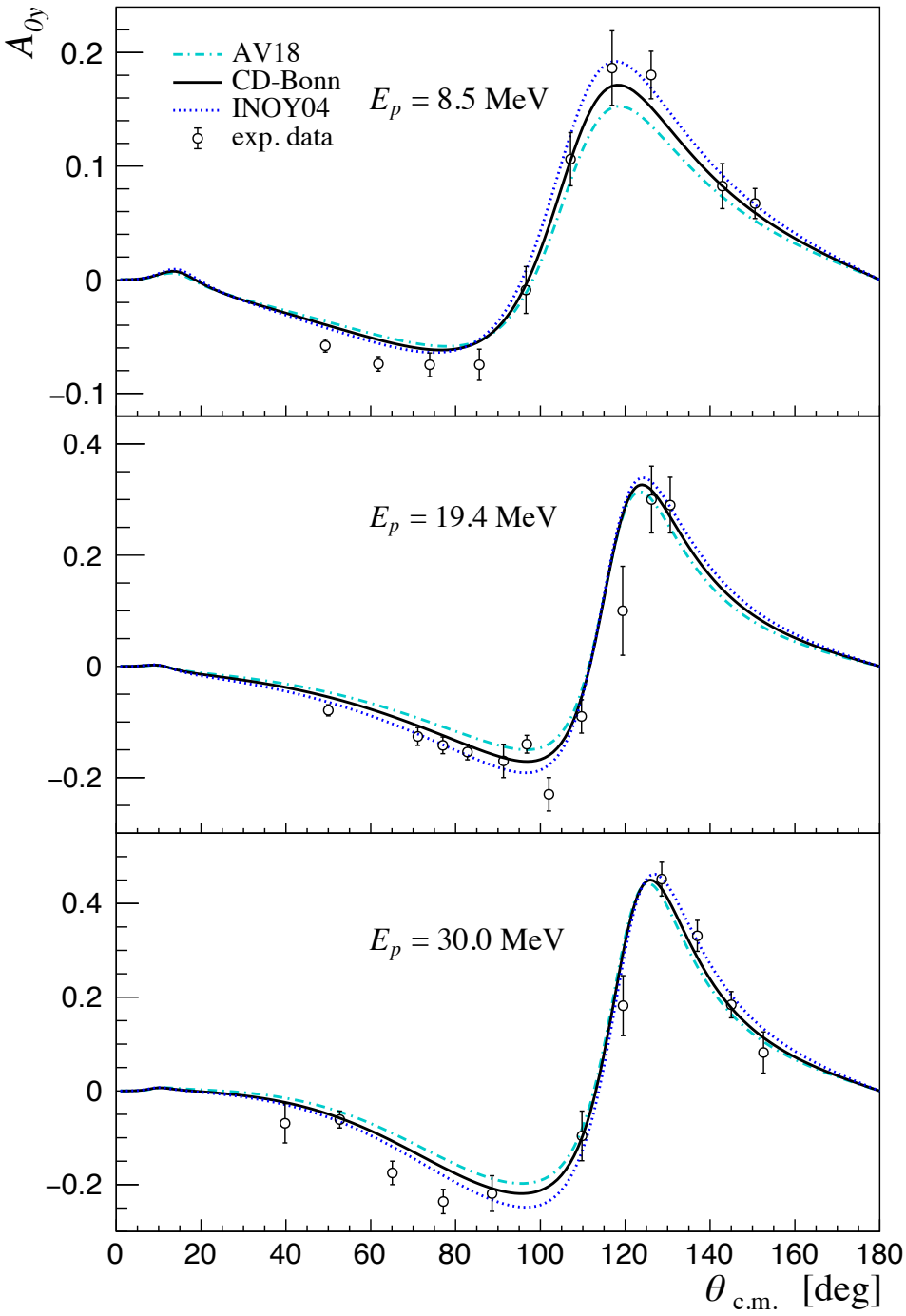

Figure 6.1: ^{3}He analyzing power A_{0y} in p–^{3}He elastic scattering at 8.5, 19.4 and 30.0 MeV. The theoretical calculations based on the AV18 (dashed-dotted curves), CD-Bonn (solid curves) and INOY04 (dotted curves) NN potentials are shown. The experimental data are from Refs. [62, 64, 65].

Table 6.1: Predicted D-state probability P_D by the modern NN potentials.

Potential	P_D [%]	Ref.
AV18	5.76	[5]
INOY04	3.60	[53]
SMS51	4.12	[34]
SMS53	5.01	[34]
CD-Bonn	4.85	[6]

parison are larger at 100 MeV. The CD-Bonn potential including Δ-isobar effects slightly changes compared to the CD-Bonn potential for c.m. angles larger than 90°. The inclusion of Δ-isobar does not explain the discrepancy between the data and the calculations. In addition, focusing on the backward angles $\theta_{\rm c.m.} = 130°$–$140°$ at 70 MeV the sensitivity of the NN interactions used is seen. Here the AV18 potential is closer to the data compared to the CD-Bonn, and INOY04. As for the chiral EFT NN potentials the SMS51 is closer to the data compared to the SMS53. This dependence seems to be related with the deuteron D-state probability P_D (see Table 6.1). Differences of the deuteron D-state probability between the NN potentials as well as the predictions of the ^{3}He binding energy are closely related with the treatments of the tensor interactions of the nuclear forces. The results of the calculations indicate that NN tensor interactions could be one of the elements to understand the discrepancies seen between the data and the theoretical calculations.

Even more considerable differences, which override the sensitivity of the NN interactions, exist between the data and the calculations based on the various NN potentials at 70 and 100 MeV. In order to see how the difference between the data and the calculations emerges with increasing an incident energy, Fig. 6.3 shows the differences between the data and the theoretical calculations at three angular regions: i) around the forward angles of $\theta_{\rm c.m.} \sim 45°$, ii) around the A_{0y} minimum ($\theta_{\rm c.m.} \sim 90°$) and iii) around the A_{0y} maximum ($\theta_{\rm c.m.} \sim 120°$–$140°$). The calculations based on the INOY04 potential are used. The differences at the forward angles are rather small; namely, the data have good agreements with the predictions. On the other hand, the obtained data of A_{0y} shows significant discrepancies at the angles where the A_{0y} takes minimum and maximum. These discrepancies become larger with increasing incident energies. Drastic discrepancies, magnitudes of 0.37 for 70 MeV and 0.26 for 100 MeV of the theoretical predictions, are observed at the backward angles $\theta_{\rm c.m.} \sim 120°$–$140°$.

The discrepancies found in the A_{0y} start to appear at higher energies (at least 70 MeV),

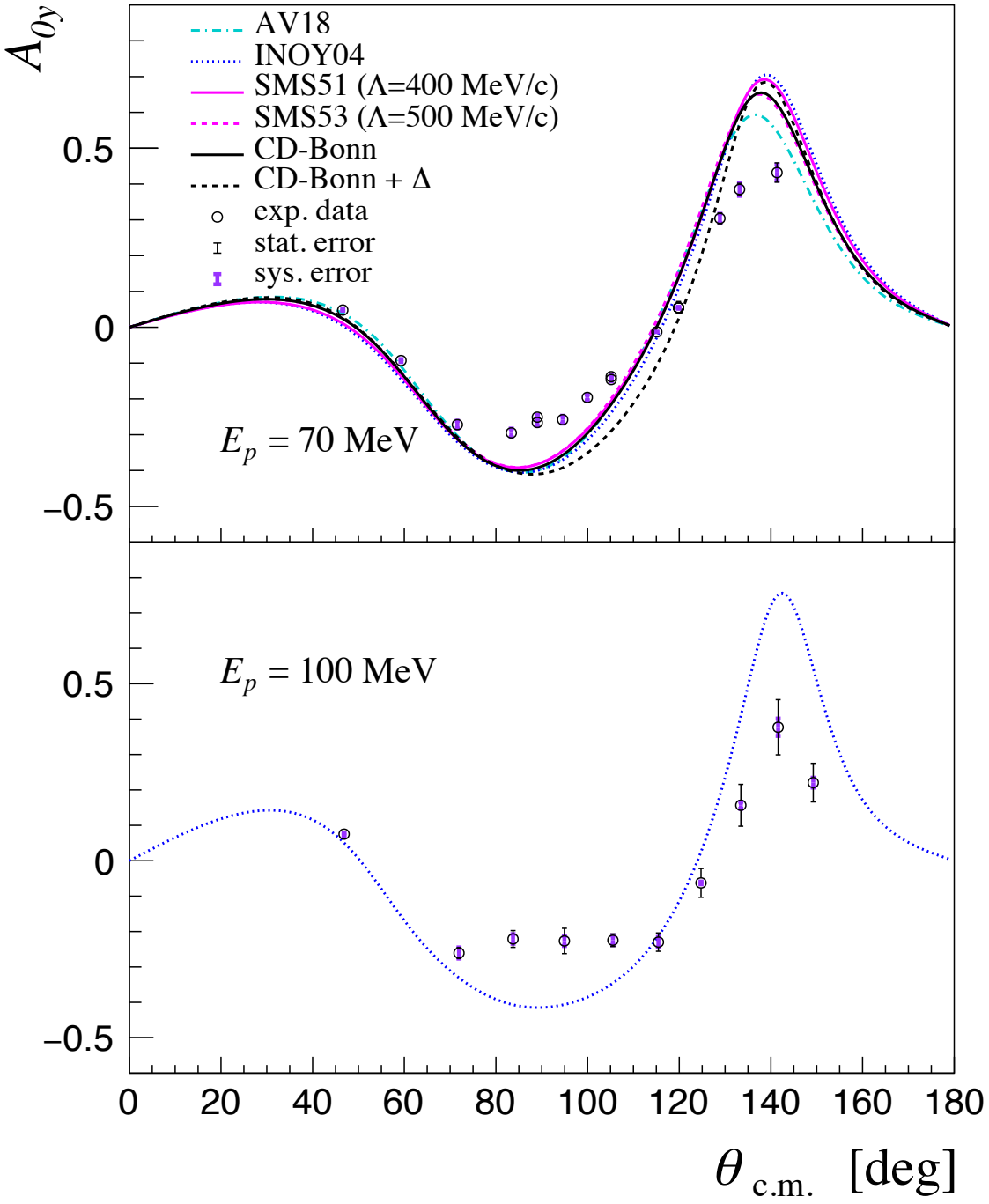

Figure 6.2: Measured ^{3}He analyzing power A_{0y} in p–^{3}He elastic scattering at 70 and 100 MeV. The theoretical calculations based on the AV18 (a cyan dashed-dotted curve), CD-Bonn (a black solid curve) and INOY04 (blue dotted curves) NN potentials are shown. The magenta solid (dashed) curve is the calculation using the SMS51 (SMS53) potential. SMS51 (SMS53) denotes that a momentum-space cutoff Λ is chosen to be 400 (500) MeV/c. The black dashed curve is the calculations based on the CD-Bonn potentials with the Δ degrees of freedom.

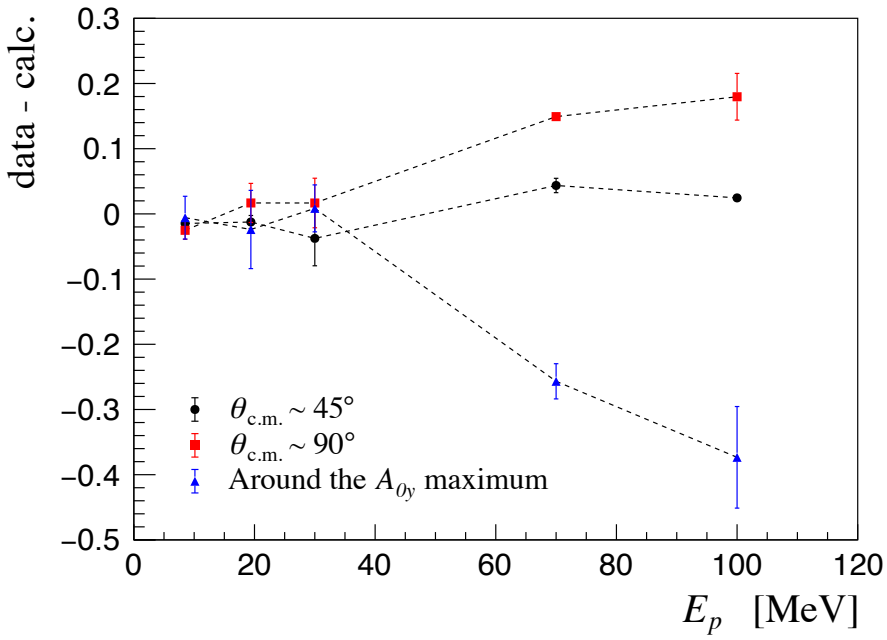

Figure 6.3: Difference between the data and the theoretical predictions of A_{0y} based on the INOY04 potential at the angle of $\theta_{\text{c.m.}} \sim 45°$, $\theta_{\text{c.m.}} \sim 90°$ and around the A_{0y} maximum.

while those have already been seen in the cross section at 30 MeV. Thus it is expected that some specific components of 3NFs could be responsible for description of the A_{0y}. For further discussions the theoretical calculations with 3NFs are needed. In the approach based on the chiral EFT the treatments of 3NFs up to the fifth-order (N^4LO) are now in progress [39]. The necessities of such higher-order 3NFs are strongly suggested in Nd elastic scattering [47] and our newly obtained ^{3}He analyzing power A_{0y}. Since there exit the 3π-ring diagrams as well as shorter range diagrams of 3NFs which are sensitive to $T = 3/2$ isospin channels, discussions of 3NFs including isospin dependence could be possible. Definitely the obtained data of A_{0y} in this study provide very important sources for quantitative understanding of the 3NFs discussed in the future.

Chapter 7

Summary and Conclusion

One of the main topic of nuclear physics is to understand nuclear properties based on bare nuclear forces. Establishing the high-precision realistic NN potentials and performing rigorous numerical calculations and *ab initio* calculations by using these potentials, the importance of three-nucleon forces (3NFs) was suggested for various nuclear phenomena such as binding energies of light mass nuclei, nuclear matter properties and few-nucleon scattering. In order to clarify the properties of 3NFs, the deuteron-nucleon scattering experiments have been conducted energetically at intermediate energies ($E \gtrsim 60$ MeV/nucleon). Comparing the high-precision data with the rigorous numerical calculations in terms of the Faddeev equation based on the realistic nuclear potentials, the effects of 3NFs have been confirmed in the cross section minimum of dp elastic scattering.

In recent years, the importance of the isospin dependence of 3NFs has been suggested for understanding of asymmetric nuclear matter, e.g. neutron-rich nuclei and neutron matter properties. We have extended the experimental prove to four-nucleon scattering, proton-^{3}He scattering, to explore the 3NF effects in four or more nucleon system. The p–^{3}He scattering is one of the attractive prove which can approach to the total isospin channel of $T = 3/2$ of 3NFs. We plan to measure the complete set of the p–^{3}He elastic scattering including differential cross sections, analyzing powers and spin-correlation coefficients at intermediate energies.

For the project of the complete measurement of p–^{3}He elastic scattering, we have developed the polarized ^{3}He target system. The polarized ^{3}He target is based on the SEOP method which utilizes spin-exchange interactions between alkali-metal atoms and ^{3}He nuclei. The ^{3}He target is the double-chambered cell made of GE180 glass and contains ^{3}He gas with pressure of 3 atm together with alkali-metals as well as N_2 gas. In this work,

we constructed two-target cells; the Koganei cell based on the SEOP method and the Ishibashi cell based on the AH-SEOP method. We measured the ^{3}He polarization by the AFP-NMR method in combination with the alkali-metal EPR method. However, the EPR measurement gives us only the ^{3}He polarization of the polarization-production part (pumping chamber). In addition, the ^{3}He number densities are quite uncertain because the gas temperature inside the cell is not obvious due to the high-power laser for optical pumping. In order to obtain the absolute value of ^{3}He polarization of the target chamber from the EPR method, it is necessary to know the ^{3}He number densities, namely the gas temperature inside each chamber. Therefore, we studied the gas temperature and the polarization gradient which is the polarization difference between the target and pumping chambers based on numerical simulations. As a result, we obtained the target polarization of the Koganei cell with an accuracy of 3.8 % and the Ishibashi cell with accuracies of 2.4 % and 6.0 % for the experimental conditions at CYRIC and RCNP. The maximum ^{3}He polarization was 30 % for the Koganei cell and 40 % for the Ishibashi cell, respectively. However, for a more detailed discussion on the gas temperature, we have to consider the X-factor. Babcock *et al*. reported that there is an excess ^{3}He relaxation term characterized by the alkali-metal density [121]. They represented the ^{3}He spin relaxation rate as $\Gamma_{^3\mathrm{He}} = X\gamma_{\mathrm{SE}} + \Gamma_{\mathrm{r}}$, where X is the phenomenological factor, so-called the X factor, and Γ_{r} is the ^{3}He spin relaxation rate at room temperatures. Although the mechanism of this additional relaxation is not well understood, it is important for estimating the gas temperature inside the cell.

We performed the neutron transmission measurement which offers direct measurement of the ^{3}He polarization in the target chamber at RANS, RIKEN. This measurement utilizes the fact that the neutron transmission for ^{3}He is dependent on the ^{3}He polarization. We measured the ^{3}He polarization of the target chamber directly with an accuracy of 3.7 % for the Koganei cell and 1.8 % for the Ishibashi cell. The obtained target polarizations have good agreements with the results from the numerical simulations described above.

Using the polarized ^{3}He target we performed the measurement of ^{3}He analyzing powers A_{0y} for p–^{3}He scattering with incident energies of 70 MeV at CYRIC and 100 MeV at RCNP. We obtained the data in the wide angular range $\theta_{\mathrm{c.m.}} = 46°$–$141°$ and $\theta_{\mathrm{c.m.}} = 47°$–$149°$ for the experiments at CYRIC and RCNP, respectively. For the data at 70 MeV, the statistical uncertainties are less than 0.02, and the systematic uncertainties are estimated to be 0.02 or less. The data taken independently with the different targets are consistent within the estimated uncertainties. For the data at 100 MeV, the statistical uncertainties are less than 0.04 at the forward angles ($\theta_{\mathrm{c.m.}} \leq 116°$), and are from 0.05 to 0.08 at the

backward angles ($\theta_{\rm c.m.} \geq 133^\circ$). The systematic uncertainties are estimated to be 0.02 or less except for the angle of $\theta_{\rm c.m.} = 142^\circ$.

Our experimental data of A_{0y} were compared with the theoretical predictions based on various nuclear potentials. In comparison of the data with the predictions, clear discrepancies which override the sensitivity of the NN interactions were found at around the angles where the A_{0y} takes minimum and maximum. These discrepancies become larger with increasing an incident energy. The discrepancies were not observed at energies below 30.0 MeV. We also compared the data with the prediction taking into account the Δ-isobar combined with the CD-Bonn potential which provides effective three- and four-nucleon forces. However the inclusion of Δ-isobar did not explain the discrepancy observed at 70 MeV. Energy dependent study from 8.5 to 100 MeV in A_{0y} in comparison between the data and the theoretical predictions indicates that effects of fine components of 3NFs would be appearing with increasing an incident energy. For further discussion the calculations with 3NFs, e.g. 3NFs based on chiral EFT, are needed.

The measurements of differential cross sections and other spin observables will be required in addition to our A_{0y} data for the complete measurement of elastic p–^{3}He scattering at intermediate energies. For further step, we plan to perform the measurements of the differential cross section and the other spin observables than the A_{0y}, i.e., the proton analyzing power and the all spin-correlation coefficients, in the wide angular range at intermediate energies (65-200 MeV), that allows us to extract the scattering amplitudes at different incident energies. In parallel to this thesis, the experiments of the cross section as well as the proton analyzing power and the spin-correlation coefficient $C_{y,y}$ have been performed at 65 MeV, and the data analysis is in progress [122]. In order to measure the other spin-correlation coefficients such as $C_{x,x}$, $C_{z,z}$, $C_{x,z}$ and $C_{z,x}$, it is necessary to tilt the polarization axis of ^{3}He. Therefore, further improvements of the polarized target system are needed. Based on the improvements of the target system, we will achieve the complete measurement of the elastic p–^{3}He scattering at intermediate energies. In the near future, discussions of 3NFs based on the chiral EFT nuclear potentials will start in comparison with high precision data of the Nd scattering as well as the p–^{3}He scattering. Since the total isospin channel is limited to $T = 1/2$ for the Nd scattering, the p–^{3}He scattering data could be useful sources to nail down the properties of $T = 3/2$ channels.

Finally, we note that the obtained data are the first precise data of ^{3}He analyzing power for p–^{3}He elastic scattering at intermediate energies covering the wide angular range. Our data of A_{0y} provide very important sources for quantitative discussions for the 3NF effects

in the future.

Bibliography

[1] H. Yukawa, Proc. Phys. Math. Soc. Japan **17**, 48–57 (1935).

[2] C. M. G. Lattes *et al.*, Nature **159**, 694–697 (1947).

[3] M. H. MacGregor, R. A. Arndt and R. M. Wright, Phys. Rev. **182**, 1714–1728 (1969).

[4] V. G. J. Stoks *et al.*, Phys. Rev. C **48**, 792–815 (1993).

[5] R. B. Wiringa, V. G. J. Stoks and R. Schiavilla, Phys. Rev. C **51**, 38–51 (1995).

[6] R. Machleidt, Phys. Rev. C **63**, 024001 (2001).

[7] V. G. J. Stoks *et al.*, Phys. Rev. C **49**, 2950–2962 (1994).

[8] S. C. Pieper *et al.*, Phys. Rev. C **64**, 014001 (2001).

[9] P. Navrátil and W. E. Ormand, Phys. Rev. C **68**, 034305 (2003).

[10] A. Akmal, V. R. Pandharipande and D. G. Ravenhall, Phys. Rev. C **58**, 1804–1828 (1998).

[11] E. Wigner, Phys. Rev. **43**, 252–257 (1933).

[12] J. Fujita and H. Miyazawa, Prog. Theor. Phys. **17**, 360–365 (1957).

[13] S. Coon *et al.*, Nucl. Phys. A **317**, 242–278 (1979).

[14] S. A. Coon and W. Glöckle, Phys. Rev. C **23**, 1790–1802 (1981).

[15] S. A. Coon and J. L. Friar, Phys. Rev. C **34**, 1060–1071 (1986).

[16] B. S. Pudliner *et al.*, Phys. Rev. C **56**, 1720–1750 (1997).

[17] C. R. Chen *et al.*, Phys. Rev. C **33**, 1740–1752 (1986).

[18] T. Sasakawa and S. Ishikawa, Few–Body Syst. **1**, 3–12 (1986).

[19] L. D. Faddeev, Sov. Phys. JETP **12**, 1014–1019 (1961).

[20] A. Nogga *et al.*, Phys. Rev. C **65**, 054003 (2002).

[21] O. A. Yakubovsky, Sov. J. Nucl. Phys. **5**, 937 (1967).

[22] R. B. Wiringa, R. A. Smith and T. L. Ainsworth, Phys. Rev. C **29**, 1207–1221 (1984).

[23] R. Machleidt, K. Holinde and Ch. Elster, Phys. Rep. **149**, 1–89 (1987).

[24] J. L. Friar, D. Hüber and U. van Kolck, Phys. Rev. C **59**, 53–58 (1999).

[25] S. Coon and H. Han, Few–Body Syst. **30**, 131–141 (2001).

[26] H. Kamada, D. Hüber and A. Nogga, Few–Body Syst. **30**, 121–129 (2001).

[27] A. Nogga *et al.*, Phys. Lett. B **409**, 19–25 (1997).

[28] A. Deltuva, R. Machleidt and P. U. Sauer, Phys. Rev. C **68**, 024005 (2003).

[29] A. Deltuva, A.C. Fonseca and P.U. Sauer, Phys. Lett. B **660**, 471–477 (2008).

[30] S. Weinberg, Phys. Lett. B **251**, 288–292 (1990).

[31] E. Epelbaum, W. Glöckle and Ulf-G. Meißner, Nucl. Phys. A **637**, 107–134 (1998).

[32] E. Epelbaum, Prog. Part. Nucl. Phys. **57**, 654–741 (2006).

[33] E. Epelbaum, H.-W. Hammer and Ulf-G. Meißner, Rev. Mod. Phys. **81**, 1773–1825 (2009).

[34] P. Reinert, H. Krebs and E. Epelbaum, Eur. Phys. J. A **54**, 86 (2018).

[35] R. Navarro Pérez, J. E. Amaro and E. Ruiz Arriola, Phys. Rev. C **88**, 064002 (2013) **91**, 029901 (E) (2015).

[36] L. Girlanda, A. Kievsky and M. Viviani, Phys. Rev. C **84**, 014001 (2011).

[37] H. Krebs, A. Gasparyan and E. Epelbaum, Phys. Rev. C **85**, 054006 (2012).

[38] H. Krebs, A. Gasparyan and E. Epelbaum, Phys. Rev. C **87**, 054007 (2013).

[39] E. Epelbaum *et al.*, arXiv:1907.03608 (2019).

[40] E. Epelbaum, H. Krebs and P. Reinert, arXiv:1911.11875 (2019).

[41] W. Glöckle *et al.*, Phys. Rep. **274**, 107–285 (1996).

[42] H. Witała *et al.*, Phys. Rev. Lett. **81**, 1183–1186 (1998).

[43] N. Sakamoto *et al.*, Phys. Lett. B **367**, 60–64 (1996).

[44] H. Sakai *et al.*, Phys. Rev. Lett. **84**, 5288–5291 (2000).

[45] K. Sekiguchi *et al.*, Phys. Rev. C **65**, 034003 (2002).

[46] K. Sekiguchi *et al.*, Phys. Rev. Lett. **95**, 162301 (2005).

[47] K. Sekiguchi *et al.*, Phys. Rev. C **96**, 064001 (2017).

[48] S. C. Pieper, K. Varga and R. B. Wiringa, Phys. Rev. C **66**, 044310 (2002).

[49] S. Gandolfi *et al.*, Eur. Phys. J. A **50**, 10 (2014).

[50] R. Schiavilla *et al.*, Phys. Rev. Lett. **98**, 132501 (2007).

[51] M. Viviani *et al.*, Phys. Rev. Lett. **111**, 172302 (2013).

[52] A. Deltuva and A. C. Fonseca, Phys. Rev. C **87**, 054002 (2013).

[53] P. Doleschall, Phys. Rev. C **69**, 054001 (2004).

[54] R. Lazauskas and J. Carbonell, Phys. Rev. C **70**, 044002 (2004).

[55] T. Clegg *et al.*, Nucl. Phys. **50**, 621–628 (1964).

[56] D. G. McDonald, W. Haeberli and L. W. Morrow, Phys. Rev. **133**, B1178–B1182 (1964).

[57] R. L. Hutson *et al.*, Phys. Rev. C **4**, 17–22 (1971).

[58] B. T. Murdoch *et al.*, Phys. Rev. C **29**, 2001–2008 (1984).

[59] S. D. Baker *et al.*, Nucl. Phys. A **160**, 428–436 (1971).

[60] N. Jarmie and J. H. Jett, Phys. Rev. C **10**, 57–59 (1974).

[61] J. Birchall *et al.*, Phys. Rev. C **29**, 2009–2012 (1984).

[62] M. T. Alley and L. D. Knutson, Phys. Rev. C **48**, 1890–1900 (1993).

[63] D. Müller, R. Beckmann and U. Holm, Nucl. Phys. A **311**, 1–10 (1978).

[64] R. H. McCamis *et al.*, Phys. Rev. C **31**, 1651–1655 (1985).

[65] T. V. Daniels *et al.*, Phys. Rev. C **82**, 034002 (2010).

[66] L. G. Votta *et al.*, Phys. Rev. C **10**, 520–528 (1974).

[67] N. P. Goldstein, A. Held and D. G. Stairs, Can. J. Phys. **48**, 2629–2639 (1970).

[68] J. S. Wesick *et al.*, Phys. Rev. C **32**, 1474–1487 (1985).

[69] Y. Shimizu *et al.*, Phys. Rev. C **76**, 044003 (2007).

[70] G. G. Ohlsen, Rep. Prog. Phys. **35**, 717–801 (1972).

[71] Y. Wada, PhD thesis, Tohoku University (2017).

[72] J. L. Friar *et al.*, Phys. Rev. C **42**, 2310–2314 (1990).

[73] K. Coulter *et al.*, Nucl. Instr. and Meth. A **270**, 90–94 (1988).

[74] K. Coulter *et al.*, Nucl. Instr. and Meth. A **288**, 463–466 (1990).

[75] G. L. Greene, A. K. Thompson and M. S. Dewey, Nucl. Instr. and Meth. A **356**, 177–180 (1995).

[76] F. D. Colegrove, L. D. Schearer and G. K. Walters, Phys. Rev. **132**, 2561–2572 (1963).

[77] M. A. Bouchiat, T. R. Carver and C. M. Varnum, Phys. Rev. Lett. **5**, 373–375 (1960).

[78] W. C. Chen *et al.*, J. Phys.: Conf. Ser. **294**, 012003 (2011).

[79] M. E. Wagshul and T. E. Chupp, Phys. Rev. A **40**, 4447–4454 (1989).

[80] B. Larson *et al.*, Phys. Rev. A **44**, 3108–3118 (1991).

[81] Z. Wu, T. G. Walker and W. Happer, Phys. Rev. Lett. **54**, 1921–1924 (1985).

[82] M. E. Wagshul and T. E. Chupp, Phys. Rev. A **49**, 3854–3869 (1994).

[83] C. B. Alcock, V. P. Itkin and M. K. Horrigan, Canadian Metallurgical Quarterly **23**, 309–313 (1984).

[84] R. M. Herman, Phys. Rev. **137**, A1062–A1065 (1965).

[85] B. Chann *et al.*, Phys. Rev. A **66**, 032703 (2002).

[86] N. R. Newbury *et al.*, Phys. Rev. A **48**, 4411–4420 (1993).

[87] G. D. Cates, S. R. Schaefer and W. Happer, Phys. Rev. A **37**, 2877–2885 (1988).

[88] R. L. Gamblin and T. R. Carver, Phys. Rev. **138**, A946–A960 (1965).

[89] E. Babcock *et al.*, Phys. Rev. Lett. **91**, 123003 (2003).

[90] W. Happer, Rev. Mod. Phys. **44**, 169–249 (1972).

[91] J. T. Singh *et al.*, Phys. Rev. C **91**, 055205 (2015).

[92] W. C. Chen *et al.*, Phys. Rev. A **75**, 013416 (2007).

[93] David R. Lide, editor, *CRC Handbook of Chemistry and Physics, Internet Version 2005*, CRC Press, Boca Raton, FL (2005).

[94] B. Lancor and T. G. Walker, Phys. Rev. A **83**, 065401 (2011).

[95] J. Schmiedeskamp *et al.*, Eur. Phys. J. D **38**, 427–438 (2006).

[96] Q. Ye *et al.*, Eur. Phys. J. A **44**, 55–61 (2010).

[97] D. C. Morton, Astrophys. J. Suppl. Ser. **77**, 119–202 (1991).

[98] D. C. Morton, Astrophys. J. Suppl. Ser. **130**, 403–436 (2000).

[99] M. V. Romalis and W. Happer, Phys. Rev. A **60**, 1385–1402 (1999).

[100] F. Bloch and A. Siegert, Phys. Rev. **57**, 522–527 (1940).

[101] G. D. Cates *et al.*, Phys. Rev. A **38**, 5092–5106 (1988).

[102] E. Arimondo, M. Inguscio and P. Violino, Rev. Mod. Phys. **49**, 31–75 (1977).

[103] G. Breit and I. I. Rabi, Phys. Rev. **38**, 2082–2083 (1931).

[104] M. V. Romalis and G. D. Cates, Phys. Rev. A **58**, 3004–3011 (1998).

[105] L. C. Balling, R. J. Hanson and F. M. Pipkin, Phys. Rev. **133**, A607–A626 (1964).

[106] E. Babcock *et al.*, Phys. Rev. A **71**, 013414 (2005).

[107] S. Shibuya, Master's thesis, Tohoku University (2018).

[108] D. K. Walter, W. M. Griffith and W. Happer, Phys. Rev. Lett. **86**, 3264–3267 (2001).

[109] E. Normand *et al.*, Journal of Physics: Conference Series **711**, 012012 (2016).

[110] T. E. Chupp *et al.*, Phys. Rev. C **45**, 915–930 (1992).

[111] P. A. M. Dolph *et al.*, Phys. Rev. C **84**, 065201 (2011).

[112] V. P. Alfimenkov *et al.*, Sov. J. Nucl. Phys. **25**, 607 (1977).

[113] C. D. Keith *et al.*, Phys. Rev. C **69**, 034005 (2004).

[114] Y. Ikeda *et al.*, Nucl. Instr. and Meth. A **833**, 61–67 (2016).

[115] Y. Otake *et al.*, Journal of Disaster Research **12**, 585–592 (2017).

[116] K. Hirota *et al.*, Phys. Chem. Chem. Phys. **7**, 1836–1838 (2005).

[117] M. Moinester *et al.*, Phys. Lett. B **230**, 41–45 (1989).

[118] A. Erell *et al.*, Phys. Rev. C **34**, 1822–1844 (1986).

[119] F. Irom *et al.*, Phys. Rev. C **34**, 2231–2239 (1986).

[120] A. Deltuva, private communication.

[121] E. Babcock *et al.*, Phys. Rev. Lett. **96**, 083003 (2006).

[122] RCNP E442 experiment and the RCNP project "Study of three–nucleon force effects in p+^{3}He at intermediate energies", (Spokesperson : Kimiko Sekiguchi).

Acknowledgements

In conducting this work and working as a graduate student at Tohoku University, I have been given guidance, encouragement and support from many people. I would like to express hearty thank here.

First of all, I am grateful to my supervisor, Prof. Kimiko Sekiguchi, for giving me a valuable opportunity to study the interesting subject. She kindly cared me when I went to Tohoku University as a graduate student and did not accustomed to the change of environment. Her eager teaching about the knowledge and attitude as a researcher has grown me greatly. I also would like to highly appreciate to Dr. Kenjiro Miki for his insightful comments and support for my research.

The development of the polarized ^{3}He target system would be impossible without the grate support from many people. Prof. Takashi Ino made great contributions for our study, such as lending us valuable devices and the *short training* at KEK, as well as much advice on the polarized ^{3}He target. Dr. Takashi Wakui and Prof. Todd Averett gave us the constructive advice about the polarized ^{3}He target. The beautiful and wonderful grass cells were made by Mr. Mitsuru Ohgi, Mr. Shuhei Sawada and Ms. Yuka Sato at a glass shop of School of Science, Tohoku University. Prof. Masaki Fujita kindly lent the wonderful laser system produced by OptiGrate Co. to us. I am deeply indebted to them.

I would like to express my gratitude to Prof. Toshio Kobayashi and Prof. Toshiyuki Sumikama for their insightful advice and experimental support.

Our experiments have been constructed with the outstanding work of the CYRIC, RCNP and RANS accelerator groups. Prof. Masatoshi Itoh and Dr. Yohei Matsuda provided various contributions for the experiments at CYRIC. We have greatly benefited from Dr. Kenichi Harada for lasers used in the polarized ^{3}He target system. I would also like to show my appreciation to everyone who has contributed to the experiment at RCNP: Prof. Kichiji Hatanaka, Prof. Mitsuhiro Fukuda, Prof. Eiji Ideguchi, Prof. Tatsushi Shima, Prof. Hiroki Kanda, Prof. Hooi Jin Ong, Dr. Tomoaki Hotta, Dr. Tomokazu Suzuki,

Dr. Dinh Trong Tran, Mr. Hidetomo Yoshida and Mr. Michio Uraki. Many collaborators made enormous contribution in conducting our experiment at RCNP: Prof. Tomotsugu Wakasa, Mr. Shuhei Goto, Mr. Shinji Mitsumoto, Mr. Hisanori Oshiro, Mr. Yuma Hirai, Mr. Daiki Inomoto and Ms. Hina Kasahara from Kyushu University; Prof. Yukie Maeda and Mr. Kotaro Nonaka from University of Miyazaki. I am also deeply indebted to the members of the RANS accelerator group: Dr. Yoshie Otake, Dr. Atsushi Taketani, Dr. Yasuo Wakabayashi, Dr. Yoshimasa Ikeda, Dr. Maki Mizuta, Dr. Takaoki Takanashi, Dr. Chihiro Iwamoto, Dr. Hideo Morimoto, Mr. Makoto Goto, Mr. Takao Hashiguchi and Mr. Shunsuke Mihara. I would like to thank to Prof. Hideyuki Sakai, Dr. Tomohiro Uesaka and Dr. Shinsuke Ota for collaborating and supporting our experiments. I would also like to show my appreciation to the technical stuff, Mr. Hiroo Umetsu, for his wonderful support to our work.

For the apparatuses of the experiments and the polarized ^{3}He target system, I would like to thank Mr. Shigeru Yanagawa from SIGMAKOKI Co. Ltd., Mr. Toshio Suda from Photonic Science Technology Inc., Mr. Kenichi Matsuda from MIMASU Co. Ltd. and Mr. Yukio Hasegawa from REFTEC Co. Ltd..

I really appreciate the feedback offered by my Ph.D. thesis committee: Prof. Hirokazu Tamura, Prof. Toshimi Suda, Prof. Tomoyuki Sanuki, Prof. Masatoshi Itoh and Prof. Kimiko Sekiguchi.

I would like to express my gratitude to Prof. Arnoldas Deltuva and Prof. Soichi Ishikawa for their theoretical support, comments and discussions about 3NFs.

Senior members of our laboratory, Dr. Yasunori Wada and Mr. Yuta Shiokawa, kindly taught me about the polarized ^{3}He target system and other physical knowledge. This Ph.D. thesis would be impossible without the great teaching and previous study by Y. Wada, and the excellent measurement program made by Y. Shiokawa. I am deeply grateful to them. I would also like to express my greatest appreciation to the wonderful work by the other labmates: Mr. Shinnosuke Nakai, Mr. Daisuke Sakai, Ms. Minami Inoue, Mr. Yuta Utsuki, Mr. Sho Kitayama and Ms. Yuko Saito. I wish S. Nakai can do the best for the future study and defend his Ph.D.. I would also like to thank the graduated labmates: Mr. Daijiro Eto, Ms. Tomomi Akieda, Mr. Hiroshi Kon, Mr. Tomoyuki Mukai, Mr. Shun Shibuya, Mr. Morihiro Watanabe, Mr. Yoshinori Inoue and Mr. Kenta Kawahara. I also received generous support from the members of the other laboratory: Ms. Natsumi Ichige, Ms. Sadami Suto, Mr. Yuta Takahashi, Ms. Manami Fujita, Mr. Kazuhisa Honda and Mr. Shunki Ishikawa. I had a lot of fun for my life as a graduate student at Tohoku

University with them.

Finally, I would like to my special thanks to my parents and sister. I received generous support and encouragement from them. Without the great and hearty support from my family, I would not be what I am now. Again, my heartfelt appreciation goes to my family.